

UNIVERSITY OF ILLINOIS AT URBANA-CHAMPAIGN

THE GRADUATE COLLEGE

SEPTEMBER 1993

WE HEREBY RECOMMEND THAT THE THESIS BY

JONG WON SHON

ENTITLED MODELING OF HIGH PRESSURE RARE GAS LASERS:

KINETICS AND PLASMA CHEMISTRY

BE ACCEPTED IN PARTIAL FULFILLMENT OF THE REQUIREMENTS FOR

THE DEGREE OF DOCTOR OF PHILOSOPHY

Mark J. Kushner
Director of Thesis Research

N. Narayana Rao
Head of Department

Committee on Final Examination†

Mark J. Kushner

Chairperson

J. H. Eden

Thomas A. McDevitt

Joseph J. Verdugan

Robert R. Finner

† Required for doctor's degree but not for master's.

MODELING OF HIGH PRESSURE RARE GAS LASERS: KINETICS AND PLASMA CHEMISTRY

Jong Won Shon, Ph.D.
Department of Electrical and Computer Engineering
University of Illinois at Urbana-Champaign, 1994
M. J. Kushner, Advisor

The recent interest in high pressure rare gases for use as active media for high power lasers is due to their high operating efficiency, excellent optical homogeneity, and long gas lifetime. A computer model has been developed to investigate the excitation and deexcitation mechanisms and to optimize the laser performance over the wide range of operating parameters. Three rare gas lasers have been computationally investigated: the Xe laser with Ar, He/Ar and Ne/Ar buffer gases, the Ne laser with He/Ar buffer gases and the Ar laser with He buffer gases.

The infrared atomic Xe laser ($5d \rightarrow 6p$) is an attractive candidate for fission-fragment excitation which provides low-power deposition ($1\text{-}100 \text{ W cm}^{-3}$), long pulse lengths ($1\text{-}10 \text{ ms}$), and high energy deposition (100s J l^{-1}). Optical gain at 1.73 and $2.03 \text{ }\mu\text{m}$ has recently been measured in a reactor-excited Xe laser yielding values exceeding $0.03\text{-}0.05 \text{ cm}^{-1}$ at power depositions of less than 10s W cm^{-3} . Gain was also found to rapidly terminate before the peak of the pump pulse under some experimental conditions. A computer model has been developed to predict gain in fission-fragment-excited Xe lasers, and these experiments have been analyzed. It is found that the termination of gain is most likely attributable to gas heating which increases the electron density, leading to electron collision quenching. The specific dependence of gain on pump rate suggests that a reduced rate of recombination of molecular ions with increasing gas temperature is partly responsible for this behavior.

The high pressure atomic Ne laser operates on four visible transitions between the $3p$ and $3s$ manifolds. Oscillation at 585 nm ($3p'[1/2]_0 \rightarrow 3s'[1/2]_1$) with efficiency of $> 1\%$ has been demonstrated by others. The upper laser level is believed to be populated by dissociative recombination of Ne_2^+ , while state-selective Penning reactions relax the lower laser levels. To

investigate these pumping mechanisms, experimental and modeling studies have been performed on a short pulse e -beam excited Ne laser, using He/Ne/Ar mixtures. We found that the electron temperature in the afterglow following the e -beam pulse largely determines the time at which oscillation starts. Electron temperature during the afterglow is partly controlled by a slow relaxation of excited states in Ar. Laser oscillation does not occur until these manifolds are depleted and the electron temperature decreases, thereby increasing the rate of dissociative recombination.

The high pressure (≥ 0.5 atm) atomic Ar laser ($3d \rightarrow 4p$) oscillates on four infrared transitions (1.27 - 2.4 μm). Quasi-continuous oscillation on the 1.79 μm transition has been obtained using electron-beam and fission-fragment excitations over a wide range of power deposition and gas pressure. In this regard, a computer model has been developed to investigate excitation mechanisms of the Ar laser. Results from the model suggest that the upper laser level of the 1.79 μm transition [$\text{Ar}(3d[1/2]_1)$] is dominantly populated by dissociative recombination of HeAr^+ . In contrast, the dissociative recombination of Ar_2^+ is believed to predominantly produce $\text{Ar}(4s)$ states. Electro-ionization from Ar metastables at moderate to high pump rates is responsible for the high efficiency of the Ar laser. Gain and laser oscillation are discussed and compared to measurements made for He/Ar gas mixtures which use various Ar mole fractions and total pressures. These results show that the optimum Ar mole fractions in He/Ar mixtures are approximately 0.1 - 5 % for quasi-continuous pumping.

DEDICATION

To my parents, Choon Shik and Gab Soon Shon, and
my wife Jong In

ACKNOWLEDGMENTS

The author would like to express appreciation to the Sandia National Laboratory for their support of this project, with special thanks to Dr. Hebner and Dr. Hays for the helpful discussions and their experimental results.

The author would like to deeply thank his advisor, Professor Mark Kushner, for his guidance, dedication, and patience. Without his fatherly advice and genuine concern, this thesis would never have been materialized. He also express thanks to the professors in his committee for the preliminary and final defense: Joe Verdeyen, Tom DeTemple, Gary Eden, and Kevin Kim. Their expertise and genuine interest in the author's project deeply moved him. The lessons that he learned from his preliminary and final defense will never be forgotten.

The author also wishes to express thanks to the various members of the ODP group, present and past: Mieko Ohwa, Hoyoung Pak, Mike McCaughy, Mike Hartig, Tim Sommerer, Yilin Wang, Jeanne Balbach, Seung Choi, Phillip Stout, Fred Huang, Helen Hwang, Peter Ventzek, Irène Pérès, Rob Hoekstra, Ann Gentile, Mike Grapperhaus and Professor Kitamori. Their friendship and kindness will remain with the author for a long time. Three of the undergraduate assistants who have worked with me, Chow Pin Chong, John Lape, and Matt Vogel, deserve special thanks for their technical assistance and friendship. He also express thanks to our secretary, Mrs. Jean Sexton for all the miscellaneous and essential tasks.

The author would like to thank the officers of the Korean Student Association and Korean Undergraduate Student Association for their dedication and assistance during the author's presidency (1992-1993). Without their assistance, the author would never find enough time to finish his thesis. Special thanks goes to Taeill Lee, Jinho Rha, Jaeho Kim, Juhi Kee, Nae Eung Lee, Kwon Jung, Jaewon Kim, Haewook Han, Dongphil Yoon, Yoojoong Kim, Seung Jin Choi, Meg Kim and Heechong Kim.

The author expresses special thanks to his friends: Eunsoo Shin, Sungbum Kim, Wonkoo Lee, Dongwan and Eunha Cho, Jongwon Park, Keehyeung Lee, Yeonhee Choi, Ikmo

Park, Sungho Kim, Wankee Jun, Hungse Cha, Hansuk Kim and Jongyeul Chang. Their companionship and kindness gave him courage and tenacity to endure his long and exhaustive graduate career.

The author would like to express thanks to the church where he served as a deacon. He expresses thanks to the pastors, elders and deacons: Doohyun Paik, Sunghwan Kim, Hayngsung Yang, Kyekyoon Kim, Kunil Lee, Hye Suk Yoon, Youngdong Kim, and Joohyun Choi.

The author would like to thank his parents: Choon Shik and Gab Soon Shon. Their prayers and support helped their son to finally succeed in his quest for the degree. He also thanks his two loving sisters, Nayoung and Minhi, for their love of their brother. He especially thanks his father and mother in-law, Tai Hee Park and Soon Hee Yoon, for their love and support.

The author expresses thanks to his wife, Jong In, for her support and love throughout the author's academic career. Without her encouragement, patience and sacrifice, this thesis would not be possible.

TABLE OF CONTENTS

| | | PAGE |
|----|--|------|
| 1. | INTRODUCTION | 1 |
| | 1.1 References..... | 4 |
| 2. | BRIEF DESCRIPTION OF THE MODEL FOR RARE GAS ATOMIC LASERS | 5 |
| | 2.1 Pumping Mechanisms..... | 5 |
| | 2.2 Plasma-Chemical Kinetics..... | 6 |
| | 2.3 Rate Equations | 9 |
| | 2.4 Electron Temperature and Gas Temperature Modeling..... | 9 |
| | 2.5 References | 10 |
| 3. | PREDICTIONS FOR GAIN IN THE FISSION-FRAGMENT-EXCITED ATOMIC XENON LASER | 11 |
| | 3.1 Introduction..... | 11 |
| | 3.2 Description of Model and Experiment..... | 14 |
| | 3.3 Derived Rate Coefficients and Processes | 17 |
| | 3.3.1 Broadening rate coefficients | 17 |
| | 3.3.2 Energy loading and gas temperature effects | 18 |
| | 3.3.3 Effects of branching of heavy particle quenching of Xe(6p)..... | 19 |
| | 3.4 Analysis of Gain for Ar/Xe, He/Ar/Xe and Ne/Ar/Xe Mixtures | 20 |
| | 3.5 Scaling of Xenon Laser..... | 23 |
| | 3.6 Concluding Remarks..... | 24 |
| | 3.7 References..... | 38 |
| 4. | SHORT PULSE ELECTRON BEAM EXCITATION OF THE HIGH PRESSURE ATOMIC Ne LASER | 40 |
| | 4.1 Introduction..... | 40 |
| | 4.2 Description of the Experiment..... | 42 |
| | 4.3 Description of the Model..... | 42 |
| | 4.4 Neon Laser Characteristics Using Short Pulse E-Beam Excitation..... | 45 |
| | 4.5 Concluding Remarks..... | 49 |
| | 4.6 References..... | 61 |
| 5. | EXCITATION MECHANISMS AND GAIN MODELING OF THE HIGH PRESSURE ATOMIC Ar LASER IN He/Ar MIXTURES | 63 |
| | 5.1 Introduction..... | 63 |
| | 5.2 Description of Model..... | 64 |
| | 5.3 Parametric Study of the Performance of the Argon Laser..... | 68 |
| | 5.4 Concluding Remarks..... | 72 |
| | 5.5 References..... | 81 |
| 6. | CONCLUSIONS | 83 |

| | |
|--|----|
| APPENDIX. A. LIST OF CHEMICAL SPECIES PERTINENT TO RARE GAS LASERS | 85 |
| APPENDIX. B. LIST OF PLASMA CHEMICAL REACTIONS PERTINENT TO RARE GAS LASERS | 88 |
| B.1 References | 97 |
| VITA | 99 |

1. INTRODUCTION

Rare gas atomic lasers operate with a small mole fraction of lasing atoms and a buffer gas of lower atomic weight. The input energy, which is deposited mostly in the buffer gas, is efficiently transferred to the lasant, since the electronic states of the buffer gas are usually higher in energy than those of the lasant. The fraction of the transferred energies then leads to lasing. Penning ionization and heavy particle quenching of the lower laser level by the buffer gases can increase the efficiency of the laser. Various excitation methods can be used for rare gas lasers including electron-beam pumping, electron-beam-sustained discharge, self-sustained discharge, microwave discharge, and fission-fragment excitation. Experiments have shown that the electron-beam-sustained discharge pumping generally yields the highest efficiency ($> 3\%$). Two to three percent of efficiency can be obtained by self-sustained discharge when X-ray or UV preionization is applied.

The high pressure rare gas lasers have recently gained attention due to their high operating efficiency, excellent optical homogeneity, and long gas lifetime. One of the potential applications of the rare gas lasers is in laser communications. Their beam quality and ability to lase at several lasing transitions, either simultaneously or in different conditions, can be useful in long range atmospheric data communication.¹ The $1.73\ \mu\text{m}$ transition in the atomic Xe laser^{2,3} and $1.79\ \mu\text{m}$ transition in the atomic Ar laser are particularly useful, because of their fitness in an atmospheric transmission window. The atomic Xe laser can also be used in laser surgery, because the 2.63 and $2.65\ \mu\text{m}$ transitions of the Xe laser are almost completely absorbed in water. The Xe laser can be used effectively in tissue cutting. Traditionally, CO_2 lasers were used in laser machining. However, a long gas lifetime, high beam quality and the shorter wavelength of the rare gas lasers provide a strong alternative to CO_2 lasers. Lately, fission-fragment pumped rare gas lasers have also been investigated for defense applications and energy transfer mechanisms in space.

Recent experiments have revealed that the laser parameters such as laser output power and efficiency are sensitive to the small changes in gas mixtures, pump power and operating pressure. Therefore, it is difficult to optimize or predict the performance of the laser for the desired applications with experiments alone. A computer model has been developed to deepen the understanding of laser kinetics and optimize the laser parameters over gas mixtures, power and energy deposition, and pressure. The results from the model have been validated by numerous comparisons with the experimental results over a wide range of parameters. The parametrization of rare gas lasers obtained from computer modeling is particularly useful in optimizing rare gas lasers excited by fission-fragments, because this reduces the numerous high cost experiments which are required to obtain the optimization of rare gas lasers.

From the efforts of modeling, we have identified several common characteristics of the rare gas atomic lasers. The precursors to the laser levels are likely to be dimer ions. Therefore, the formation and destruction of the dimer ions play an important role in the kinetics of the rare gas lasers. The dimer ions are mostly formed by three-body association reaction and are destroyed by dissociative recombination. Dissociative recombination is also a dominant kinetic mechanism for electron loss, instead of the attachment process as in rare gas-halogen mixtures.

The process that clears the lower laser manifold is another important factor in understanding the kinetics of rare gas lasers; the dominant clearing mechanism varies among the different rare gas lasers. In the atomic Xe laser, quenching of the lower laser manifold by the buffer gas is the dominant clearing mechanism. Penning ionization of the lower laser levels by Ar or Kr is used in the atomic Ne laser as the dominant clearing mechanism. Heavy particle quenching and radiative decay are the dominant clearing mechanisms for the lower laser level in the atomic Ar laser. However, if the larger mole fraction of the lasing atoms is used in the gas mixture, self-quenching of the laser levels can reduce the inversion density.

The efficiency of some rare gas lasers approaches its quantum efficiency with respect to the ground state. This phenomenon is explained by the process called "electro-ionization."⁴ When a significant portion of the ions of lasing atoms is produced by the recirculation of the

metastables, it is much more efficient than excitation from the ground state. This recirculation of energies from metastables to ions is called electro-ionization. This phenomenon is found in the atomic Xe and Ar laser, but not in the Ne laser due to the large energy separation in laser levels.

Our computational investigations have yielded a number of significant findings. For the atomic Xe laser, the premature termination of gain has been found before the input power reaches its peak in fission-fragment pumping. From the model, this is most likely attributable to gas heating, which results from high energy loading of the laser. Gas heating increases the electron density, and leads to electron collision quenching (ECM) of the laser levels.

From the modeling of the atomic Ne laser, we found that variations of the electron temperature in the afterglow following the e -beam pulse largely determine the time at which laser oscillation starts. Laser oscillation does not occur until the excited states are depleted and electron temperature decreases, thereby increasing the rate of dissociative recombination.

From the modeling of the atomic Ar laser, the dominant excitation mechanism is identified as the dissociative recombination of HeAr^+ . Collisional-radiative recombination, which used to be thought of as the dominant pumping mechanism, was not significantly affecting laser kinetics due to high electron temperature. The electron temperature is raised by superelastic heating. Also, electro-ionization at high pump rates seems to enhance the efficiency of the atomic Ar laser.

In Chapter 2, the model for rare gas atomic lasers is described in detail by first introducing the basic principle of various pumping mechanisms. Then, the plasma chemical reactions used in the model are described. A discussion on solving the system of rate equations with the computation of electron and gas temperatures and an explanation of the laser cavity model are also included in Chapter 2. The gain modeling of the atomic Xe laser for fission-fragment pumping is described in Chapter 3. The time-dependent small signal gains for both 1.73 and 2.03 μm in Ar/Xe, He/Ar/Xe and Ne/Ar/Xe gas mixtures are computed and compared to the experimental results. The kinetics of the atomic Ne laser in e -beam pumping are

presented in Chapter 4. In addition, the time-dependent laser output with respect to small changes in the gas mixture is discussed. And finally, in Chapter 5, the gain modeling and the excitation mechanisms of the atomic Ar laser will be presented. The laser efficiency over the Ar mole fraction and pressure are computed and compared to the experimental results. A complete list of the chemical species and plasma-chemical reactions used in our model is presented in the appendices.

1.1 References

- ¹ D. H. Hohn, W. Steffens and A. Kohnle, Atmospheric IR Propagation, *Infrared Phys.* **25**, 445 (1985).
- ² G. A. Hebner and G. N. Hays, *J. Appl. Phys.* **73**, 3614 (1993).
- ³ G. A. Hebner and G. N. Hays, *J. Appl. Phys.* **73**, 3627 (1993).
- ⁴ N. G. Basov, V. A. Danilychev, A. Yu. Dudin, D. A. Zayarnyl, N. N. Ustinovsky, I. V. Kholin, and A. Y. Chugunov, *Sov. J. Quantum Electron.* **14**, 1158 (1984).

2. BRIEF DESCRIPTION OF THE MODEL FOR RARE GAS ATOMIC LASERS

2.1 Pumping Mechanisms

Rare gas lasers can operate with various pumping methods^{1,2} including electron beam (*e*-beam), *e*-beam sustained discharge, discharge, microwave, and fission-fragment excitation. The characteristics of three basic pumping mechanisms are discussed below.

In *e*-beam pumped plasma, high energy electrons passing through the gas medium experience elastic and inelastic collisions with the other gas atoms. The electron beams used to excite rare gas lasers have energies ranging from 0.01 to 1.0 MeV. Elastic collisions of the electrons with nuclei of the decelerating medium cause the electrons to be scattered. The geometric dimension of the excitation region and the pump density are influenced by the scattering. The inelastic collisions produce ions and excited state species. A typical electron beam pumped laser consists of a vacuum diode and a laser head. In the vacuum diode electrons are produced by field emissions from a cold cathode and are accelerated by the cathode voltage. These electrons enter the laser chamber and deposit the power (10s-100s kW/cm³).

The fission-fragment pumping described in this work is performed at the SPR-III fast burst reactor at Sandia National Laboratory. The fission neutrons from the reactor were moderated to thermal energies. Then these moderated neutrons induce fission in the enriched uranium oxide (²³⁵UO₂) coatings deposited on removable aluminum plates in the laser cell. A fraction of the fission fragments exited from the coating deposit their energies in the gas through collisions with rare gas atoms.

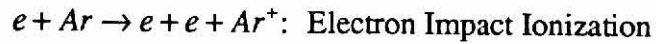
In a self-sustained discharge excitation, the active medium is irradiated with UV or X-ray photons. The discharge in the active medium is initiated by preionization. Then the applied electric fields between the anode and the cathode sustains the discharge. Since the laser output is very sensitive to the homogeneity of the discharge, the laser head and the discharge chamber must be carefully designed to produce a homogeneously pumped discharge region. The efficiency in a self-sustained discharge is generally not as high as in an *e*-beam system.

However, this scheme is more amenable to high-repetition rate operation than electron beam and electron beam sustained excitation.

2.2 Plasma-Chemical Kinetics

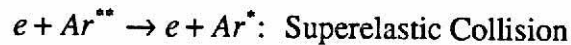
To understand the variations in laser output, power, and efficiency with respect to gas mixtures, pressures, and pump rates, the internal kinetics must be understood. Thus, significant excited and ionic state species are selected and incorporated into the model. The time-dependent changes in number density of such species are represented by plasma-chemical reactions. For different conditions, a different set of reactions becomes more important. The following are brief descriptions of the significant reactions in each rare gas laser plasma.

Electron impact ionization and excitation: Either e -beam electrons or secondary electrons collide with neutral or excited state atoms, producing ions or higher excited states.



For the e -beam plasmas, the rate of excitation and ionization are represented by W -values (energy / event). These values are computed by the Monte Carlo simulation of beam slowing.

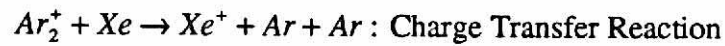
Superelastic collision: Electron quenching of the excited states to either ground state or lower excited states are called super elastic collisions:



The difference in energy between initial and final states is transferred to the electron as kinetic energy. Therefore, the electron temperature rises due to the superelastic heating effect.

Charge Transfer and Excitation Transfer Reactions: Collisions between ions and neutral atoms resulting in ionization of the neutral atoms are called charge transfer reactions. Collisions

between the excited state atoms and a neutral atom resulting in excitation of the neutral atom are called energy transfer reactions.



Charge transfer occurring between the dimer ions and the atoms with lower ionization potential is the dominant charge transfer reaction between the buffer gas and the lasant.

Three-Body Association Reaction: Three-body collision between an ion and two neutrals producing the dimer ions is called a Three-body Association Reaction:



The dimer ions in rare gas lasers are important due to their role as a precursor to the laser levels. The dominant mechanism which produces the dimer ions in rare gas lasers is the three-body association reaction.

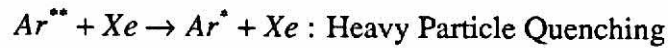
Dissociative Recombination Reaction: The capture of low energy electrons by the dimers resulting in excited states is called dissociative recombination.



This is the dominant mechanism for the excitation of upper laser levels. The branching ratios of dissociative recombination strongly determine the lasing characteristics of the laser. Since this is the dominant mechanism for electron consumption, understanding this reaction is one of the most important aspects of understanding the excitation mechanisms of the rare gas lasers. The heterogeneous dimers such as $HeAr^+$ usually have a lower potential well than the more strongly bound homogeneous dimers such as Ar_2^+ . Therefore, the heterodimers, such as $HeAr^+$, tend to

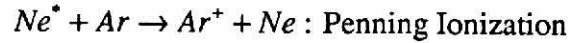
produce the upper laser levels or higher excited states of Ar. The branching of dissociative recombination of homogeneous dimers, such as Ar_2^+ , is greater for the lower laser manifold and metastables of Ar. Also, the rates of these reactions depend on the electron and gas temperatures.

Heavy Particle Quenching: Collisions between excited state species with neutral atoms resulting in lower or higher excited states are known as heavy particle quenching:



Lower laser levels in the atomic Xe lasers are cleared by heavy particle quenching of the buffer gas. The state selectivity of the quenching is responsible for the dominant transition of the Xe laser.

Penning Ionization: Excited state species colliding with a neutral atom with lower ionization potential results in the ionization of the neutral:



In the atomic Ne laser, Penning ionization is the dominant mechanism to clear its lower laser levels.

Radiative Decay: When excited states decay to either ground state or lower excited states and produce a photon. This is known as radiative decay:



The complete list of rate constants used in our model is listed in Appendix B.

2.3. Rate Equations

In a laser plasma, numerous chemical species including photons and electrons participate in the destructive and formative collisions. If there are N chemical species involved in M chemical reactions, the rate equations for these chemical species are:

$$\frac{dn_i(t)}{dt} = \sum_{j=1}^M (v_i^j - \mu_i^j) \left\{ k_j \prod_{\alpha=1}^N n_{\alpha}(t)^{\mu_{\alpha}^j} - k_{-j} \prod_{\alpha=1}^N n_{\alpha}(t)^{v_{\alpha}^j} \right\}$$

where n_{α} is the number density of the chemical reaction α ; k_j and k_{-j} are the rate coefficients of the forward and backward reactions; and μ_{α}^j and v_{α}^j are the absolute values of the stoichiometric coefficients of the reaction j .

The temporal evolution of any chemical species including the photons is represented by the corresponding rate equations. The rate constants for the rate equations are first compiled from the literature and used in the model. The system of rate equations forms the system of coupled nonlinear ordinary differential equations. Since most of the rate coefficients are dependent on either the electron and/or gas temperature, most of them must be continuously updated during simulation. The time integration of the rate equations is performed using the third-order Runge-Kutta method. The integration step size Δt used in our laser code is adjusted automatically by the code itself. The criterion for this adjustment is based on limiting the fastest changes in number density of the species. The rate equations provide the time-dependent number densities for all excited and ionic states in the laser plasma.

2.4. Electron Temperature and Gas Temperature Modeling

The table of electron temperature is computed prior to the actual time integration of the rate equations. The Monte Carlo solver uses the information such as gas mixture, power deposition, pressure and fractional ionization to solve for the average electron temperature for the laser plasma. Then, for each time iteration, the electron temperature is interpolated from the

table. The rates of electron impact excitation and electron collision mixing are sensitive to the variations in electron temperature.

The increase in gas temperature in rare gas lasers is basically due to high energy deposition to the medium. For example, with a power deposition of 100's of W/(cm³ atm), over a time of 100's of μ s and netting an energy deposition of tens of joules per atmosphere, the gas temperature increases by 100's K. A few of the most sensitive reactions for the gas temperature are three-body association and dissociative recombination. The increase in gas temperature decreases the rate coefficients for three-body association reactions. The temperature dependence of the three-body association rate has been estimated from previous parametric studies to be $T_{gas}^{-1.5}$. The rate of dissociative recombination also decreases with increasing gas temperature, thereby further reducing the pumping of the upper level.

2.5 References

- ¹ R. L. Rhoades and J. T. Verdeyen, Appl. Phys. Lett. **60**, 2951 (1992).
- ² N. G. Basov and V. A. Danilychev, Sov. Phys. Usp. **29**, 31 (1986).

3. PREDICTIONS FOR GAIN IN THE FISSION-FRAGMENT-EXCITED ATOMIC XENON LASER

3.1. Introduction

During the past few years, there has been a renewed interest in the atomic xenon laser as an efficient source of infrared radiation. The atomic xenon laser is capable of operating at high efficiency ($\leq 5\%$) over a wide range of pump rates (10s of W cm^{-3} to 10s of kW cm^{-3}).¹⁻¹¹ The gas mixtures typically contain a small fraction of xenon (less than a few percent) in rare gas buffers at pressures of 0.5-5 atm. Various excitation methods have been used including electron-beam pumping,^{2,5} electron-beam-sustained discharge,⁶ self-sustained discharge,⁷ microwave discharge,⁸ and fission-fragment excitation.⁹⁻¹¹

The atomic xenon laser is most often operated on one or more of six infrared transitions between 1.73 and 3.65 μm corresponding to transitions between the 5d and 6p manifolds. Inversion mechanisms and the energy loading effects of the atomic xenon laser using Ar/Xe mixtures have been previously discussed in the context of electron beam and fission-fragment pumping.^{12,13} In summary, excitation of the upper laser levels ($5d[3/2]_1$ and $5d[5/2]_2$), is believed to occur as a result of a collisional-radiative cascade following dissociative recombination of ArXe^+ , and electron impact excitation from $\text{Xe}(6s)$.¹² (See Fig. 3.1. Tables and figures appear at the end of each chapter.) The depopulation of the lower laser levels ($6p[1/2]_0$, $6p[3/2]_1$, $6p[5/2]_2$) occurs by radiative relaxation or collisional quenching by heavy particles to the 6s levels. The intrinsic efficiency of the Ar/Xe laser, measured as high as 5%, is comparable to the quantum efficiency of the 1.73 μm transition, which is $\approx 7\%$. An explanation of this phenomenon was first proposed by Lawton et al.¹ and Basov et al.² as being the recirculation of xenon atoms by electron-impact ionization from the 6s or higher levels to $\text{Xe}(5d)$ and Xe^+ , followed by association reactions forming ArXe^+ . This provides for a much more efficient path than direct electron-impact excitation of the ground state of xenon. This recirculation has been called electro-ionization.¹⁻³ The quantum efficiency based on the electro-ionization cycle is $\approx 30\%$. Results from our model of the xenon laser indicate that 20-30% of

Xe^+ is formed by electron impact of $\text{Xe}(6s)$ and $\text{Xe}(6s')$, with a comparable amount of excitation occurring from $\text{Xe}(6s)$ and $\text{Xe}(6s')$ to higher excited states.

The selective nature of heavy particle quenching of the $\text{Xe}(6p)$ manifold by different buffer gases explains, in part, the spectrum of the laser output in a broad band optical cavity.^{9,11} The 1.73, 2.03 and 2.65 μm Xe transitions share a common upper laser level. Therefore, as a first-order approximation, the dominant wavelength is determined by the quenching of the lower laser level. In Ar/Xe gas mixtures, the common lower laser level of the 1.73 and 2.63 μm transitions ($6p[5/2]_2$) is quenched by argon sufficiently fast so that both lines may simultaneously oscillate at the expense of the 2.03 μm transition whose lower laser level ($6p[3/2]_1$) is not strongly quenched. In helium-buffered gas mixtures, helium preferentially quenches the lower level of the 2.03 μm transition, initiating a cascade which ultimately populates the lower level of the 1.73 μm transition.¹¹ The 2.03 μm transition also has a higher oscillator strength than the 1.73 μm transition. These conditions allow the 2.03 μm transition to oscillate in He/Ar/Xe mixtures having only 5%-20% of helium in a broad band optical cavity.^{7,11}

Due to the high oscillator strengths of the laser transitions and a close match between the electron temperature and energy separation between the laser levels, the performance of the atomic xenon laser is sensitive to the effects of electron collision mixing (ECM).¹² We have previously proposed that at high power or energy loading, ECM thermalizes the laser levels and terminates oscillation when the fractional ionization exceeds 10^{-6} , depending on the gas pressure and power deposition. The effects of high energy loading, or gas heating, are also related to ECM. At a constant pump rate, increasing the gas temperature increases the electron density as a result of decreasing rates of dissociative recombination of the dimer ions.¹² Therefore, laser performance may degrade at a constant pump rate when gas heating increases the electron density above a critical value.

A compilation of the experimental results from a number of different systems using different pumping mechanisms has shown that the saturation intensity of the xenon laser scales

as $P^{0.6}$, where P is the specific power deposition.¹² The implication of these results is that broadening of the transition is predominantly a result of electron collisions since the electron density scales roughly as $P^{0.5}$ in recombination-dominated plasmas. Unfortunately, the combined effects of increased rates of excitation of the upper laser level and increased mixing of the laser levels with increasing pump rates (electron density) complicate the interpretation of both experimental and theoretical results. For example, the saturation intensity of the xenon laser at low pump rates is only 10s $\text{W}\cdot\text{cm}^{-2}$. This results in the laser operating highly saturated under most conditions. Comparing laser output power between model and experiment therefore does not independently yield information on either saturation intensity or gain. This results from the fact that under highly saturated conditions, laser power scales as $g_0 I_s$ (g_0 is the small signal gain, I_s is the saturation intensity). Recently, however, direct measurements of gain at 1.73 and 2.03 μm have been made in a fission-fragment excited atomic xenon laser operating at low pump power (\leq tens of $\text{W}\cdot\text{cm}^{-3}$) at near-atmospheric pressure.^{14,15} These measurements, combined with computer modeling, have enabled us to refine our understanding of the kinetics of the atomic xenon laser.

In this thesis, gain and broadening of the 1.73 and 2.03 μm transitions of the atomic xenon laser using rare-gas buffers are investigated using a computer model. Results from the model are compared to experimental measurements of gain made in fission-fragment-excited Ar/Xe, Ar/He/Xe and Ar/Ne/Xe gas mixtures. The pumping mechanisms used in the model have been validated by comparing results of the model for laser power to experiments under saturated conditions. The comparisons made here provide an opportunity to test predictions of broadening coefficients and other kinetics parameters¹² such as the effects of gas heating, pump rate and gas pressure at low pump rates. In this work, we found that products of the quenching of the $\text{Xe}(6p[3/2]_1)$ level by argon must remain in the $6p$ manifold, as opposed to directly branching to the $6s$ levels, in order to explain the onset of absorption at high energy loading. Our results also suggest that the temperature dependence of three-body association reactions

must also scale moderately with gas temperature ($T_g^{-1.5}$) to reproduce experimentally observed absorption at the laser wavelengths.

The computer model and experiments used in this study are described in Section 3.2. Quantities derived from the model are discussed in Section 3.3, followed by a comparison of computed and experimental values of gain for Ar/Xe, He/Ar/Xe and Ne/Ar/Xe mixtures in Section 3.4. Scaling laws for the relation between gain, pump power and energy deposition are proposed in Section 3.5, followed by our concluding remarks in Section 3.6.

3.2 Description of Model and Experiment

The basic components of our computer model for the fission fragment excited laser has been previously discussed in Refs. 11-13, and therefore will be only briefly described here. The model is conceptually similar to other models for particle-beam-excited excimer lasers. Additional levels of the rare gas are included to resolve the laser transitions. Eight levels in the $5d$ manifold and six levels in the $6p$ manifold of xenon are included in addition to the $6s$ and $6s'$ levels, a combined $7s/7p$ state, and a lumped excited state located at 11.5 eV representing radiating levels at higher energies. A listing of other species and reactions in the model can be found in Refs. 11 and 12. The model includes five laser transitions between the $5d$ and $6p$ manifolds: 1.73, 2.03, 2.63, 2.65, and 3.37 μm . The collisional broadening of these transitions by heavy particles and electrons is assumed to produce Lorentzian line shapes.

In fission-fragment excitation, the plasma is generated by the slowing of energetic heavy ions in the laser gas mixture. In these experiments, described below, the heavy ions are produced by the fissioning of uranium foils lining the laser cavity. The ions are produced with two characteristic energies averaging 99 MeV and 68 MeV. The heavy ions predominantly slow by ionizing the gas which generates energetic secondary electrons, which also ionize and excite the gas. The model includes a calculation of the W values (energy deposition/event) for ionization and excitation of all levels of each component of the gas mixture by the heavy ions. This calculation is performed with a Monte Carlo simulation for the injected particles and

secondary electrons¹⁶ for individual gas mixtures. This calculation is necessary since W values are not simple functions of the gas mixture when the ionization potentials of the constituents are markedly different. Although these W values are calculated based on electron beam excitation, previous work has shown that W values for heavy ions differ by only 10% from those for electrons, and are usually larger.¹⁷

Since the pumping pulse in the fission-fragment-excited system of interest is approximately 2-10 ms long, a direct time-dependent calculation of the gain is computationally impractical. Therefore, model predictions were made at discrete points in the pump profile, integrating the rate equations for each species to their quasi-steady-state values (which are reached in 5-15 μ s). The initial conditions for each of these discrete calculations include the gas temperature and power deposition, which is corrected for the gas motion. The gas temperature was calculated based on the integrated energy deposition in the gas to the time of interest. This latter assumption is only an approximation since calculations of the power deposition and hydrodynamics of the gain cell show that there is some gas motion into cool, unpumped regions.¹⁸

The dominant sources of ionization in particle-beam excited plasmas are the impact of ground state species by the injected particles and energy energetic secondary electrons. These sources do not directly depend on the bulk electron temperature T_e . The electron temperature does, however, impact the kinetics since quenching, recombination and multistep ionization rates are dependent on its value. In electron-beam-excited gas mixtures, the electron temperature is determined by the energy at which electrons recombine or attach. In rare gas-halogen gas mixtures where attachment is the dominant loss mechanism, the rate of electron loss is only a weak function of plasma density, and hence power deposition. In rare gas mixtures, recombination is the dominant loss mechanism. Therefore, the rate of electron loss is proportional to the plasma density, which in turn depends on power deposition.

We determined the electron temperature by using a Monte Carlo simulation (MCS) while including collisions with excited states and ions for a given gas mixture.¹⁶ We

parameterized the MCS to obtain a table of T_e as a function of excited state, electron densities, and gas mixture. This table was then interpolated during the actual calculation. Examples of these results for Ar/Xe and He/Ar/Xe mixtures are shown in Fig. 3.2. Electron temperature is lower in He-buffered mixtures compared to Ar/Xe mixtures due to the larger rate of momentum transfer afforded by the lighter He. In all cases, T_e increases with increasing fractional ionization since the rate of recombination increases with the square of the fractional ionization, and recombination preferentially depletes the lower part of the electron energy distribution. These results are therefore analogous to the heating of the electron distribution which occurs when using large mole fractions of a thermal electron attaching gas such as F_2 .¹⁶ Although low-powered particle beam excited plasmas are often thought of as having rather cool temperatures, at fractional ionizations exceeding 10^{-5} the temperature can exceed 1 eV. This value is commensurate with those found in e-beam-pumped rare-gas halogen gas mixtures. Briefly, the experiments were conducted using the Sandia Pulsed Reactor III (SPR III). The experimental apparatus is described in detail in Refs. 9, 11 and 19-21. The active pumped volume of the laser cell is $60 \times 1 \times 7 \text{ cm}^3$, and the cell is equipped with Brewster angle windows made of quartz. Fission fragments from the $^{235}\text{UO}_2$ foils lining the cavity are generated by neutron pulses from the reactor having pulse lengths of 0.5-5 ms full-width half-maximum (FWHM). The power deposition is obtained by normalizing the thermal neutron signals observed with a Reuter-Stokes cobalt detector to the energy deposition obtained by pressure rise. The pressure rise was corrected for thermally generated gas motion into unpumped regions of the cell as predicted by solving the Navier-Stokes equations for the convective gas motion.¹⁸ These corrections increased the power deposition by 25%-40% compared to the value one would obtain from the pressure rise alone. Gain was measured using an F-center laser operating at $1.73 \text{ }\mu\text{m}$ or a longitudinally excited electric discharge laser He/Xe laser operating at $2.03 \text{ }\mu\text{m}$.²² A detailed discussion of the experimentally measured small signal gain as a function of gas mixture, pressure and pump power will be presented elsewhere.²²

3.3 Derived Rate Coefficients and Processes

3.3.1 Broadening rate coefficients

Predictions of laser power and intrinsic laser efficiency have been previously validated based on comparisons of our model's results with experiments performed on electron-beam-excited and fission-fragment-excited lasers.^{11,12} Based on these comparisons, our proposed kinetic population mechanisms, including the effects of gas heating and ECM, have some credence. The predicted saturated output power is proportional to $g_0 I_s$. This value is somewhat independent of broadening since g_0 is inversely proportional to the broadening of the transition ($\Delta\nu$) while I_s is proportional to that broadening. Therefore, to first order, a kinetically consistent broadening coefficient for the laser transitions cannot be validated from comparisons based on laser power or energy; validation requires independent measurements of gain. The collisional broadening coefficients for the 1.73,^{15,19} 3.36,²³ and 3.5 μm (Ref. 24) transitions have been reported by others. A subset of those broadening coefficients are shown in Table 3.1.

The values of the pressure broadening rate coefficients for the 1.73 μm transition used in the model were obtained by normalizing the predicted gain to the maximum value obtained in the experiments. The broadening coefficients thus obtained are also shown in Table 3.1. They differ from experimental values by less than 20%, except for the helium. The derived broadening coefficients in helium are lower by approximately half than those of the experiment. We attribute this to the fact that the electron density and electron temperature are closely coupled. Increases of the electron temperature of a few tenths of an eV can increase the electron density by a factor of 2. The total broadening is the result of both heavy particle and electron collisions, the latter of which also quenches the inversion. Small uncertainties in the electron temperature therefore ultimately affect our derived broadening coefficients by electrons.

Although this procedure was sufficient to reproduce the maximum experimental gain for a variety of gas mixtures and pump rates, agreement could not be obtained over the entire length of the pulse without considering other kinetic processes.

3.3.2 Energy loading and gas temperature effects

Experiments by A. Voinov et al.^{25,26} on the fission-pumped Ar/Xe laser showed that the laser output reached a maximum prior to the maximum of the pumping pulse. Similar trends have been observed by Hebner and Hays^{14,15} for laser power and for laser gain, as discussed in this thesis. The gain and laser power deviates from being proportional to the power deposition, very often decreasing and the gain turning to absorption before the pump pulse reaches a maximum. Voinov et al.²⁵ proposed that the premature termination of the laser power results from disruption of the optical quality of the gas. Calculations and experiments were performed on the optical quality of our laser gas mixtures during reactor pumping.²⁷ The results indicated that the optical homogeneity is not significantly degraded for the pump rates and pressures of interest. For our conditions, the degradation in gain most likely results from energy loading, a rise in gas temperature and a coincident rise in electron density. We have previously proposed that laser oscillation in the Xe laser is quenched by electron collision mixing of the laser levels when the electron density increases above a critical fractional ionization of 5×10^{-6} - 10^{-5} .¹² If the mixing is sufficiently large, the termination of laser oscillation, and gain, may be followed by absorption.

The sensitivity of laser performance to gas temperature is tied to the effects of ECM. In rare-gas mixtures, the electron density is determined by a balance between ionization and recombination. At a constant power deposition, the rate of ionization is independent of gas temperature. For this system, the loss of electrons is dominated by dissociative recombination of dimer ions. The rate coefficient for association of dimer ions, a three-body process, scales approximately as T_g^{-N} .²⁸ Rate coefficients for dissociative recombination also decrease with increasing temperature. As a result, the electron density increases with increasing gas temperature due to a decreased density of dimer ions (relative to monomer ions) that recombine more slowly, even though the source due to ionization is constant.

We performed a parametric survey with our model in which we investigated the temperature dependence of a variety of heavy particle processes. We determined that the time

(corresponding to a given energy loading or gas temperature) at which gain terminates is most sensitive to the temperature dependence of the three-body association reactions for forming dimer ions. The important reactions in Ar/Xe mixtures are $\text{Ar}^+ + \text{Ar} + \text{M} \rightarrow \text{Ar}_2^+ + \text{M}$, $\text{Xe}^+ + \text{Ar} \rightarrow \text{ArXe}^+ + \text{M}$ and $\text{Xe}^+ + \text{Xe} + \text{M} \rightarrow \text{Xe}_2^+ + \text{M}$. Measurements and theoretical studies of this process for a variety of ions have yielded dependencies of $T_g^{-0.5}$ - $T_g^{-2.5}$. Typical results from our parametric survey in which we varied the temperature dependence of ion association reactions (T_g^{-N} , $1.5 \leq N \leq 3.0$) are shown in Fig. 3.3. We plotted our predictions with experimental results for gain at 2.03 μm in a fission fragment excited Ar/Xe = 99.7/0.3 gas mixture. The gas pressure was 530 Torr and the maximum power deposition was 87 W cm^{-3} . The peak gain is well reproduced for all temperature dependencies, that is, for all values of N . The transition to, and magnitude of, the absorption, however, are sensitive to the temperature dependence of dimer ion association ($T_g \approx 550$ K at maximum absorption). We reproduce experimental results with a temperature dependence of $T_g^{-1.5}$. The underprediction of gain at the leading edge of the pulse is discussed below.

3.3.3 Effects of branching of heavy particle quenching of Xe(6p)

The high efficiency of the atomic Xe laser is partly due to the rapid depopulation of the Xe(6p) manifold (lower laser levels) to other levels in the Xe(6p) manifold or to the 6s manifold by collisional quenching by argon and helium. Out of the seven infrared transitions between the 5d and 6p manifold, only one laser line is usually dominant, either the 1.73 or 2.03 μm line. This behavior is due, in part, to gain saturation and, in part, to selective quenching of the lower laser levels of the 1.73 and 2.03 μm transitions by argon and helium, respectively. Quenching rate constants and primary product state assignments have been reported for the deactivation of Xe(6p) states in Ar using one-photon excitation in the afterglow of a pulsed discharge and two-photon excitation in a static cell.²⁹⁻³¹ The quenching rate coefficients used in the model for Xe(6p) levels are shown in Table 3.2. Quenching of the 6p and 5d manifolds of xenon may also occur by three-body collisions. Analysis of the molecular potentials and curve crossing for Xe_2^* suggests that three-body collisions of Xe atoms in the 5d manifold with ground-state xenon do

not result in dimerization but predissociate to $\text{Xe}(6s)$. A similar process is likely to occur for the higher levels of $\text{Xe}(6p)$, while the lower levels of $\text{Xe}(6p)$, $\text{Xe}(6p')$, and $\text{Xe}(6s)$ most likely dimerize.

The validity of these quenching coefficients and their branchings in the context of our model are obviously important factors in predicting gain. For example, at the beginning of our study, the total rate coefficients for quenching of $\text{Xe}(6p)$ by Ar had been measured; however, their branchings were not known. If one proposes that the branchings of the quenching of $\text{Xe}(6p[3/2]_2)$ are exclusively to $\text{Xe}(6s)$ levels, as in quenching by xenon, the predicted gain (Trace A in Fig. 3.4) decreases at the same time as observed in the experiments. However, the peak gain is larger than experiments and absorption is not predicted. If, instead, the branchings are to other levels in the $6p$ manifold, as later recommended in Ref. 29, the predictions for gain are in good agreement with the experiment. These results imply that the onset of absorption results, at least in part, from a bottlenecking of density in the $\text{Xe}(6p)$ manifold. Bottlenecking in the lower laser manifold coupled with ECM with the $\text{Xe}(5s)$ manifold thermalizes the laser levels, terminates the gain and may result in absorption.

The uniqueness of the parameters we have derived in this exercise are certainly an issue. One could hypothesize other processes which could reproduce the experimental results. Given, however, the uncertainties in the reactor experiments, uncertainties in the existing database of rate coefficients, and the good agreement we have obtained between our model and experimental results, we believe our reaction scheme captures the essential physics while not necessarily being unique.

3.4 Analysis of Gain for Ar/Xe, He/Ar/Xe and Ne/Ar/Xe Mixtures

Predictions of gain compared to experiment for the $2.03 \mu\text{m}$ transition in Ar/Xe = 99.7/0.3 mixtures are shown in Figs. 3.5 and 3.6. The initial gas pressure was approximately 530 Torr and the maximum power deposition is approximately 87 W cm^{-3} . The peak gain and the onset of absorption are reproduced. The peak gain occurs prior to the maximum pump rate,

while the absorption increases with increasing pump rates. The reason for the cutoff and onset of absorption is thermalization of the laser levels ($5d$ and $6p$ manifolds) resulting from electron-collision mixing and some additional amount of excitation from $\text{Xe}(6s)$ to $\text{Xe}(6p)$. The higher pump rate results not only in a higher electron density but also higher gas temperatures which, for the reasons discussed above, increase the electron density to even a larger value.

The predictions for gain shown in Fig. 3.5 differ from those in Fig. 3.3 at the leading edge of the pump pulse. Our model had underpredicted gain in the leading edge of the pump pulse where power deposition is $< 10 \text{ W cm}^{-3}$. The fact that experimental measurements of gain at the leading edge were unexpectedly high prompted a reexamination of the response of the thermal neutron detector at low pump powers. At low neutron flux, the cobalt detector is sensitive to the gamma ray flash produced by the reactor. This exercise resulted in a renormalization of the detector response, increasing the implied power deposition by approximately a factor of 2 at values $< 10 \text{ W}$. With this renormalization, the agreement with experiment is markedly improved.

Additional comparisons of predictions of gain with experiments for both the 1.73 and $2.03 \mu\text{m}$ transitions in an $\text{Ar/Xe} = 99.7/0.3$ mixture are shown in Fig. 3.6. The initial gas pressure was $\approx 520 \text{ Torr}$ and the maximum power deposition was $\approx 44\text{-}50 \text{ W cm}^{-3}$. Gains at 1.73 and $2.03 \mu\text{m}$ were measured on different reactor pulses. The dynamics of the SPR III reactor result in lower peak power pulses having longer pulse lengths. The peak gain occurs prior to the peak pump power for both the 2.03 and $1.73 \mu\text{m}$ transitions. The peak gain with a maximum pump power of 87 W cm^{-3} occurs at approximately 46 W cm^{-3} whereas that at a peak pump power of 44 W cm^{-3} occurs at approximately 33 W cm^{-3} . The values of the peak gain, approximately 0.03 cm^{-1} , are almost the same in both cases. Since the pulse length at the lower pump rate is somewhat longer, the onset of absorption occurs at almost identical amounts of energy deposition, approximately $45\text{-}50 \text{ J/l}$.

The predicted and experimental gain at $1.73 \mu\text{m}$ have peak values of approximately 0.01 cm^{-1} . In general, gain on the $1.73 \mu\text{m}$ transition is $0.3\text{-}0.5$ that of the $2.03 \mu\text{m}$ transition in

spite of the higher rate of quenching of the lower laser level of the 1.73 μm . This indicates that bottlenecking in the lower level ($6p[5/2]_2$), at least prior to cutoff, is not a limiting factor. The higher gain at 2.03 μm is largely a result of the higher oscillator strength for that transition.

Comparisons of gain for a He/Ar/Xe mixture are shown in Fig. 3.7 for the 1.73 and 2.03 μm lines, respectively. The gas mixture is He/Ar/Xe = 49.4/50.3/0.3 at a total pressure of 1034 Torr with peak pumping powers of 50-60 W cm^{-3} . The trends are similar to that for the Ar/Xe mixtures, except that the gain on the 2.03 μm transition is, on a relative basis, larger than the 1.73 μm due to the more favorable rate of quenching of its lower laser level by He. The predicted peak gain for 2.03 μm agrees well with experiment while that for 1.73 μm is 10%-20% lower than that obtained in the experiments. The predicted values are quite sensitive to small changes in electron temperature and power deposition, as explained in the previous section. Due to the higher heat capacity resulting from adding helium, the gas heating which results in cutoff of the gain is reduced, allowing the gain pulse to nearly track the pumping pulse. Peak gain still occurs somewhat prior to the peak of the pump pulse though the onset of absorption is significantly delayed, if it occurs at all. The specific energy deposition at which absorption occurs is approximately 80 J/l-atm, somewhat larger than that for the Ar/Xe mixtures, which is approximately 68 J/l-atm.

Comparisons of the model and experimental results for gain at 2.03 μm in a Ne/Ar/Xe = 33/66.7/0.3 gas mixture are shown in Fig. 3.8. The peak pump power is 30 W cm^{-3} and initial gas pressure is 776 Torr. The gain is comparable to that obtained in He/Ar/Xe mixtures. The gain also prematurely peaks in this mixture; however, the added heat capacity provided by the addition of Ne to the mixture lengthens the gain pulse to nearly the entire duration of the pumping pulse (100 J/l-atm). We found from results of the model that the gain in Ne/Ar/Xe mixtures is quite sensitive to the rate of Penning ionization of Xe ions by Ne-excited states. The curve labeled A in Fig. 3.8 was obtained using a rate coefficient of $2 \times 10^{-10} \text{ cm}^3 \text{ s}^{-1}$ for this Penning process, while the curve labeled B was obtained using a rate coefficient of $1 \times 10^{-11} \text{ cm}^3 \text{ s}^{-1}$. Since Ne is not a particularly rapid, nor selective, quencher of Xe($6p$), the addition of

Ne to the gas mixture can only decrease gain by intercepting power which would otherwise channel to the upper laser levels. A rapid transfer of excitation between Ne and Xe, particularly Xe ions, prevents parasitic processes such as the formation of Ne dimers and radiative relaxation, from decreasing the inversion density.

3.5 Scaling of Xenon Laser

Similar gains in the Xe laser are obtained at similar specific power and energy depositions. For example, gains from three separate experiments are plotted in Fig. 3.9 for different Ne/Ar/Xe mixtures: Ne/Ar/Xe = 33.3/66.4/0.3, 0.286 atm, 39 W cm^{-3} ; 66.5/33.3/0.2, 0.381 atm, 43 W cm^{-3} ; and Ne/Ar/Xe = 74.4/24.5/0.1, 0.572 atm, 46 W cm^{-3} . The diameter of the circles in Fig. 3.9 represents the relative magnitude of gain, whereas the location of the circles corresponds to the power and energy deposition of that particular experiment. Within experimental uncertainties, similar gains are obtained at similar locations in the specific power ($\text{W/cm}^3 \text{ atm}$) and specific energy deposition ($\text{J/cm}^3 \text{ atm}$) parameter space. Unfortunately, the experiments are restricted to nearly the same trajectory in the power-energy deposition plane since the shape of the pumping pulse is not easily controlled in reactor experiments.

To alleviate this restriction and to derive scaling laws for the Xe laser, the following computer experiments were performed. The gains at 1.73 and 2.03 μm were calculated for a variety of gas mixtures while independently varying the power and energy deposition. The range of values in the survey were $5 \leq P (\text{W/cm}^3) \leq 30$ and $50 \leq E (\text{mJ/cm}^3) \leq 150$. We restricted ourselves to conditions which correspond to being prior to the cutoff observed in gain. We then searched for a scaling parameter based on the logic that increased pump power increases gain whereas increasing energy deposition decreases gain due to gas heating. This lead to the general form $g_0 \sim P/(E+b)^c$ where b and c are constants. The results of that survey in comparison to experiments are shown in Fig. 3.10. Circles and triangles are results from the model from a variety of combinations of P and E . The lines are the proposed scaling laws.

We found that in Ar/Xe mixtures (0.69 atm), the data were fit well by g_0 (10^{-2} cm^{-1}) = $P/(E+100)^{0.8}$ at $1.73 \text{ } \mu\text{m}$, and $P/(E+100)^{0.5}$ at $2.03 \text{ } \mu\text{m}$. The characteristic energy deposition for reduction in the gain is then approximately 50 J/l-atm , or a temperature rise of approximately 100 K . Although the gain at $1.73 \text{ } \mu\text{m}$ is lower than $2.03 \text{ } \mu\text{m}$, it appears to be less sensitive to energy deposition than is the $2.03 \text{ } \mu\text{m}$ transition, as borne out by the experimental results in Fig. 3.9. Similar gain scalings were obtained for He/Ar/Xe mixtures (0.69 atm), as shown in Fig. 3.10(b). The scaling relationship we derived is $g_0 \propto P/(E+100)^{0.8}$. These scaling relationships are valid for P and E prior to the premature cutoff in gain.

3.6 Concluding Remarks

Gain predictions for the xenon laser from a plasma kinetics computer model have been presented and compared with experiments from fission fragment excitation of Ar/Xe, He/Ar/Xe and Ne/Ar/Xe mixtures. Gain predictions at pump powers of 10s W cm^{-3} and energy loadings of 10s mJ cm^{-3} agree well with experiments. We determined that the products of quenching of Xe($6p$) levels by Ar likely remain in the $6p$ manifold. We also derived an effective gas temperature dependence for three-body ion association reactions, $T_g^{-3/2}$. Scaling laws were proposed for low power, high energy deposition pumping of the xenon laser prior to the cutoff in gain. The proposed scaling law is $P/(E+100)^n$, where P is specific power deposition ($\text{W/cm}^3 \text{ atm}$) and E is specific energy deposition ($\text{mJ/cm}^3 \text{ atm}$). These scalings reflect that gain increases with increasing pump rate but decrease with increasing energy deposition due to the effects of gas heating.

Table 3.1. Collisional broadening coefficient for $\text{Xe}(5d[3/2]_1-6p[3/2]_1)$.

| <u>Collision partner</u> | <u>Value derived from</u> <u>model</u> (cm^3s^{-1}) | <u>Experimental</u> <u>value</u> (cm^3s^{-1}) (Refs. 15 and 19) |
|--------------------------|--|---|
| He | 4.0×10^{-10} | 6.5×10^{-10} |
| Ne | 5.0×10^{-10} | 5.0×10^{-10} |
| Ar | 8.0×10^{-10} | 6.2×10^{-10} |

Table 3.2. Quenching rate coefficients for Xe (6p) used in the model (cm^3s^{-1}).

| <u>Xe(6p)</u> | <u>Collision partner</u> | | |
|--------------------|--------------------------|------------------------|------------------------|
| | <u>He</u> ^a | <u>Ne</u> ^a | <u>Ar</u> ^b |
| [1/2] ₀ | 6.0×10^{-12} | 3.4×10^{-11} | 1.4×10^{-10} |
| [3/2] ₂ | 1.7×10^{-12} | 4.7×10^{-13} | 3.8×10^{-11} |
| [3/2] ₁ | 7.49×10^{-11} | 2.0×10^{-13} | 1.1×10^{-11} |
| [5/2] ₃ | 1.0×10^{-11} | 3.0×10^{-12} | 3.5×10^{-11} |
| [5/2] ₂ | 9.2×10^{-12} | 6.6×10^{-12} | 1.0×10^{-10} |
| [1/2] ₁ | 4.0×10^{-11} | 3.0×10^{-12} | 6.0×10^{-12} |

^a See Ref. 30.^b See Ref. 24.

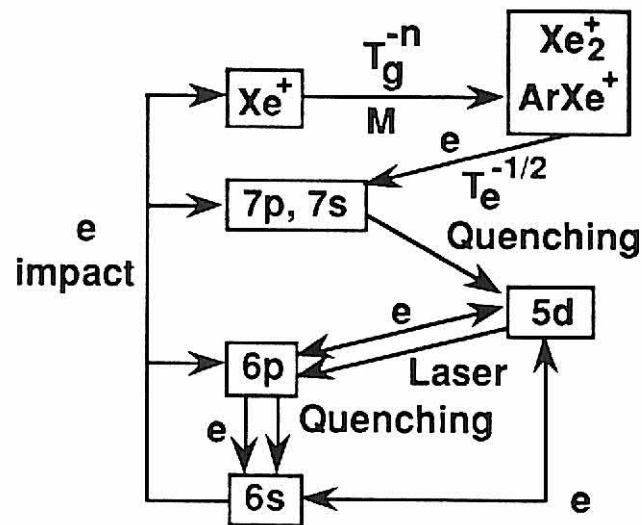


Fig. 3.1. Schematic of the inversion mechanism showing significant kinetic pathways in the Xe laser in Ar/Xe mixtures. Xe^+ forms Xe_2^+ and ArXe^+ through three-body association reactions. Dissociative recombination populates excited states of Xe which by a collisional radiative cascade pump the upper laser levels [Xe(5d)]. Electron collision mixing of the Xe(5d) and Xe(6p), and electron impact excitation from the Xe(6s) contribute towards reducing gain at high pump powers and energy deposition.

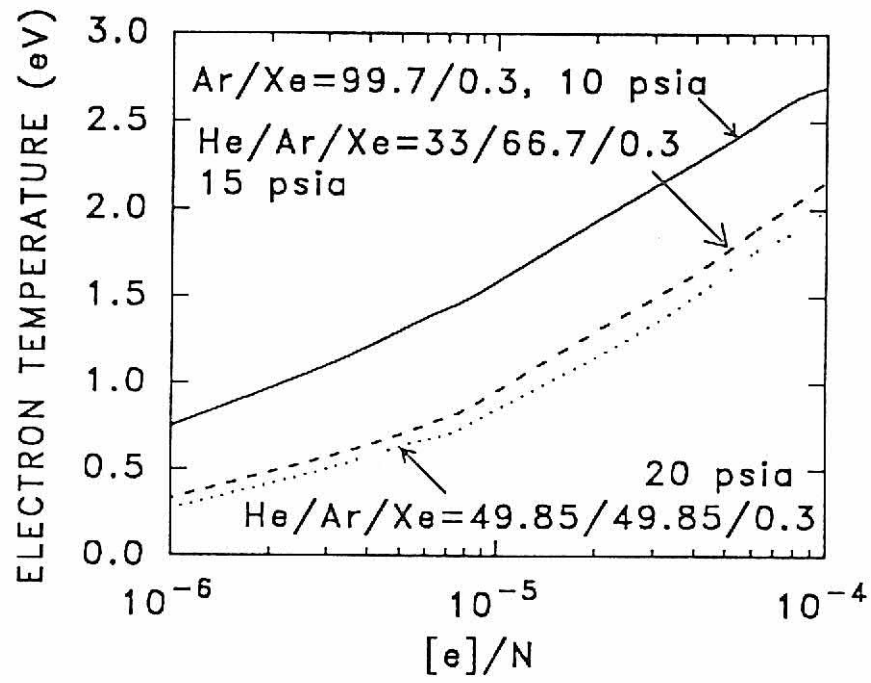


Fig. 3.2. Predicted electron temperature as a function of fractional ionization ($[e]/N$) for Ar/Xe and He/Ar/Xe gas mixtures. As the electron density increases, removal of low energy electrons by recombination effectively heats the distribution.

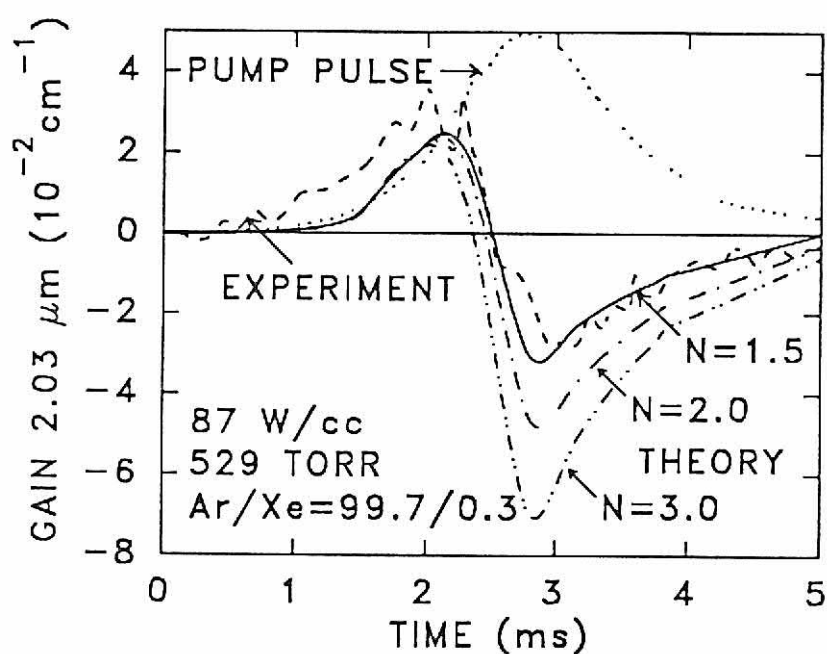


Fig. 3.3. Predictions for gain using different temperature dependencies for the rate coefficient for three-body ion association reactions. The experimental conditions are Ar/Xe = 99.7/0.3, 529 Torr, peak pump power 87 W cm⁻³. The rate coefficient scales as T^{-N} , and three trials are shown: $N = 1.5, 2.0$ and 3.0 . Agreement with experiment is obtained for $N \approx 1.5$.

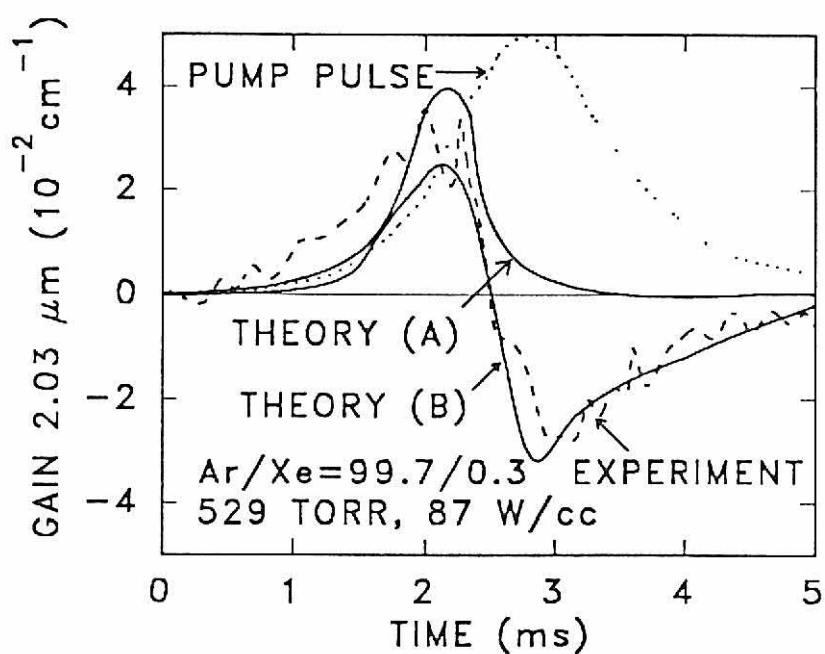


Fig. 3.4. Predictions for gain using different branchings for products of the quenching of Xe($6p$). The conditions are the same as in Fig. 3.3. Theory A has branchings of the quenching to the Xe($6s$) manifold. Theory B has branchings which are retained in the Xe($6p$) manifold.

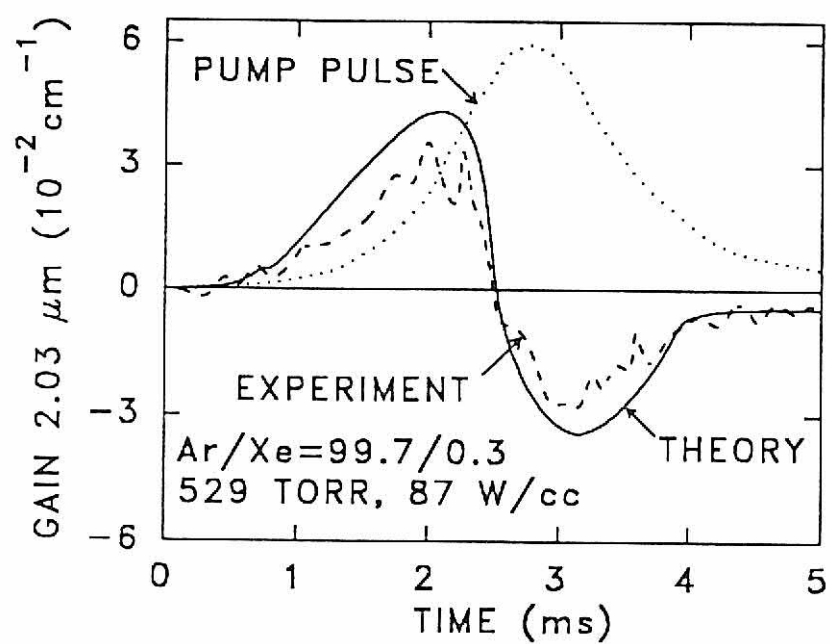


Fig. 3.5. Predicted and experimental gain, and pump power as a function of time for the 2.03 μm transition. The conditions are Ar/Xe = 99.7/0.3, peak pump power 87 W cm⁻³ and 529 Torr.

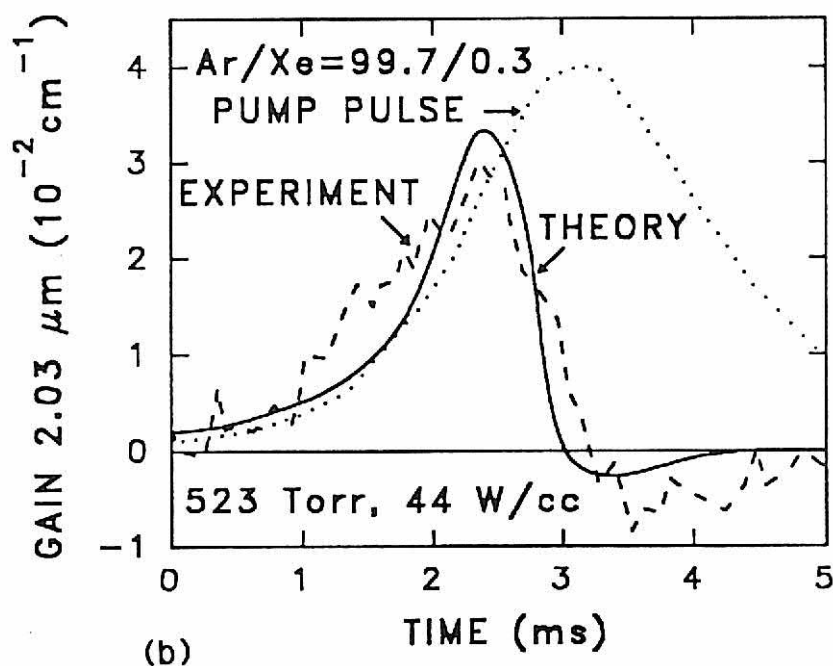
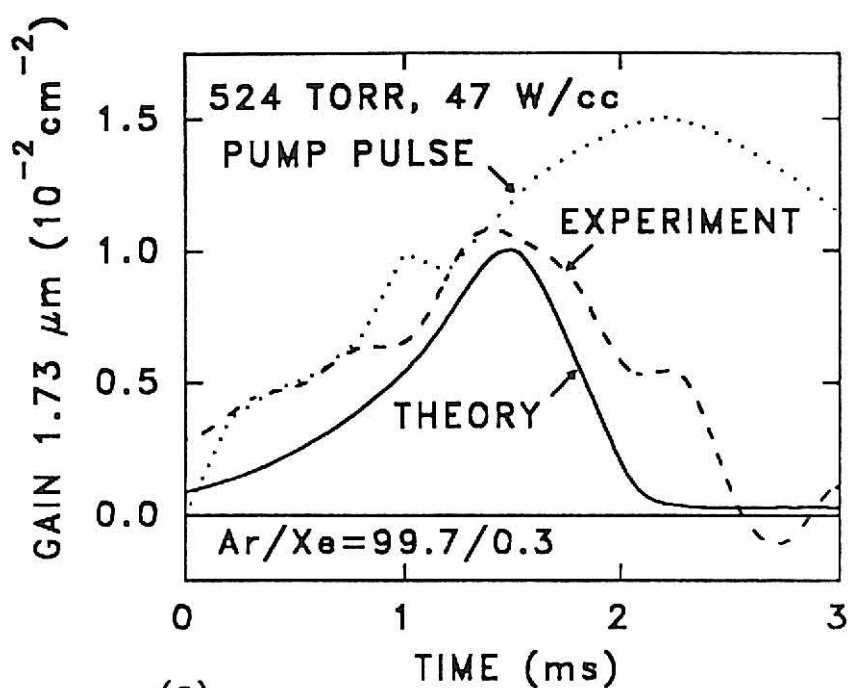


Fig. 3.6. Predicted and experimental gain, and pump power as a function of time for the 1.73 and 2.03 μm transitions in $\text{Ar/Xe} = 99.7/0.3$. The conditions are (a) 1.73 μm , 47 W cm^{-3} , 524 Torr; (b) 2.03 μm , 44 W cm^{-3} , 523 Torr. Gain at 1.73 μm is 0.3-0.5 that at 2.03 μm .

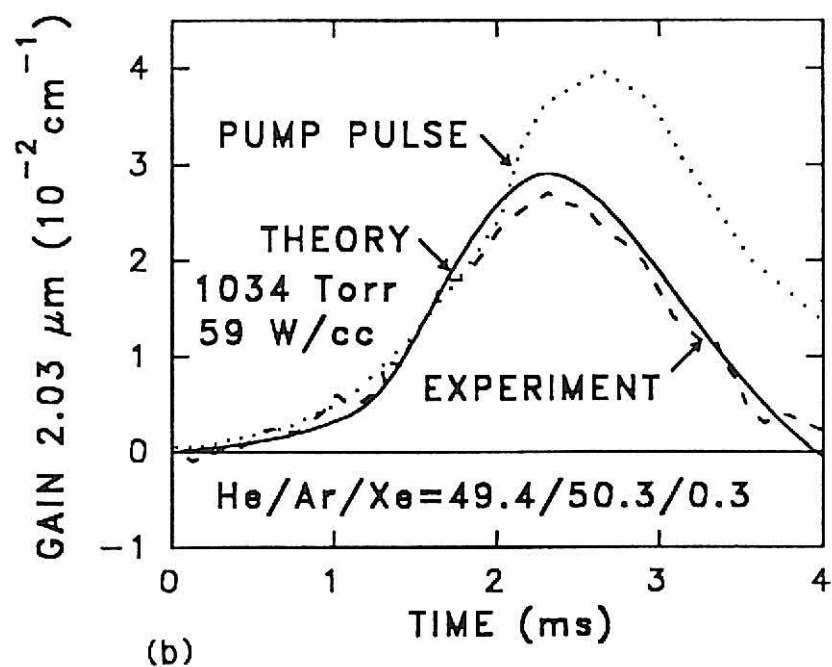
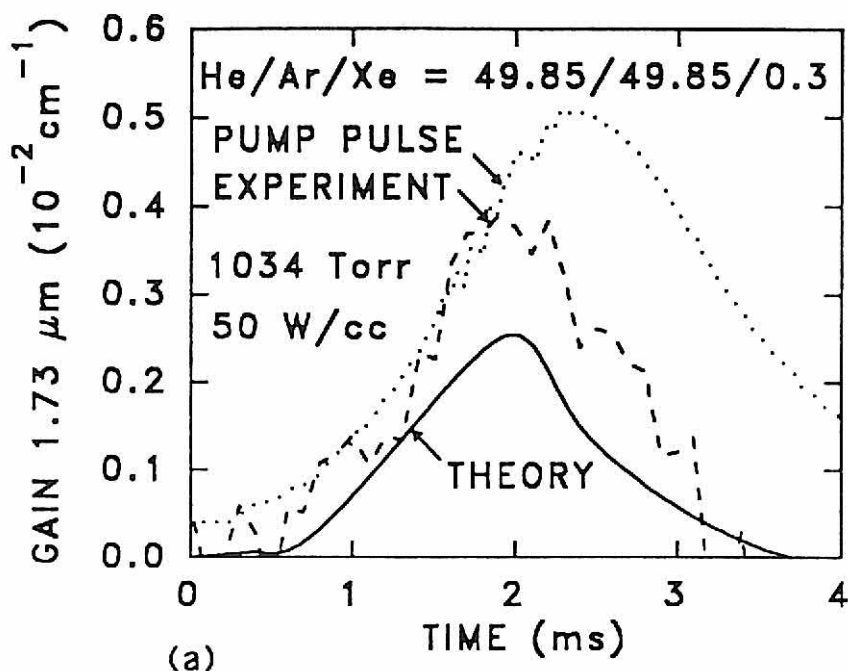


Fig. 3.7. Predicted and experimental gain, and pump power as a function of time for the 1.73 and 2.03 μm transitions. The conditions are (a) 1.73 μm , He/Ar/Xe = 49.85/49.85/0.3, pump power 50 W cm^{-3} and 1034 Torr, (b) 2.03 μm , He/Ar/Xe = 49.4/50.3/0.3, pump power 59 W cm^{-3} and 1034 Torr. The lower specific energy deposition allows gain to extend to longer times.

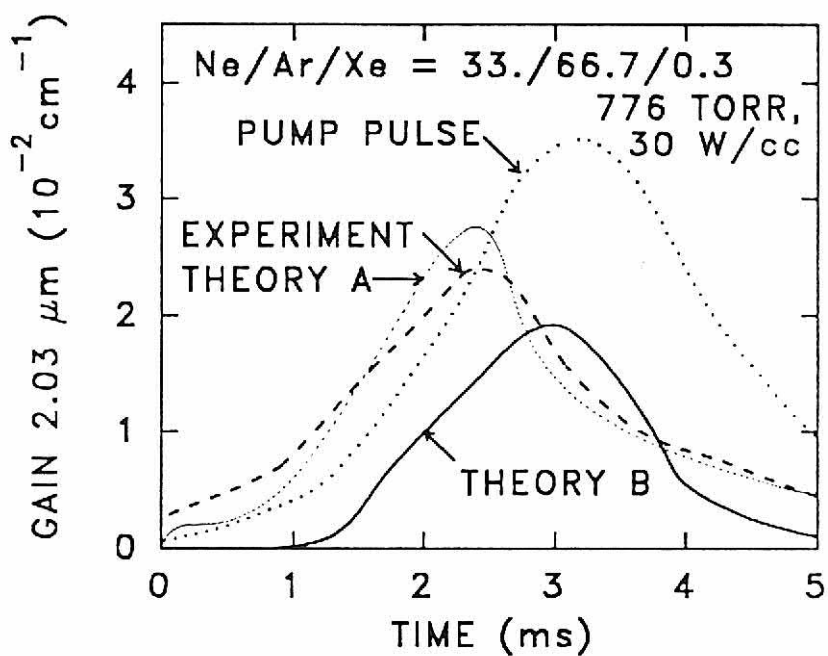


Fig. 3.8. Predicted and experimental gain, and pump power as a function of time for the 2.03 μm transition. The conditions are Ne/Ar/Xe = 33/66.7/0.3, pump power 30 W cm^{-3} and 776 Torr. Two theoretical curves are shown. Curve A uses a rate coefficient for Penning ionization of Xe by Ne excited states of $2 \times 10^{-10} \text{ cm}^3 \text{ s}^{-1}$. Curve B uses a rate coefficient of $1 \times 10^{-11} \text{ cm}^3 \text{ s}^{-1}$.

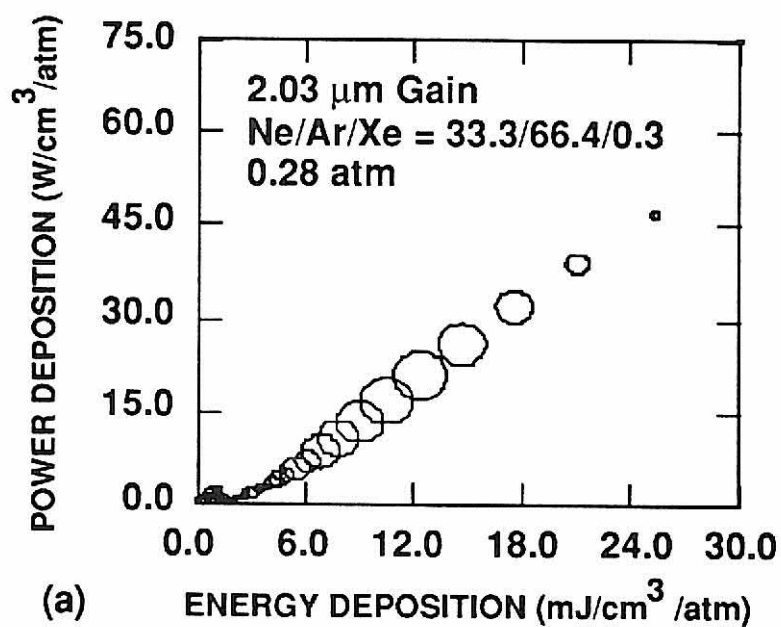
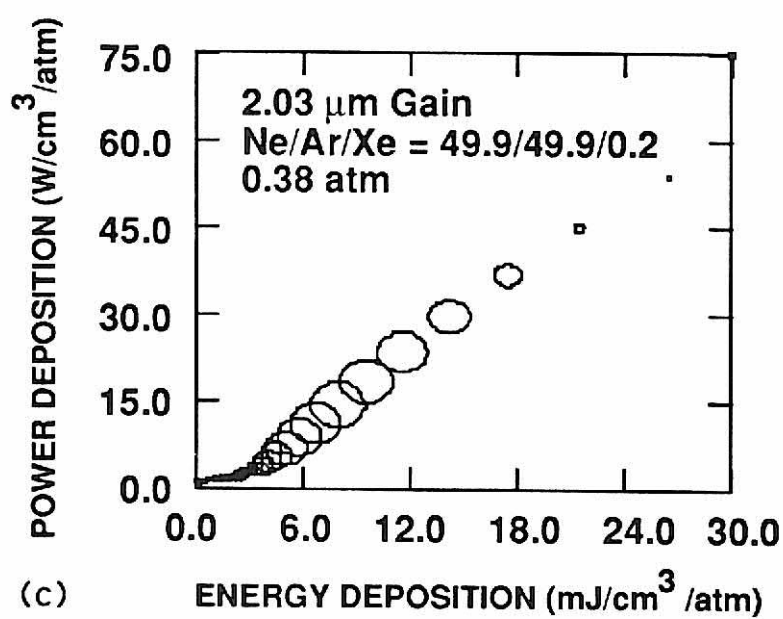
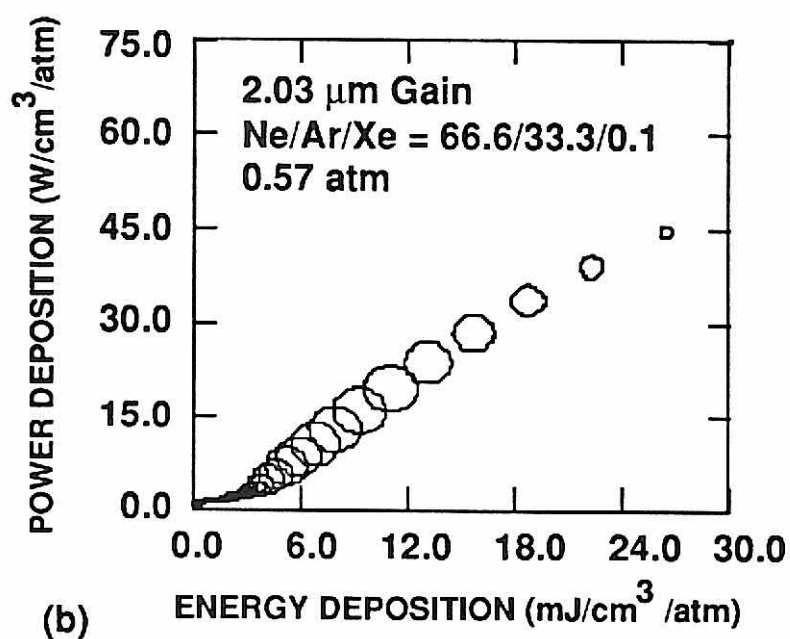


Fig. 3.9. Experimental gain ($2.03 \mu\text{m}$ transition) plotted in terms of power and energy deposition. Size of the circles represents the relative magnitude in gain: (a) Ne/Ar/Xe = 33.3/66.4/0.3%, 0.286 atm, $39 \text{ W}/\text{cm}^3$, (b) Ne/Ar/Xe = 74.4/24.5/0.1%, 0.572 atm, $46 \text{ W}/\text{cm}^3$, (c) Ne/Ar/Xe = 66.5/33.3/0.2%, 0.381 atm, $43 \text{ W}/\text{cm}^3$.



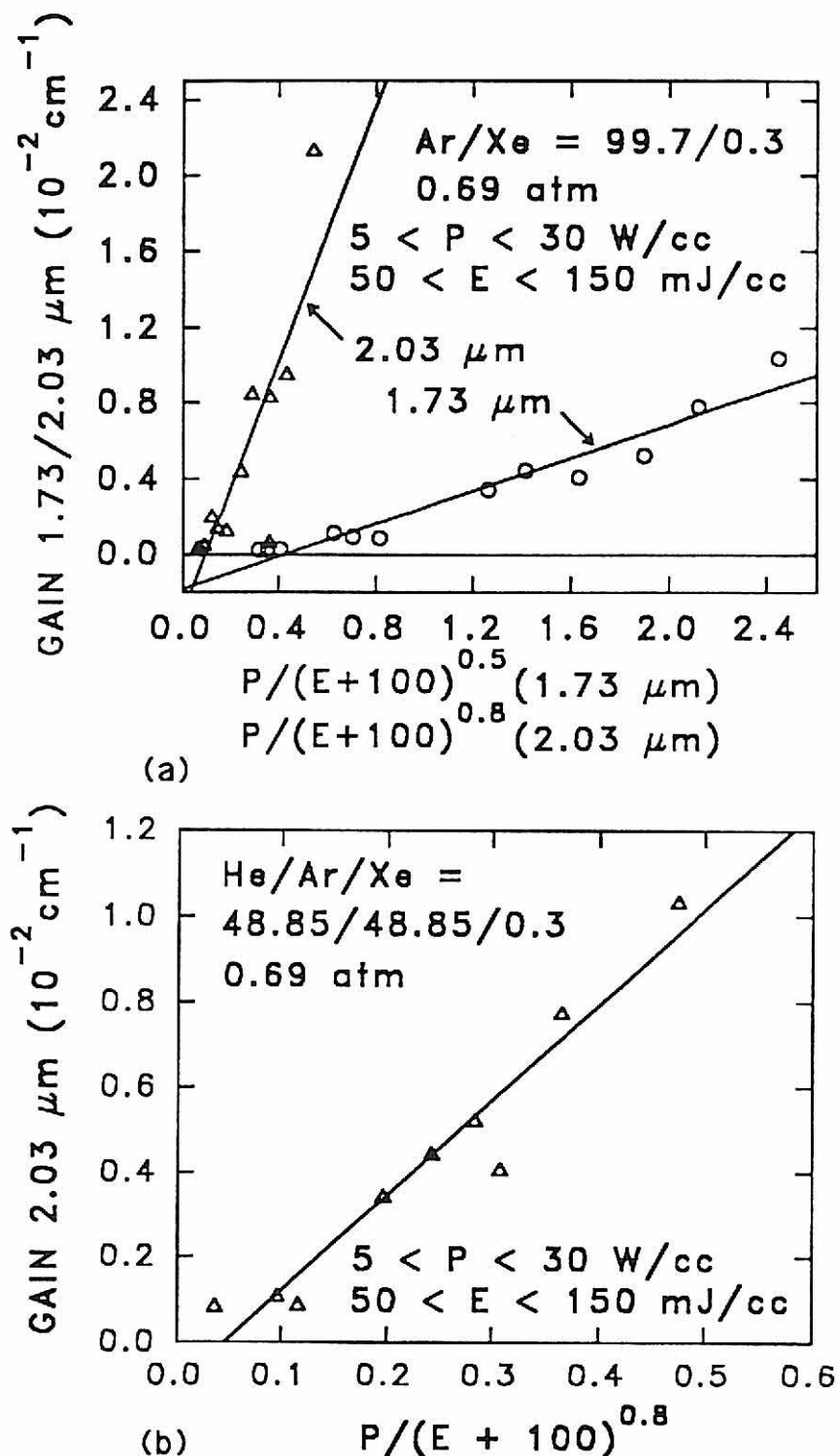


FIG 3.10. Results from computer experiments for gain over a range of power deposition [$5 \leq P(\text{W/cm}^3) \leq 30$] and energy deposition [$50 \leq E(\text{mJ/cm}^3) \leq 150$]. (a) 1.73 and 2.03 μm transitions for Ar/Xe mixtures. (b) 2.03 μm transition for He/Ar/Xe mixtures. Gain scalings of the form $g_0 \approx P/(E+b)^c$ are suggested. The symbols are for trials performed at different combinations of P and E .

3.7 References

- ¹ S. A. Lawton, J. B. Richards, L. A. Newman, L. Specht, and T. A. DeTemple, *J. Appl. Phys.* **50**, 3888 (1979).
- ² N. G. Basov, V. A. Danilychev, A. Yu. Dudin, D. A. Zayarnyl, N. N. Ustinovsky, I. V. Kholin, and A. Y. Chugunov, *Sov. J. Quantum Electron.* **14**, 1158 (1984).
- ³ N. G. Basov, V. V. Baranov, A. Y. Chugunov, V. A. Danilychev, A. Yu. Dudin, I. V. Kholin, N. N. Ustinovsky, and D. A. Zayarnyi, *IEEE J. Quantum Electron.* **QE-21**, 1756 (1985).
- ⁴ A. Suda, B. Wexler, B. Feldman, and K. Riley, *Appl. Phys. Lett.* **54**, 1305 (1989).
- ⁵ A. Suda, B. L. Wexler, K. J. Riley and B. J. Feldman, *IEEE J. Quantum Electron.* **QE-26**, 911 (1990).
- ⁶ A. Suda, B. L. Wexler, K. J. Riley and B. J. Feldman, *IEEE J. Quantum Electron.* **QE-26**, 1304 (1990).
- ⁷ K. Komatsu, E. Matsui, F. Kannari, and M. Obara, *IEEE J. Quantum Electron.* **QE-27**, 90 (1991).
- ⁸ C. L. Gordon III, B. Feldman and C. P. Christensen, *Opt. Lett.* **13**, 114 (1988).
- ⁹ W. J. Alford and G. N. Hays, *J. Appl. Phys.* **65**, 3760 (1989).
- ¹⁰ E. L. Patterson, G. E. Samlin, P. J. Brannon, and M. J. Hurst, *IEEE J. Quantum Electron.* **QE-26**, 1661 (1990).
- ¹¹ W. J. Alford, G. N. Hays, M. Ohwa, and M. J. Kushner, *J. Appl. Phys.* **69**, 1843 (1990).
- ¹² M. Ohwa, T. J. Moratz, and M. J. Kushner, *J. Appl. Phys.* **66**, 5131 (1989).
- ¹³ M. Ohwa and M. J. Kushner, *IEEE J. Quantum Electron.* **26**, 1639 (1990).
- ¹⁴ G. A. Hebner and G. N. Hays, 43rd Gaseous Electronics Conference, Urbana, IL, October 1990, paper QB-1.
- ¹⁵ G. A. Hebner and G. N. Hays, in *Conference on Lasers and Electro-Optics* (Optical Society of America, Washington, DC, (1991), p. 516.
- ¹⁶ M. J. Kushner, *J. Appl. Phys.* **66**, 2297 (1989).
- ¹⁷ T. J. Moratz T. D. Saunders, and M. J. Kushner, *J. Appl. Phys.* **64**, 3799 (1988).
- ¹⁸ J. Torczynski, Sandia National Laboratories, 1990 (unpublished).
- ¹⁹ G. A. Hebner and G. N. Hays, *Appl. Phys. Lett.* **59**, 537 (1991).
- ²⁰ G. A. Hebner and G. N. Hays, *Appl. Phys. Lett.* **57**, 2175 (1990).
- ²¹ G. A. Hebner and G. N. Hays, *J. Appl. Phys.* **71**, 1610 (1992).

- ²² G. Hebner and G. N. Hays (to be published).
- ²³ R. Vetter and D. Reymann, *J. Phys. B* **7**, 323 (1974).
- ²⁴ J. Nella, S. Y. Szeto, P. Rabinowitz and J. T. Latourrette, *IEEE J. Quantum Electron.* **QE-12**, 543 (1976).
- ²⁵ A. M. Voinov, L. E. Dovbysh, V. N. Krivonosov, S. P. Mel'nikov, I. V. Podmoshenskii, and A. A. Sinyanskii, *Sov. Tech. Phys. Lett.* **7**, 437 (1981).
- ²⁶ A. M. Voinov, L. E. Dovbysh, V. N. Krivonosov, S. P. Mel'nikov, I. V. Podmoshenskii, and A. A. Sinyanskii, *Sov. Phys. Dokl.* **24**, 189 (1979).
- ²⁷ D. R. Neal, J. R. Torczynski, W. J. Alford, R. B. Michie and D. E. Bodette, in *Conference on Lasers and Electro-optics* (Optical Society of America, DC, 1991), pp. 244-245.
- ²⁸ R. Johnsen, *J. Chem. Phys.* **85**, 3869 (1986).
- ²⁹ J. Xu and D. W. Setser, *J. Chem. Phys.* **92**, 4191 (1990).
- ³⁰ J. Xu and D. W. Setser, *J. Chem. Phys.* **94**, 4243 (1991).
- ³¹ W. J. Alford, *IEEE J. Quantum Electron.* **QE-26**, 1633 (1990).

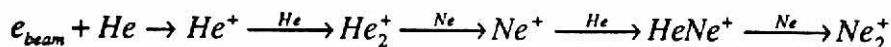
4. SHORT PURSE ELECTRON BEAM EXCITATION OF THE HIGH PRESSURE ATOMIC Ne LASER

4.1 Introduction

The high pressure atomic neon laser operates on four transitions between the $3p$ and $3s$ manifolds (585.3, 659.9, 703.2 and 724.5 nm).¹⁻¹⁸ In particular, the $3p'[1/2]_0 \rightarrow 3s'[1/2]_1$ transition at 585 nm has attracted considerable attention in recent years as a source of efficient quasi-continuous optical power using electron beam,^{2-7,10,14,15} electric discharge,^{1,8,11,12,16,17} microwave,⁹ and fission-fragment¹³ excitation.

Oscillation at 585 nm was first obtained by Bridges and Chester in 1965.¹⁸ Little further work was reported until 1981 when Schmieder et al.¹ investigated electric discharge excitation at 0.7 atm using a $\text{Ne}/\text{H}_2 = 1/(0.6-1.5)$ gas mixture. They proposed that laser oscillation is made possible by quenching of the lower laser level by a Penning reaction of $\text{Ne}(3s)$ with H_2 . In studies by Aleksandrov et al.,⁵ Basov et al.,³ and Bunkin et al.,⁴ the 585 nm transition was pumped in multiatmosphere $\text{He}/\text{Ne}/(\text{Ar}, \text{Kr})$ gas mixtures using low power electron beams (tens of to hundreds of $\text{W}\cdot\text{cm}^{-3}$). They obtained laser efficiencies of 1%-1.6%. Those works, and subsequent modeling studies,^{10, 15} proposed that the upper laser level is populated by dissociative recombination of Ne_2^+ , and that the lower laser level is depopulated by Penning ionization of the lower ionization gas additive (Ar or Kr). Aleksandrov et al.⁵ estimated that nearly 40% of Ne_2^+ recombinations directly populate $\text{Ne}(3p'[1/2]_0)$ at high pressure (> 1 atm) due to a rapid collisional relaxation of the dimer ion to its lowest vibrational state. This allows for selective population of the upper laser level by restricting the energetically permitted exit channels.

Using e-beam excitation, Basov et al.³ obtained high efficiencies in, for example, $\text{He}/\text{Ne}/\text{Ar} = 50/5/1$ gas mixtures at 1-3 atm and 70 W cm^{-3} . They suggested that a possible reaction sequence leading to population of the laser level and relaxation of the lower level is²





Operating with Ne fractions higher than the optimum results in self-quenching of the laser levels by forming neon dimers from $\text{Ne}(3p)$ or directly quenching $\text{Ne}(3p) \rightarrow \text{Ne}(3s)$. Operating with Ar fractions higher than the optimum results in intercepting the formation of Ne_2^+ by charge exchange reactions of Ar with He_2^+ . The dissociative recombination of Ne_2^+ which excites the upper laser level can also be intercepted by charge exchange to Ar. Basov et al.⁵ found that operating at higher power depositions, at least on a quasi-continuous basis, decreased and terminated laser oscillation. This was presumably due to electron collision quenching of $\text{Ne}(3p)$ and collisional radiative recombination of He_2^+ .

Part of the appeal of the Ne laser for low power electron beam and fission fragment excitation is the fact that the upper laser level is probably populated by dissociative recombination of Ne_2^+ . This process has a rate coefficient which increases with decreasing electron temperature ($k \sim T_e^{-1/2}$). These excitation sources typically have lower electron temperatures (0.5-1 eV) compared to, for example, high power discharge excited lasers. Particle beam excitation at low-power deposition produces a lower electron temperature than that produced during high power excitation. This is a result of recombination heating, which occurs at high plasma densities.¹⁹ Electron collision quenching of the laser levels is also minimized at low power deposition. The moderate stopping power of He/Ne/Ar mixtures makes them particularly attractive for fission fragment excitation since high gas pressures may be used.

To investigate the sensitivity of laser oscillation to electron temperature and electron collision quenching, the Ne 585 nm high pressure laser was experimentally investigated using short pulse e -beam excitation, and was theoretically investigated using a computer model. We found that laser oscillation occurred only after a delay following the termination of the e -beam current pulse. This delay is inversely proportional to the amount of added He in a He/Ne/Ar mixture. Results from our computer model showed that the onset of lasing correlated with a

decrease in electron temperature which occurred when the excited state manifolds of Ar were depleted. The decrease in T_e increased the rate of dissociative recombination and pumping of the upper level.

In Section 4.2, the experimental apparatus will be briefly described. The model will be described in Section 4.3, followed by a discussion of our results in Section 4.4. Our concluding remarks are in Section 4.5.

4.2 Description of the Experiment

The Ne laser using He/Ne/Ar mixtures was excited using a short pulse e -beam. The experimental apparatus was a coaxial diode electron beam (Febetron 706).²⁰ The anode consisted of a 20 cm x 0.6 cm (diameter) aluminum tube etched to a thickness of ≈ 130 μm . The anode also served as the pressure vessel between the laser gas mixture and the vacuum diode region, and thus defined the plasma excitation region. The Febetron 706 is capable of delivering about 12 J of energy in a 600 kV pulse with a duration of 3 ns (FWHM) into a matched load. Since the diode is somewhat mismatched to the pulse forming network, the e -beam pulse is somewhat lengthened (4-5 ns), but is short compared to other time scales.

The distance between the mirrors of the laser cavity was 42 cm and the mirror reflectivities were 0.95 and 0.98. The experiments reported here were performed using He/Ne/Ar gas mixtures at 1-4 atm total pressure. The power deposition was estimated at 40 MW cm^{-3} at 3.72 atm. Laser power was measured with a Hamamatsu R1193U-03 biplanar photodiode. All data were collected using a digital oscilloscope (Hewlett Packard 54111D).

4.3 Description of the Model

The Ne laser model consists of a full accounting of the electron and heavy particle kinetics of He/Ne/Ar mixtures. It is conceptually similar to previous models of excimer lasers²¹ and of the xenon laser previously discussed by the authors.²² The model differs from previously

published models of the Ne laser by Aleksandrov et al.¹⁵ and Derzhiev et al.¹⁰ by including additional species to resolve intramanifold kinetics, and in details of our kinetic mechanisms.

In our model we include 33 ground state, excited and ionic species, which encompass all levels of the Ne($3p$), Ne($3p'$), Ne($3s'$) and Ne($3s$) manifolds. In this manner, all four laser transitions can be resolved. Approximately 450 individual collisional and radiative processes are included in the model. A complete listing of the reactions and rate coefficients used in the model is in Appendix B. The W values for the e -beam excitation were computed using a separate Monte Carlo simulation for e -beam slowing for the particular gas mixtures of interest.¹⁹ The results of the Monte Carlo simulation are also used to determine the stopping power of the gas mixture and to properly scale the power deposition as the gas mixture is changed.

In the kinetics model, energy conservation equations for both heavy and light particles are used to resolve the gas and electron temperatures. The energy balance equations for the electron temperature are essentially the same as those used by Kannari et al.²¹ in which all pertinent elastic, inelastic and superelastic collisions contribute to the electron power balance, as well as energetic contributions from the slowing of beam electrons. We found that even though excited states of Ar do not directly play an important role in the excitation and relaxation kinetics of the laser levels, they are important to the electron energy balance. Therefore, a five-level model is used for the argon excited state manifolds and is coupled into the electron temperature kinetics.

Although the immediate excitation mechanism for the upper laser level is thought to be understood (dissociative recombination of Ne_2^+), the branching ratios to the upper laser and other levels, as well as the rates of quenching of those levels are not well-known. (The major kinetic pathways are illustrated in Fig. 4.1.) We used parameteric experimental data for threshold lasing and spontaneous emission from Ne($3p'[1/2]_0$) as a function of gas pressure and mixture to derive kinetically consistent values for many of these branching ratios. For example, laser oscillation occurs only after a delay of 10s to 100s ns following the current pulse, and decreases with increasing He fraction. Branching ratios for dimer recombination to individual

Ne($3p'$) levels were obtained by comparing the predicted time to threshold with experiments for a series of gas mixtures. Although these branching ratios depend somewhat on our reaction scheme and are therefore not unique, we believe that they capture the essential physics.

The direct contribution of energetic beam electrons to excitation of the upper laser level was obtained by comparing the model results to spontaneous emission from Ne($3p'[1/2]_0$). We determined that the direct and cascade contribution to Ne($3p'[1/2]_0$) during the e -beam pulse is small, even when including the effects of electron collision quenching. (See Section 4.4.) The fractional contribution resulting from direct e -beam excitation for the upper laser level, as represented by the W value for excitation during the current pulse, was determined to be less than 5%.

Although the stopping power of He is low in electron beam excitation, He⁺ can be produced in large proportions when He is the dominant gas component. For example, in a He/Ne/Ar = 75/15/10 mixture, approximately 30% of the e -beam power is directly dissipated by ionization of He. Helium ion, however, rapidly undergoes charge transfer reactions to He₂⁺ and to Ne⁺, the latter process occurring with a rate coefficient of $1.4 \times 10^{-10} \text{ cm}^3 \text{ s}^{-1}$.²³ Helium ion is therefore not directly important to the reaction scheme. As the density of Ne⁺ increases during the afterglow of the e -beam current pulse, the dimer Ne₂⁺ is formed in large quantities through three body association reactions with both Ne⁺ and two-body reactions with HeNe⁺. The rate constants for the three-body association reactions we used are $4.4 \times 10^{-32} \text{ cm}^6 \text{ s}^{-1}$ for stabilization by Ne and $3.0 \times 10^{-31} \text{ cm}^6 \text{ s}^{-1}$ for stabilization by He.^{24,25} Dissociative recombination of Ne₂⁺ and subsequent excitation of the upper laser level proceeds with a rate coefficient of $3.7 \times 10^{-8} T_e^{-0.43} \text{ cm}^3 \text{ s}^{-1}$ where T_e is the electron temperature in electron volts.²⁶ The branching ratios for dissociative recombination of Ne₂⁺ to the laser levels, derived in the manner described above are: 40% for Ne ($3p'[1/2]_0$), 13.8% for Ne ($3p'[1/2]_1$) and 10% for Ne ($3s'[1/2]_1$).

Neon dimer ion, Ne₂⁺, will also charge exchange to Ar⁺ and Ar₂⁺ by two-body ($k=3.0 \times 10^{-11} \text{ cm}^3 \text{ s}^{-1}$) and three-body processes ($k = 3.5 \times 10^{-30} \text{ cm}^6 \text{ s}^{-1}$).²⁶ Therefore,

formation of upper laser level by dissociative recombination competes with charge transfer and dissociative recombination to Ar. When the fraction of Ar increases so that $[Ar]/[e]$ exceeds $\approx 2 \times 10^3$, the rate of charge transfer reactions from Ne_2^+ to Ar^+ exceeds the rate of dissociative recombination. This, in turn, decreases the gain. The lower laser level is dominantly quenched by Penning ionization of argon and heavy particle quenching. The rate constant we used for Penning ionization of Ar is $1.5 \times 10^{-10} \text{ cm}^3 \text{ s}^{-1}$,⁴ while the rate constant for Ar quenching of the lower laser level $[Ne(3s') + Ar \rightarrow Ne(3s) + Ar]$ was estimated to be $\approx 2.0 \times 10^{-11} \text{ cm}^3 \text{ s}^{-1}$.²⁶

4.4 Neon Laser Characteristics Using Short Pulse *E*-Beam Excitation

Typical traces of the *e*-beam current pulse and laser emission are shown in Fig. 4.2(a). The *e*-beam current pulse is indicated by the x-ray flash recorded by the photodiode, somewhat broadened by detector response. The gas mixture is He/Ne/Ar = 0.7/0.2/0.1 at a total gas pressure of 1.9 atm. Laser oscillation is not observed until $\approx 30 \text{ ns}$ after the termination of the current pulse. This behavior is partly explained by the observations of spontaneous emission shown in Fig. 4.2(b) for He/Ne/Ar mixtures of 0.18/0.55/0.27 and 0.0/0.67/0.33. Little spontaneous emission is observed during the current pulse, suggesting that the upper laser level is not directly excited by the energetic beam electrons, or electron collision quenching during the current pulse is at least as rapid as the excitation. Adding He to the mixture shortens the delay in the spontaneous emission after the current pulse but emission still does not occur during the current pulse. Results from our model for the density of the upper laser level (proportional to spontaneous emission) which reproduce the experiment are shown in Fig. 4.2(c). This behavior suggests that the more rapid cooling of the electrons during the afterglow afforded by the added He increases the rate of dissociative recombination of Ne_2^+ , which directly pumps the upper laser level.

Results from the model show that if there is any significant excitation of the upper laser level during the current pulse there should also be a substantial amount of spontaneous emission relative to the afterglow. Following these arguments, the experimental results imply that direct

excitation of the laser levels during the current pulse is not particularly important. To investigate this issue, we varied the fraction of the direct excitation of neon during the current pulse that is allocated to $\text{Ne}(3p'[1/2]_0)$. For example, predictions are shown in Fig. 4.2(c) for spontaneous emission where 0.25 of direct excitation of neon goes to the upper laser level. This produces an excessive amount of spontaneous emission, relative to that during the afterglow, compared to that observed experimentally.

Experimental laser powers as a function of time for a He/Ne/Ar gas mixture (Ne = 200, Torr, Ar = 50 Torr) are shown in Fig. 4.3(a) and 4.3(b) for different partial pressures of He (500 - 2830 Torr) yielding a total pressure of 1-4 atm. Due to the moderate stopping power of He, the total power deposition changes by only 10% over this range of gas pressures. For example, for He/Ne/Ar = 500/200/50 (Torr), the power deposition is 36.2 MW cm^{-3} ; at He/Ne/Ar = 2830/200/50 (Torr), the power deposition is 40 MW cm^{-3} . As the amount of added helium increases up to 1500 Torr, the delay time to oscillation, as well as the time at which peak laser power is obtained, decreases as shown in Fig. 4.4(a). The maximum laser power increases up to 1100 Torr added helium, decreasing at higher He addition [see Fig. 4.4(b)]. These results suggest that as the helium fraction is increased, the rate of cooling of the electrons increases due to the favorable rate of energy transfer to the light He. Since the rate of dissociative recombination of Ne_2^+ , which pumps the upper laser level, increases with decreasing electron temperature, the upper laser level is being pumped at successively shorter delays with increasing He addition. As He is added to the gas mixture, the laser transition is broadened by collisions with He. Once the minimum delay is reached, this additional broadening with increasing He decreases the gain. For constant output coupling from the cavity, this decreases laser power. Since absorption at the laser wavelength is minimal, some portion of the reduced performance could be recouped by optimizing the cavity parameters to match the lower gain.

Results from our model for laser intensity as a function of gas mixture for the experimental conditions of Fig. 4.3 are shown in Fig. 4.5(a). The predicted delay time to laser oscillation and peak intensity, and the relative peak intensities are shown in Fig. 4.5(b). We also

obtain a decrease in the delay time to threshold with increasing He addition which, with a fixed offset, agrees well with the experiment. The decrease in delay is largely due to the increasing rate of electron cooling with added He, discussed in more detail below.

The contribution of broadening of the laser transition to the decrease in laser power was investigated with the model. Aleksandrov et al.¹⁵ measured the broadening coefficient of the 585 nm transition by collisions with He and obtained $\gamma = 0.62 \times 10^{-9} \text{ cm}^3 \text{ s}^{-1}$. We parameterized this broadening coefficient in the model between 0.5×10^{-10} and $1 \times 10^{-9} \text{ cm}^3 \text{ s}^{-1}$, and the predicted laser powers are shown in Fig. 4.5(c) for He/Ne/Ar = 0.7/0.2/0.1 at 3.6 atm. An increase in broadening does not appreciably change the delay time to threshold, since this value is largely determined by the onset of dissociative recombination resulting from the cooling of the electrons. Once threshold is reached, however, the broadening of the transition increases the saturation intensity. This allows other parasitic processes, such as electron collision quenching, to lower the inversion density and hence laser power.

Predicted electron temperatures as a function of time for gas mixtures containing Ne = 300 Torr and Ar = 150 Torr are shown in Fig. 4.6(a) for various He pressures. During the *e*-beam current pulse the electron temperature reaches a maximum value of $\approx 3 \text{ eV}$. Immediately after the *e*-beam current pulse, the electron temperature cools to a plateau value of 0.5-1.0 eV. The plateau value decreases with increasing He fraction, a consequence of the more rapid rate of electron cooling afforded by more efficient energy exchange collisions with He. This plateau value is sustained for tens to hundreds of nanoseconds, at which time the electron temperature again falls to a value of 0.05-0.2 eV, and continues to slowly thermalize to the gas temperature. The onset of laser oscillation coincides with the fall in electron temperature from its plateau value. This correlation is shown in Fig. 4.6(b) where the time of the onset of laser oscillation and the time at which the electron temperature falls off the plateau are plotted.

The plateau value of the electron temperature is sustained by heating from superelastic electron collisions with excited state manifolds. Since excitation transfer results in a rapid cascade of population from He to Ne, and ultimately to Ar, the majority of the superelastic

collisions which heat the electrons during the plateau period are with excited states of Ar. The correlation between electron temperature and excited state densities is shown in Fig. 4.7(a). Here the densities of excited states of He, Ne and Ar, and the electron temperature are plotted as a function of time for a He/Ne/Ar = 0.7/0.2/0.1 mixture. Selected ion densities for the same conditions are plotted in Fig. 4.7(b). For these conditions, 39% of the *e*-beam energy is deposited in Ar, and 45% of the beam energy is deposited in He. Excitation transfer from He to Ne and Ar, and from Ne to Ar occurs rapidly until the densities of excited states of Ar greatly exceed those of excited states of He and Ne. Argon is also the most plentiful ion. The excited states of Ar therefore dominate the energy exchange with electrons during the afterglow. When excited states of Ar are depleted by superelastic collisions, the source of electron heating is exhausted, and the electron temperature is allowed to decrease. At this time the rate of dissociative recombination increases with the fall of the electron temperature, and excited states of Ne are rapidly populated. The density of Ar_2^+ remains high throughout this period because Penning processes of $\text{Ne}(3s)$ with Ar continue to generate Ar^+ .

It has been proposed that electron collision mixing (ECM) of the laser levels of the atomic xenon ($5d \rightarrow 6p$) laser is a limiting process and restricts operation of the xenon laser to a fractional ionization of $< 10^{-5}$. In experiments performed by Peters et al.,²⁷ a delay in the onset of oscillation of a xenon laser excited by a short pulse *e*-beam was observed. This behavior was attributed to the time that was required for the electron density to decrease below a critical value above which ECM prevented oscillation. We investigated whether ECM is a limiting process in the Ne laser. The electron density at the time at which laser oscillation begins in the Ne laser, as predicted by the model, is plotted in Fig. 4.8(a). The gas mixture is 200 Torr of Ne, 50 Torr of Ar and the noted balance of He. The rate coefficient used for superelastic relaxation of $\text{Ne}(3p'[1/2]_0)$ is $8.8 \times 10^{-9} \text{ cm}^3\text{s}^{-1}$. Endothermic rates are given by detailed balance. There is not a strong correlation between the onset of oscillation and the electron density or fractional ionization. This suggests that ECM is less a factor in the Ne laser (at these excitation levels) compared to the xenon laser. This behavior was confirmed by varying the pump rate in the

model. Laser powers as a function of pump rate are shown in Fig. 4.8(b) for a He/Ne/Ar mixture at 3 atm. The laser power is nearly proportional to the pump rates above threshold. The laser turns on slightly earlier at the lower pump rates due to the smaller amount of ECM. The onset of the laser oscillation, though, is only a weak function of pump power compared to its dependence on He partial pressure.

Quasi-continuous operation of the Ne laser by others has shown that the optimum laser efficiency occurs with a Ne/Ar ratio of approximately 2/1. We parameterized the Ne/Ar ratio in the model. We found that laser power as a function of Ar pressure optimizes at a Ne/Ar ratio of 4/1. Laser oscillation does not occur until an Ar pressure of ≈ 20 Torr. The experimental threshold for laser oscillation is ≈ 15 Torr of Ar. At low Ar pressures, there is not sufficient quenching of the lower laser level. At high Ar pressures, Ne_2^+ is intercepted prior to undergoing dissociative recombination.

4.5 Concluding Remarks

The kinetics of the Ne 585 nm high pressure laser using He/Ne/Ar mixtures have been experimentally and theoretically investigated using short pulse *e*-beam excitation. The experimental results are well-explained by the upper laser level being dominantly excited by dissociative recombination of Ne_2^+ during the afterglow following the current pulse. The onset of laser oscillation occurs when the electron temperature falls to a few tenths of an electron volt, and the rate of dissociative recombination increases. The lower laser level is largely quenched by Penning ionization with Ar. We found that details of the Ar kinetics are important since superelastic heating of the electrons from excited states of Ar maintains the temperature at a sufficiently high value to prevent laser oscillation. During quasi-continuous operation of the Ne laser, a higher electron temperature is compensated by a higher plasma density, which increases the rate of recombination and pumping of the upper laser level.

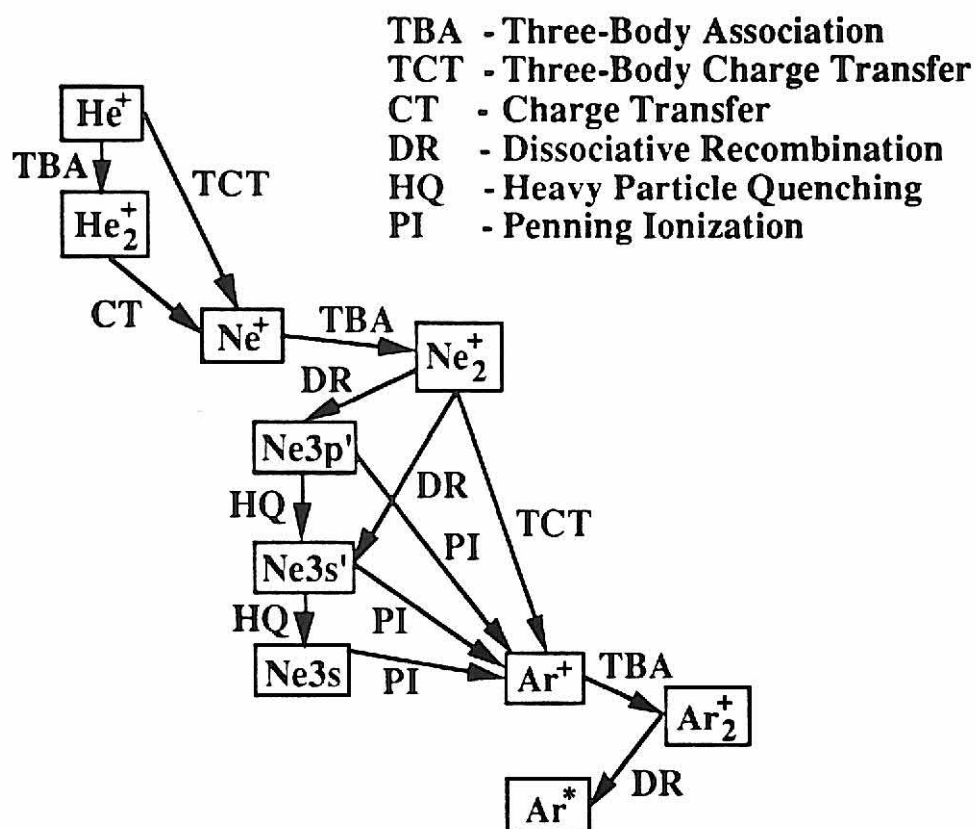


Fig. 4.1. Schematic of the excitation pathways of the high pressure Ne laser. Oscillation at 585 nm occurs between $\text{Ne}(3p'[1/2]_0)$ and $\text{Ne}(2s'[1/2]_1)$. Excitation of the upper laser level occurs dominantly by dissociative recombination of Ne_2^+ . Quenching of the lower laser level is dominantly by Penning ionization of Ar.

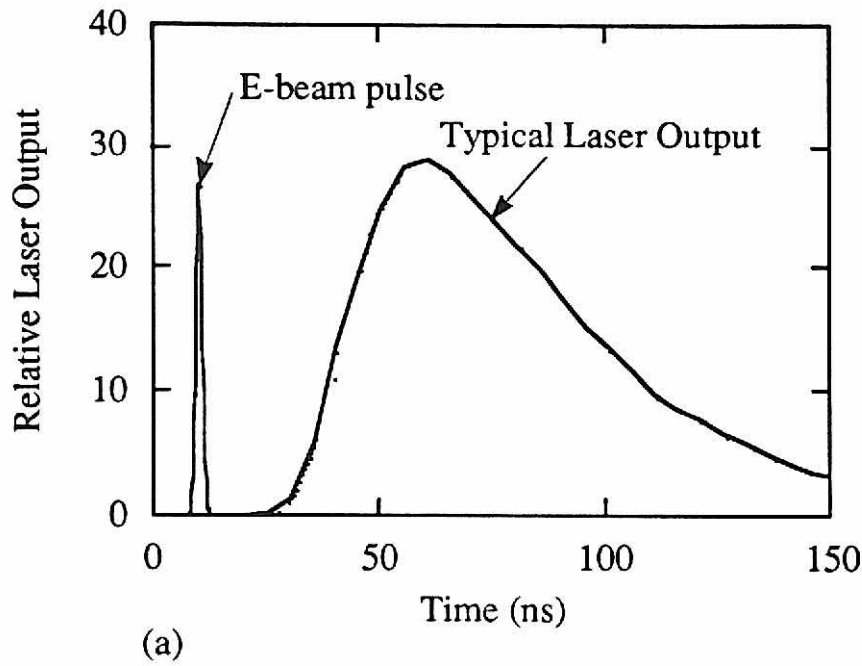
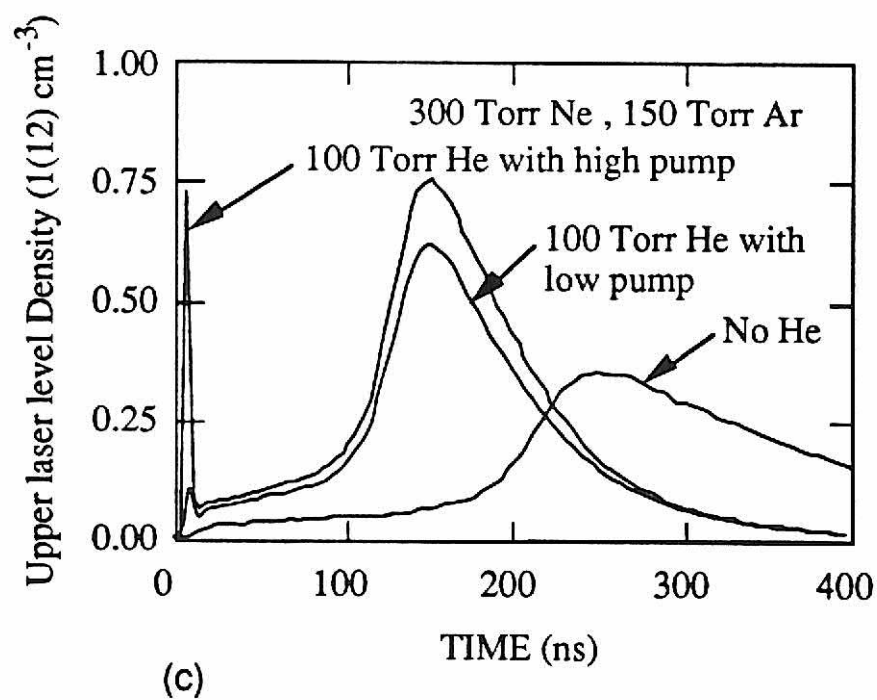
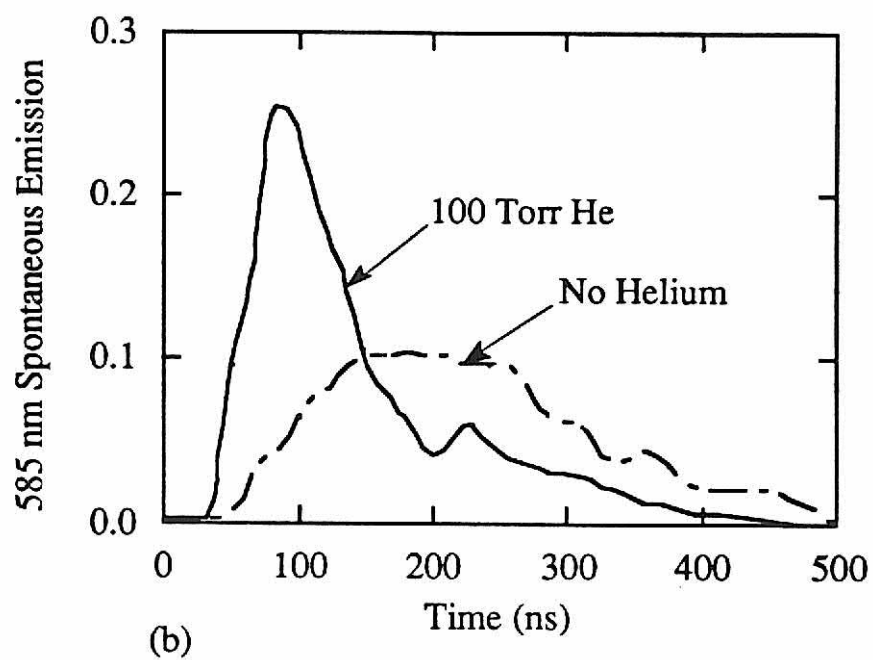


Fig. 4.2. Typical experimental and theoretical results for Ne laser operation. (a) Experimental results for the *e*-beam current pulse and laser oscillation at 585 nm showing the delay between the *e*-beam current pulse and onset of oscillation (He/Ne/Ar = 0.7/0.2/0.1, 1.9 atm). (b) Experimental observations of spontaneous emission at 585 nm when including He (He/Ne/Ar = 0.18/0.55/0.27, 550 Torr) and excluding He (He/Ne/Ar = 0/0.67/0.33, 450 Torr) showing an increase in spontaneous emission with added He. (c) Theoretical results for the density of the laser level (proportional to spontaneous emission) for the experimental conditions. We also show results when a larger proportion of excitation during the *e*-beam pulse is allocated to the upper laser level. The predicted spontaneous emission during the current pulse with the larger allocation is greater than that which is experimentally observed.



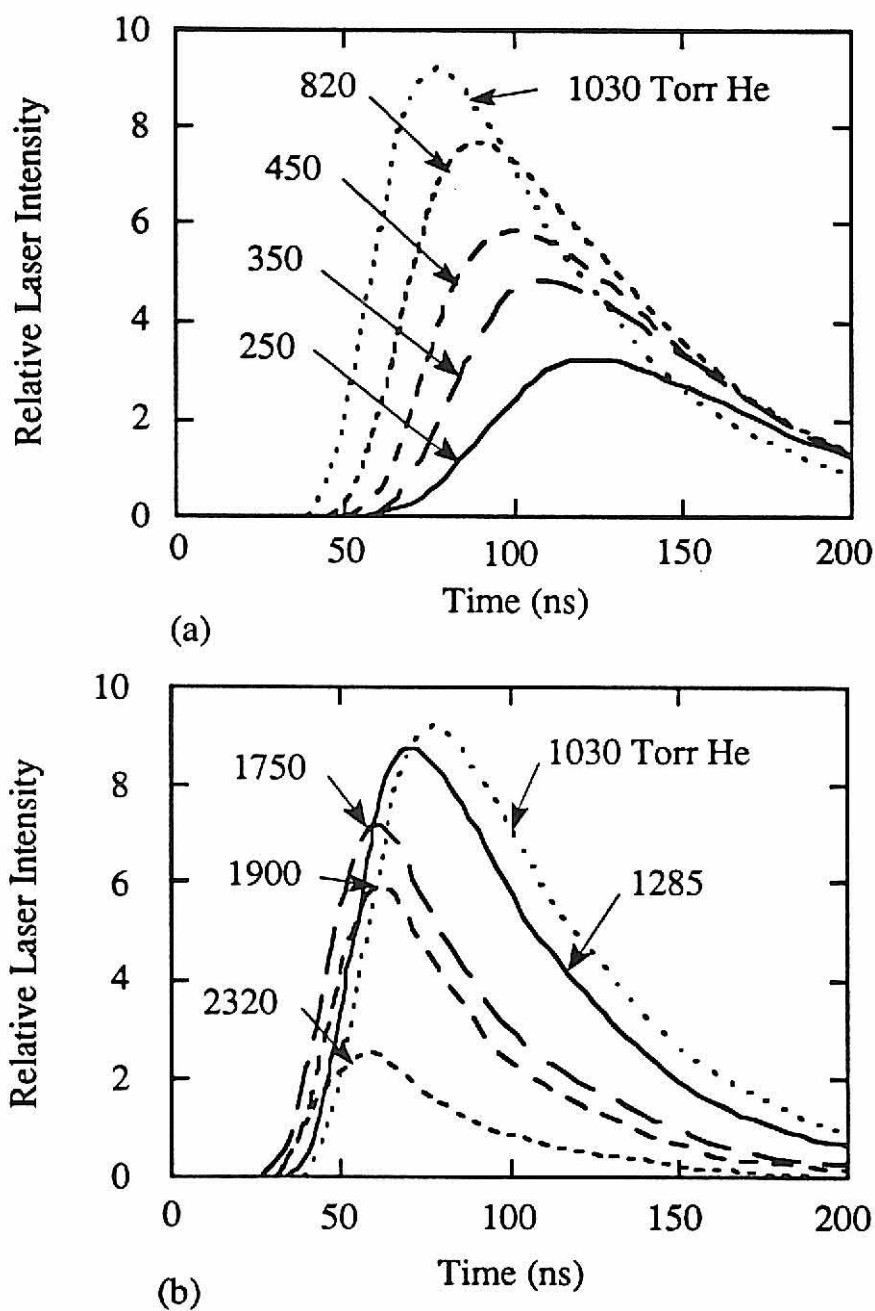
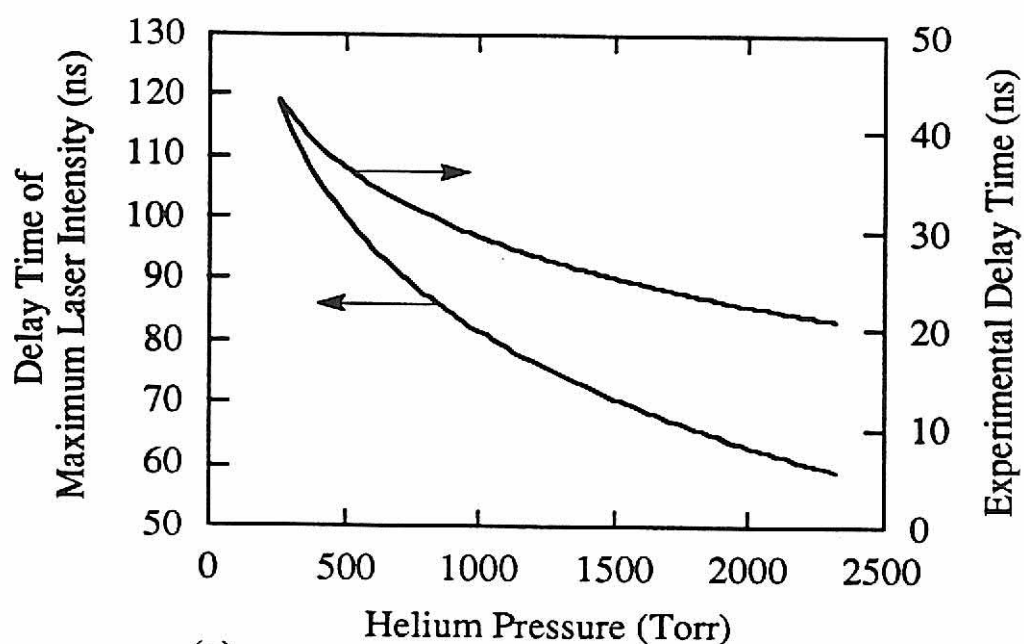
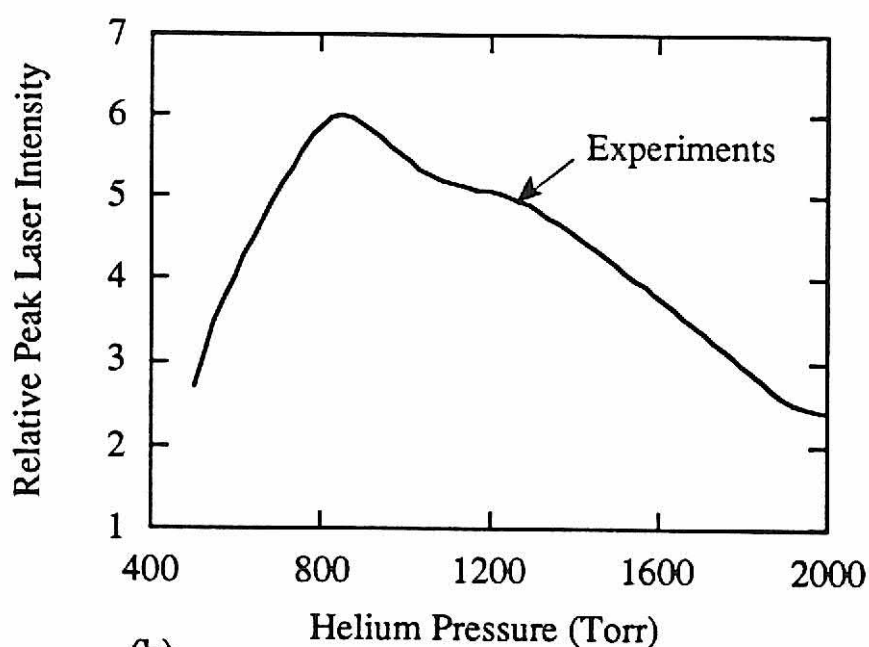


Fig. 4.3. Experimental results for laser intensity as a function of time for various He pressures. (a) 500 Torr - 1000 Torr and (b) 1000 Torr - 1900 Torr. The Ne and Ar pressures are 200 Torr and 50 Torr, respectively. The delay between the current pulse and laser oscillation increases with increasing He pressure because the electron cooling rate increases. The laser intensity decreases at high helium pressure due to broadening of the laser transition.



(a)



(b)

Fig. 4.4. Experimental results for laser parameters as a function of He pressure. (a) The delay between the current pulse, and turn on of the laser and peak intensity. (b) Maximum laser intensity. The conditions are the same as in Fig. 4.3.

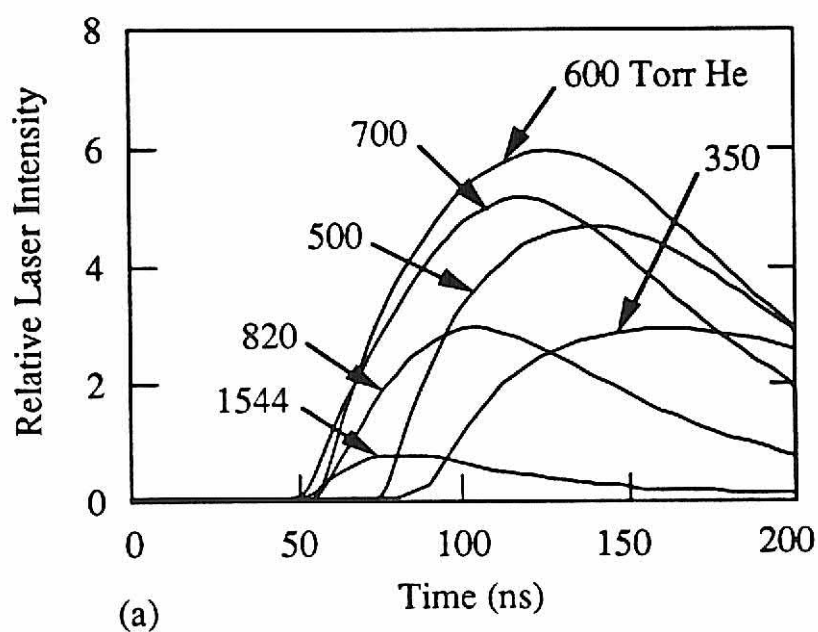
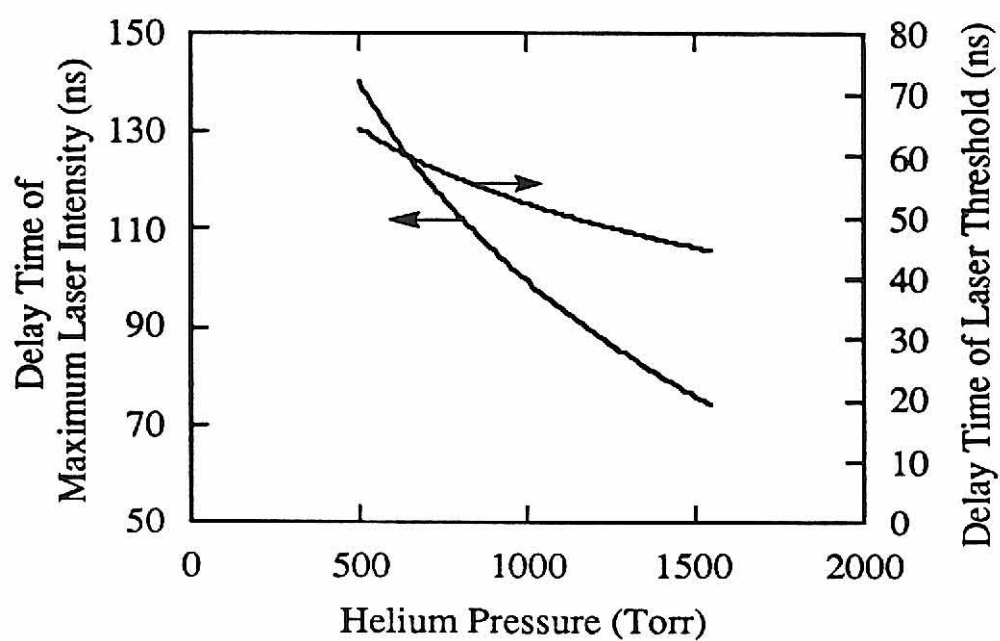
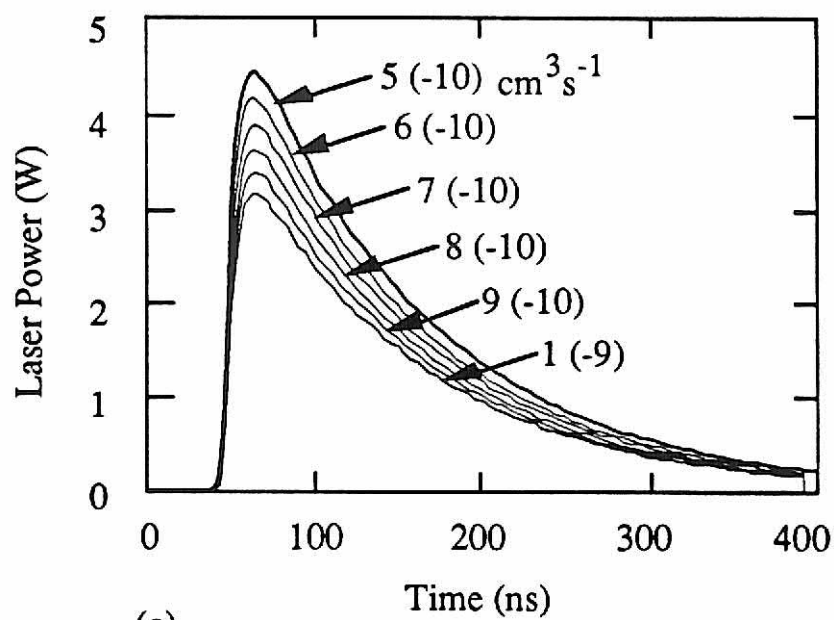


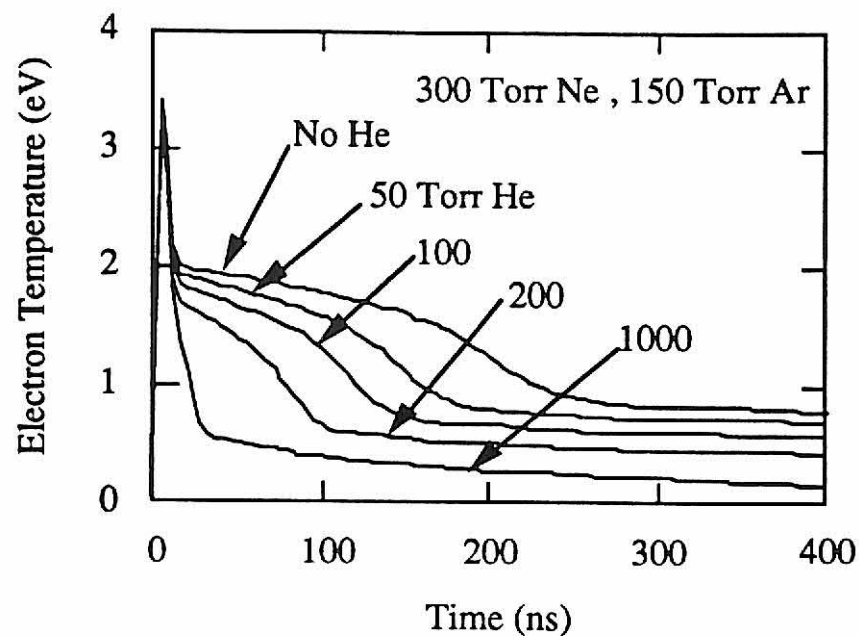
Fig. 4.5. Results from the model for (a) laser intensity as a function of time for various He partial pressures, (b) delay in onset of laser oscillation and peak intensity, and (c) laser intensity as a function of the broadening coefficient for the laser transition. The gas pressure is 3.6 atm while the other conditions are the same as for the experimental results in Fig. 4.3. The decrease in delay time can be attributed to a higher rate of electron thermalization. The decrease in laser intensity can be attributed to broadening.



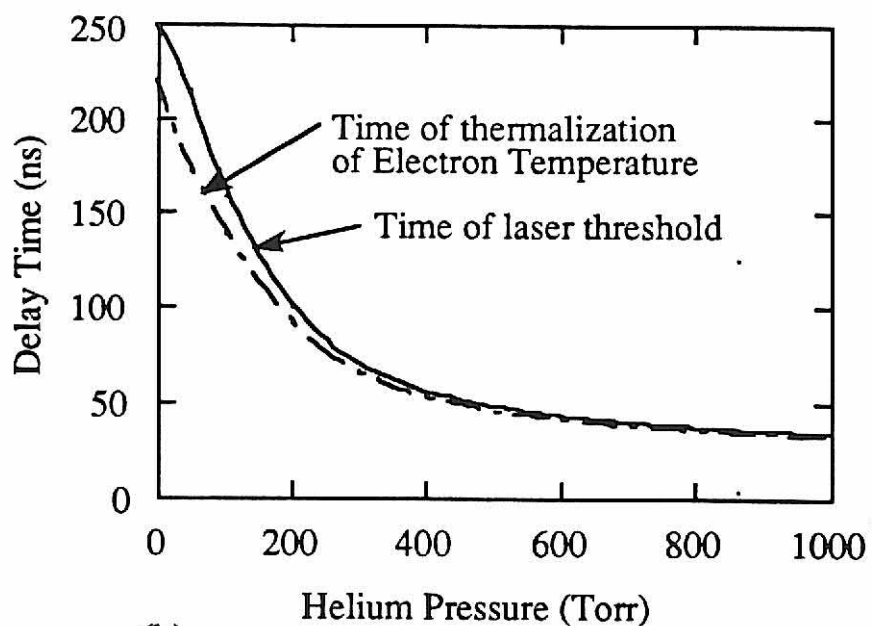
(b)



(c)



(a)



(b)

Fig. 4.6. Predictions from the model for (a) electron temperature as a function of time for various partial pressures of He, and (b) times at which the electron distribution thermalizes and the time at which oscillation starts. The gas mixture is Ne = 300 Torr, Ar = 200 Torr with the indicated amounts of He. The electron temperature quickly falls to a plateau value after the e-beam current pulse. Laser oscillation does not occur until the electron temperature falls off this plateau.

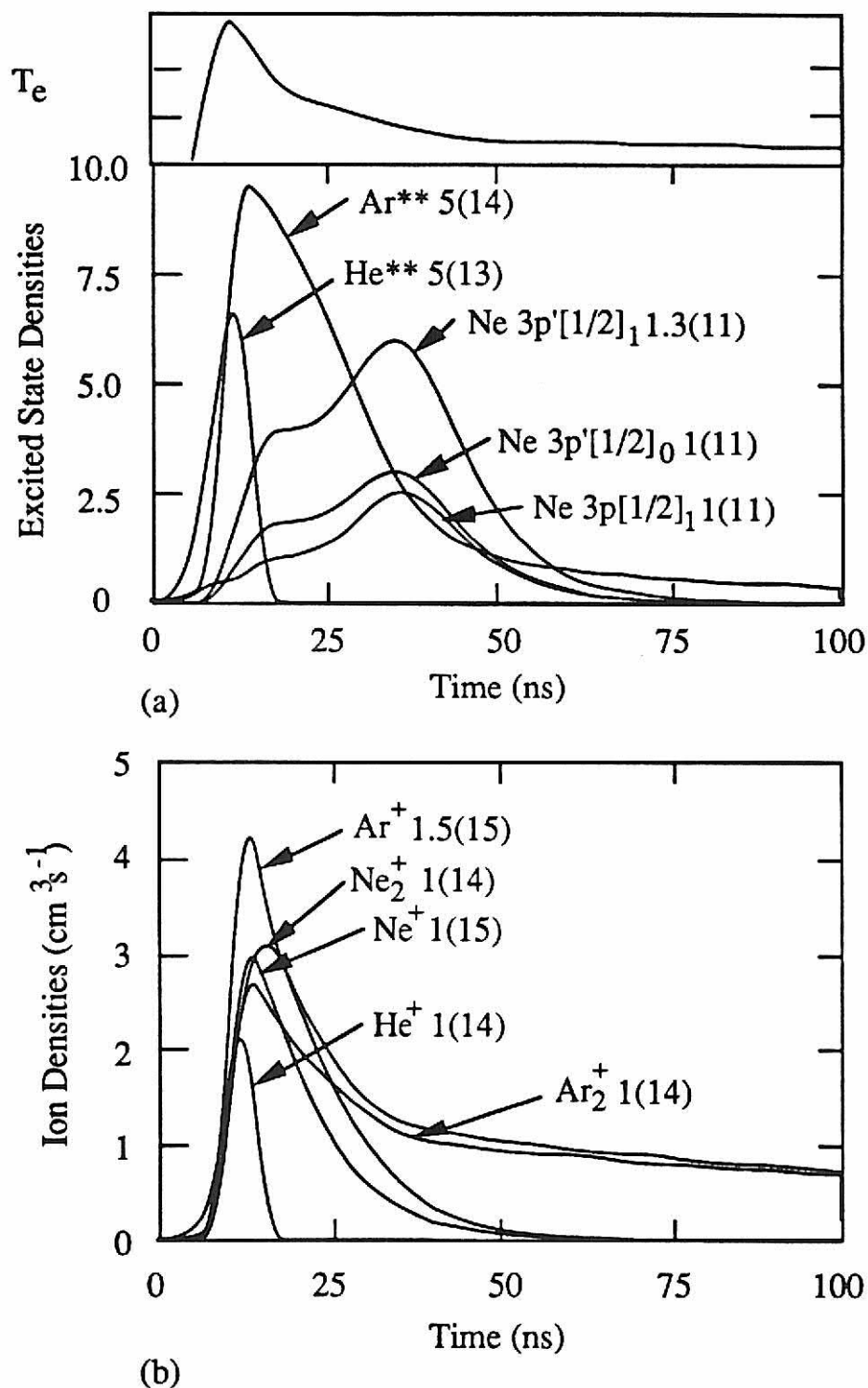
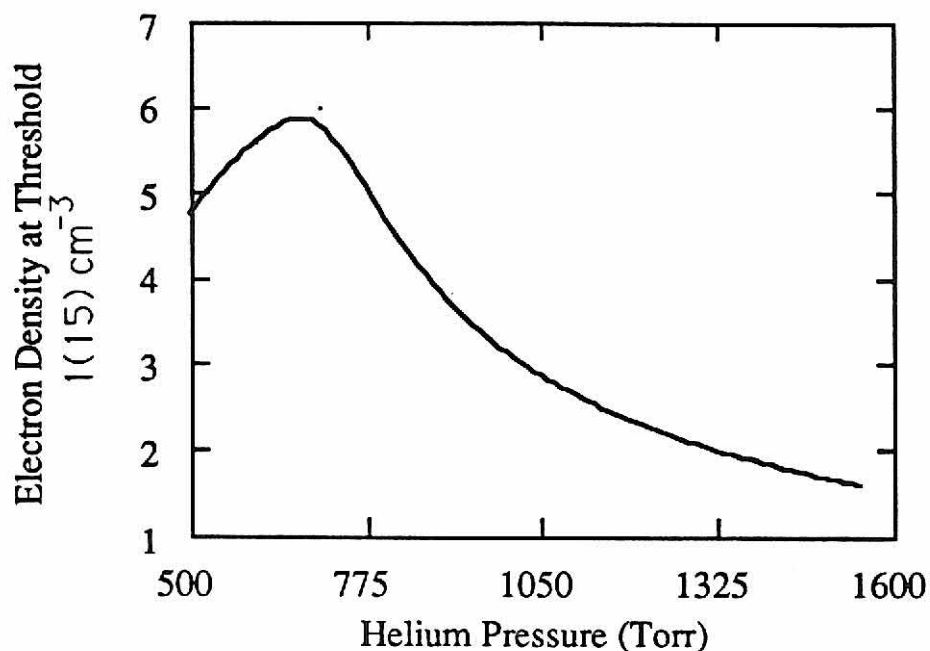
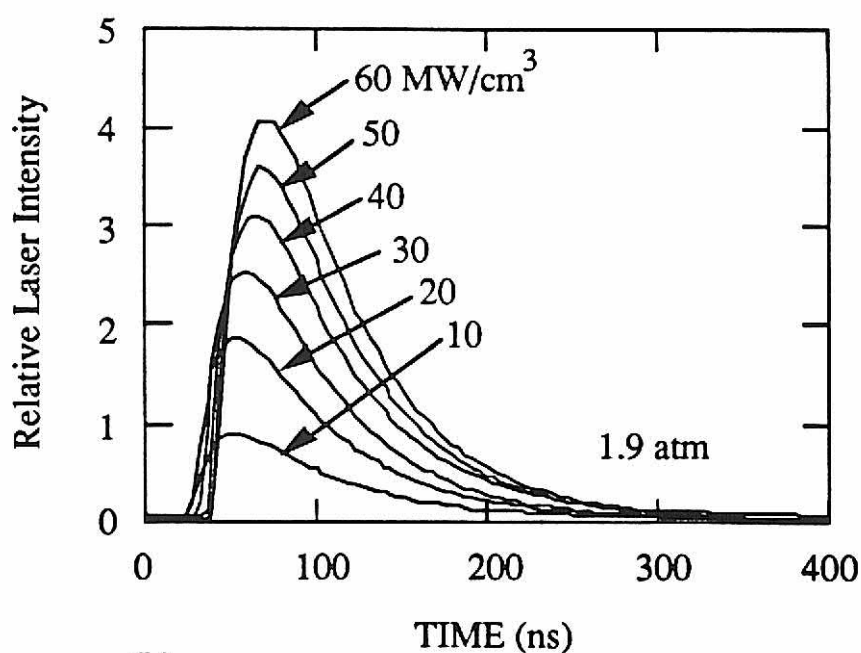


Fig. 4.7. Selected species densities (cm^{-3}) predicted by the model, (a) neutral states and (b) ions. The time dependence of the electron temperature is shown at the top of the figure. The gas mixture is He/Ne/Ar = 0.7/0.2/0.1. The densities of the excited states of argon are much greater than those of He and Ar. The electron distribution does not cool until these states are depleted by superelastic collisions. The normalizing factors for each species' density are shown in the figure.



(a)



(b)

Fig. 4.8. Predicted laser parameters: (a) electron density at the onset of lasing as a function of He partial pressure. The gas mixture is Ne (200 Torr) and Ar (50 Torr) with the indicated amount of He. (b) Laser intensity as a function of pump rate for a He/Ne/Ar = 0.7/0.2/0.1 mixture at 3 atm. Unlike the xenon laser, there is no direct correlation between the onset of lasing and the electron density (or fractional ionization), thereby implying that electron collision mixing is not particularly important. This is confirmed by the nearly linear increase in laser intensity with pump rate.

4.6 References

- ¹ D. Schmieder, D. J. Brink, T. I. Salamon and E. G. Jones, *Opt. Commun.* **36**, 223 (1981).
- ² N. G. Basov, A. Yu. Aleksandrov, V. A. Danilychev, V. A. Dolgikh, O. M. Kerimov, Yu. F. Myznikov, I. G. Rudoi and A. M. Soroka, *Sov. Tech. Phys. Lett.* **11**, 181 (1985).
- ³ N. G. Basov, A. Yu. Aleksandrov, V. A. Danilychev, V. A. Dolgikh, O. M. Kerimov, Yu. F. Myznikov, I. G. Rudoi and A. M. Soroka, *JETP Lett.* **41**, 192 (1985).
- ⁴ F. V. Bunkin, V. I. Derzhiev, G. A. Mesyats, V. S. Skakun, V. F. Tarasenko and S. I. Yakovlenko, *Sov. J. Quant. Electron.* **15**, 159 (1985).
- ⁵ A. Yu. Aleksandrov, V. Yu. Anan'ev, N. G. Basov, V. A. Danilychev, V. A. Dolgikh, A. A. Ionin, O. M. Kermiov, A. P. Lytkin, Yu. F. Myznikov, I. G. Rudoi and A. M. Soroka, *Sov. Phys. Dokl.* **30**, 875 (1985).
- ⁶ A. Yu. Aleksandrov, V. A. Dolgikh, O. M. Kermiov, A. P. Lytkin, Yu. F. Myznikov, G. Rudoi and A. M. Soroka, *Sov. J. Quant. Electron.* **17**, 1521 (1987).
- ⁷ A. Yu. Aleksandrov, V. A. Dolgikh, G. Rudoi and A. M. Soroka, *Sov. J. Quant. Electron.* **18**, 965 (1988).
- ⁸ I. I. Murav'ev, E. V. Chernikova and A. M. Yancharina, *Sov. J. Quant. Electron.* **19**, 123 (1989).
- ⁹ V. A. Vaulin, V. I. Derzhiev, V. M. Lapin, V. N. Slinko, S. S. Sulakshin, S. I. Yakovlenko and A. M. Yancharina, *Sov. J. Quant. Electron.* **19**, 323 (1989).
- ¹⁰ V. I. Derzhiev, A. G. Zhidkov, A. V. Koval, and S. I. Yakovlenko, *Sov. J. Quantum Electron.* **19**, 1016-1021 (1989).
- ¹¹ T. M. Gorbunova, V. I. Derzhiev, Y. P. Mikhailchenko, E. V. Chernikova, S. I. Yakovlenko and A. M. Yancharina, *Sov. J. Quant. Eleceeron.* **20**, 1191 (1990).
- ¹² E. L. Latush, M. F. Sem and G. D. Chebotarev, *Sov. J. Quant. Electron.* **20**, 1327 (1990).
- ¹³ G. A. Hebner and G. N. Hays, *Appl. Phys. Lett.* **57**, 2175-2177 (1990).
- ¹⁴ A. Y. Aleksandrov, V. A. Dolgikh, I. G. Rudoi and A. M. Soroka, *Sov. J. Quant. Electron.* **21**, 611 (1991).
- ¹⁵ A. Y. Aleksandrov, V. A. Dolgikh, I. G. Rudoi and A. M. Soroka, *Sov. J. Quant. Electron.* **21**, 933-937 (1991).
- ¹⁶ P. M. Pramatarov, M. S. Stefonva, M. Ganciu, A. V. Karelin, A. M. Yancharina, J. P. Ivanova and S. I. Yakovlenko, *Appl. Phys. B* **53**, 30 (1991).
- ¹⁷ M. Ganciu, A. Surmeian, C. Diplasu, I. Chera, G. Musa and I-Iovitz Popescu, *Opt. Comm.* **88**, 381 (1992).
- ¹⁸ W. B. Bridges and A. N. Chester, *Appl. Opt.* **4**, 573 (1965).
- ¹⁹ M. J. Kushner, *J. Appl. Phys.* **66**, 2297 (1989).

- ²⁰ R. L. Rhoades and J. T. Verdeyen, *Appl. Phys. Lett.* **60**, 2951 (1992).
- ²¹ F. Kannari, W. D. Kimura, and J. J. Ewing, *J. Appl. Phys.* **68**, 2615, (1990).
- ²² M. Ohwa, T. J. Moratz, and M. J. Kushner, *J. Appl. Phys.* **66**, 5131, (1989).
- ²³ D. L. Albritton, *At. Data Nucl. Tables* **22**, 1-101 (1978).
- ²⁴ R. Johnsen and M. A. Biondi, *J. Chem. Phys.* **73**, 5045-5047 (1980).
- ²⁵ G. E. Veach and H. J. Oskam, *Phys. Rev. A* **2**, 1422-1428 (1970).
- ²⁶ L. A. Levin, S. E. Moody, E. L. Klostermann, R. E. Center and J. J. Ewing, *J. Quantum Electron.* **QE-17**, 2282 (1981).
- ²⁷ P. J. Peters, Y. F. Lan, M. Ohwa, and M. J. Kushner, *IEEE J. Quantum Electron.* **QE-26**, 1964 (1990).

5. EXCITATION MECHANISMS AND GAIN MODELING OF THE HIGH PRESSURE ATOMIC Ar LASER IN He/Ar MIXTURES

5.1 Introduction

The high pressure (≥ 0.5 atm) atomic Ar infrared laser operates on transitions between the 3d and 4p manifolds at wavelengths of 1.27 μm ($3d[3/2]_1 \rightarrow 4p'[1/2]_1$), 1.69 μm ($3d[3/2]_0 \rightarrow 4p[3/2]_2$), 1.79 μm ($3d[1/2]_1 \rightarrow 4p[3/2]_2$), and 2.4 μm ($3d[1/2]_1 \rightarrow 4p'[1/2]_1$). (See Fig. 5.1.) The small amount of atmospheric absorption of the 1.27 and 1.79 μm transitions, the inherent long lifetime of rare gas mixtures, and the demonstrated high efficiency of the atomic Ar laser have renewed interest in optimizing its performance in large systems. For example, a parametric investigation of the fission-fragment excited Ar laser operating at 1.27 and 1.79 μm Ar transitions was recently reported by Hebner and Hays.¹⁻² A peak power efficiency of 1.4% for the 1.79 μm transition at 760 Torr was obtained for He/Ar mixtures having Ar mole fractions of 0.3% - 2.0%. An efficiency of 1.1% was reported for the 1.27 μm transition at 1300 Torr using a He/Ar = 99.88/0.12 mixture.

Voinov et al.³ have also recently reported on fission-fragment excitation of He/Ar and Ne/Ar mixtures in which they obtained lasing in Ar at 1.27, 1.69, and 1.79 μm . A maximum quasi-continuous output power of 390 W at 1.79 μm was obtained with an efficiency of 0.6% using a He/Ar = 99.8/0.2 mixture at 2 atm. Mel'nikov and Sinyanskii⁴ investigated the 1.149 μm transition ($4p[1/2]_1 - 4s'[1/2]_1$) in Ar using fission-fragment pumping and obtained a maximum laser power of 250 W with an efficiency of $\approx 0.1\%$ (He/Ar = 99.6/0.4 at 1520 Torr).

Similar laser performance has been demonstrated using electron beam excitation. Dudin et al.⁵ reported lasing on three Ar transitions (1.27, 1.79, and 2.4 μm) with maximum gains of 0.028 cm^{-1} at 1.79 μm ; and 0.021 cm^{-1} at 2.4 and 1.27 μm . The gas pressure was 2660 Torr and the gas mixture was He/Ar = 99/1. Berkeliev et al.⁶ have reported simultaneous lasing in Ar (1.79 μm) with a 2% efficiency and in N_2 (358 nm) with a 1% efficiency using a He/Ar/ N_2 = 98.2/1.7/0.1 mixture at 2320 Torr.

The maximum theoretical intrinsic laser efficiency for the 1.79 μm transition with respect to the ground state is 2.3%. It is difficult to explain efficiencies of 1-2% obtained in the cited experiments without there being an energy recirculation or electro-ionization process similar to the xenon laser.^{17,18} Electro-ionization in rare gas lasers refers to the recirculation of atomic states from the laser levels to the rare gas metastables followed by electron impact to the ion. Recombination of the ion then repopulates the upper laser level. This process is far more efficient than directly exciting the laser levels or creating ions from the ground state of the rare gas. In the context of this work, we would like to generalize the term "electro-ionization" to include electron impact excitation of metastables to atomic levels higher than the upper laser levels as well as the ion.

To investigate the kinetics leading to high laser efficiency in the high pressure Ar laser, we have developed and parametrized a computer model for the electron and fission-fragment excited laser. Results from the model and comparisons to experiments will be presented, and excitation mechanisms proposed for He/Ar mixtures. Our investigation suggests that dissociative recombination of HeAr^+ leads to excitation of the upper laser level in gas mixtures having moderate mole fractions of Ar (0.001 - 0.01). Self-quenching of the laser levels and population of Ar(4s) by dissociative recombination of Ar_2^+ decreases laser power at higher Ar mole fractions.

The computer model and the proposed kinetics are described in Section 5.2. A comparison of computed and experimental values of laser efficiency, small signal gain, and saturation flux are presented in Section 5.3, followed by our concluding remarks in Sec. 5.4.

5.2 Description of Model

Our computer model is similar to models for particle beam excited excimer lasers,⁷ and to our previously described models for atomic Xe and Ne lasers.^{15,16} The model will therefore be only briefly described.

The model consists of a rate equation analysis of the time dependence of excitation and kinetics of particle-beam-excited He/Ar gas mixtures. There are 31 atomic and ion states included in the model for He, He⁺, Ar, Ar⁺, and their dimer ions (He₂⁺, Ar₂⁺, HeAr⁺, ArHe⁺). Of these species, eight atomic levels of Ar are included to resolve the three laser transitions at 1.27, 1.79 and 2.4 μm. The Ar levels used in the model are listed in Appendix A. Our reaction scheme differs from earlier models of the atomic Ar laser by Wilson et al.⁸ and Basov et al.¹⁹ by including more extensive plasma reaction chemistries and by resolving more transitions. A complete list of reactions included in the model are listed in Appendix B.

The model begins by calculating *W* values (energy deposition/event) for ionization and excitation of all pertinent levels of each component of the gas mixture by the heavy ions. This calculation is performed with a Monte Carlo simulation (MCS) for the injected particles and secondary electrons for individual gas mixtures.⁹ We relate *W* values obtained from an electron slowing calculation to those for heavy ions by using the scaling laws discussed in Ref. 10. The electron temperature is also obtained from the MCS. We parameterized the MCS to obtain a table of electron temperature as a function of excited state, electron densities, and gas mixture. This table was then interpolated during the actual kinetics calculation. The electron temperature and *W* values were then used to obtain rate coefficients and rate equations for all species formulated. The rate equations were then integrated in time using a third-order Runge-Kutta technique. The overall reaction scheme differs little from those used by conventional excimer laser models. Particularly important excitation mechanisms with respect to the Ar laser are discussed below.

The proposed major kinetic pathways in our model are schematically shown in Fig. 5.2. It has previously been suggested that the Ar laser levels are populated by recombination of Ar⁺ and Ar₂⁺.⁸ It has also been suggested that dissociative recombination of HeAr⁺ is an important pumping mechanism for the upper laser level.^{3,5-6} The competition between formation of Ar⁺, Ar₂⁺ and HeAr⁺ therefore largely determines the performance of the laser as a function of gas mixture. Recent experimental results have shown that dissociative recombination of Ar₂⁺,

primarily produces Ar(4s) (branching ratio 0.9), with a small fraction producing the lower laser levels, Ar(4p).¹⁴ Therefore, population of the upper laser level must depend on dissociative recombination of Ar⁺ or HeAr⁺. Previous studies have suggested that collisional radiative recombination of Ar⁺ followed by quenching from higher excited states of Ar is the primary pumping mechanism.⁸ We found that when including a detailed accounting of the Ar excited state kinetics that this mechanism did not reproduce experimental trends for the pumping conditions of interest. This point will be discussed further below.

The fact that recombination of neither Ar⁺ or Ar₂⁺ as a precursor of the upper laser level allowed us to reproduce experiments motivated us to examine the contributions of dissociative recombination of HeAr⁺ to pumping the upper laser level. The rate coefficients for the formation and dissociative recombination of He₂⁺ and Ar₂⁺, as well as the charge transfer reactions between He⁺, He₂⁺, Ar⁺, and Ar₂⁺ are fairly well-known.¹¹⁻¹³ Unfortunately, little is known about the formation and recombination of HeAr⁺. We derived values for these rate coefficients by parameterizing the model and comparing our predictions for laser power to experiments. Although this exercise does not produce a unique set of rate coefficients, it does provide a self-consistent reaction mechanism which reproduces experimental behavior, and therefore is useful for scaling studies.

In deriving these rate coefficients, we relied on a few simple arguments to begin with. For example, the formation of HeAr⁺ by Ar⁺ + He + Ar → HeAr⁺ + Ar should be smaller than the rate of formation of Ar₂⁺ by Ar⁺ + Ar + Ar → Ar₂⁺ + Ar (rate coefficient 2.5 x 10⁻³¹ cm⁶s⁻¹). This requirement stems from the necessity to account for the experimentally observed reduction in laser power at high Ar mole fraction. (At high mole fractions of Ar, contributions of dissociative recombination of Ar₂⁺ to Ar(4p) quenches laser oscillation.) Analogously, the rate coefficient for formation of HeAr⁺ by Ar⁺ + He + He → HeAr⁺ + He should be smaller than the analogous reaction with Ar as the stabilizing collision partner to account for the fact that laser oscillation is weak at small mole fractions of Ar (< 0.001). Following these arguments

with extensive parametric studies, we derived rate coefficients of $2.5 \times 10^{-32} \text{ cm}^6 \text{ s}^{-1}$ for $\text{Ar}^+ + \text{He} + \text{Ar} \rightarrow \text{HeAr}^+ + \text{Ar}$; and $1.0 \times 10^{-32} \text{ cm}^6 \text{ s}^{-1}$ for $\text{Ar}^+ + \text{He} + \text{He} \rightarrow \text{HeAr}^+ + \text{He}$.

Due to the lower binding energy of HeAr^+ compared to Ar_2^+ , its dissociative recombination should populate states higher in the Ar manifold than Ar_2^+ . After parametric studies, we assigned a branching of 0.01 to $\text{Ar}(4d)$ and 0.99 to $\text{Ar}(3d')$ for dissociative recombination of HeAr^+ . The results of model also suggest that the rate coefficient for dissociative recombination of HeAr^+ should be smaller than that of Ar_2^+ ($7.0 \times 10^{-7} / T_e^{-0.5} \text{ cm}^3 \text{ s}^{-1}$) and a value of $7.0 \times 10^{-8} / T_e^{-0.5} \text{ cm}^3 \text{ s}^{-1}$ was assigned.

The dominant clearing mechanisms for lower laser levels are radiative relaxation to $\text{Ar}(4s)$ and collisional quenching by heavy particles. The collisions either remove $\text{Ar}(4p)$ by forming argon dimers or quench the lower laser levels to $\text{Ar}(4s)$. The argon metastables are then dominantly removed by formation of Ar dimers, are elevated by electron impact to higher excited states or are ionized by electron impact. Under typical low power deposition conditions ($\text{He}/\text{Ar} = 99.7/0.03$), 48% of $\text{Ar}(4s)$ atoms are removed by forming Ar dimers, 20% are excited to higher lying levels and less than 1% are ionized by electron impact collisions. The latter two processes contribute to the electro-ionization cycle which allow laser efficiencies to approach the quantum efficiency based on excitation from the ground state. The electro-ionization cycle of the Ar laser is not as efficient as in the Xe laser at low pump rates ($< 100 \text{ s W/cm}^3$) due to the relatively large energy separation between the metastable states and higher excited and ionic states in Ar compared to Xe. This issue will be discussed further in the next section.

The effects of gas heating were neglected in the model with the temperature being fixed at 300 K. Gas heating has been shown to be an important consideration in the Xe atomic laser where increasing gas temperature leads to higher levels of electron collision mixing of the laser levels and eventual quenching of the inversion.¹⁵ By ignoring gas heating in this model, our predictions for laser performance at high energy loading are best-case analyses.

The results of our model have been compared to experiments performed by Hebner and Hays for fission fragment excitation of the Ar laser.¹⁻² The experiments were performed using

the Sandia National Laboratory SPR-III fast burst reactor as a source of fast neutrons. The laser cell gain region was 60 cm long with a rectangular cross section of $1 \times 7 \text{ cm}^2$. The laser cavity was formed by a 4 m radius of curvature (5 cm diameter) maximum reflectivity dielectric mirror, and a flat dielectric output couplers (5 cm diameter) having various reflectivities. The laser output was detected through a bandpass filter with an InAs photodiode. The laser cell was lined with enriched uranium oxide foils. The fast fission neutrons from the reactor were moderated to thermal energies by high density polyethylene surrounding the laser cell. The moderated neutrons induced fissions in the foils, producing energetic fission fragments. A fraction of the fission fragments exit the coatings and deposit their kinetic energy in the gas as ionization and excitation.

5.3 Parametric Study of the Performance of the Argon Laser

Laser parameters as a function of Ar mole fraction in He/Ar mixtures were investigated using the experimental conditions of Hebner and Hays.^{1,2} The gas pressure was 760 Torr and the quasi-continuous power deposition was 100 W cm^{-3} . Predictions for electron temperature and electron density are shown in Fig. 5.3(a) for Ar mole fractions of 10^{-3} to 10%. Ion densities are shown in Fig. 5.3(b). The electron density decreases with increasing Ar mole fraction. This is somewhat counterintuitive since the W value for ionization decreases (more efficient ionization) as the He mole fraction decreases. However, at low Ar mole fractions, the predominant ions are He^+ and He_2^+ . A Helium dimer ion, He_2^+ has a small rate coefficient for dissociative recombination ($5.0 \times 10^{-9} T_e^{-0.5} \text{ cm}^3 \text{ s}^{-1}$) compared to Ar_2^+ and thus the electron density is large, because the rate of loss is small. As the Ar mole fraction increases, HeAr^+ and Ar_2^+ are larger proportions of the ion population. Even though the direct formation of Ar ions is small, Ar^+ ions are produced by charge exchange from He_2^+ and Penning ionizations from He^* and He_2^* . Following the formation of Ar^+ , HeAr^+ is formed by three-body association reactions. The HeAr^+ ion has a maximum density at an Ar mole fraction of $\approx 0.1\%$, whereas the

Ar_2^+ density monotonically increases over the cited range of Ar mole fraction due to the more efficient three-body association rate.

The electron temperature decreases with increasing Ar mole fraction (0.6 eV to 0.35 eV) due primarily to the increasing rate of momentum transfer resulting from collisions with Ar and its excited states. An important difference between our results and those of Wilson et al.⁸ relates to the electron temperature. Wilson et al.⁸ assumed that the electron temperature is near ambient (300 K). The electron temperature in our model is larger due to a recombination heating effect. Since the cross section for recombination scales as $1/\epsilon^n$ (ϵ is the electron energy, $n = 0.5-1.5$), the lowest energy electrons are removed by recombination at the highest rates. This results in raising the average electron energy. Due to Wilson et al. using a low electron temperature, their results emphasized collisional radiative recombination of Ar^+ , which scales as $T_e^{-4.5}$, as a precursor to the upper laser level. In our model which produces a higher T_e , collisional radiative recombination does not significantly affect the kinetics.

Predicted and experimental laser power efficiencies for oscillation at 1.79 μm are shown in Fig. 5.4 as a function of Ar mole fraction. The maximum laser power efficiency occurs at an Ar mole fraction of $\approx 1\%$. Laser oscillation is quenched at Ar mole fractions exceeding 10%. Our predictions agree well with the experiments at Ar mole fractions at and above the peak efficiency, but diverge somewhat at lower mole fractions. The dependence of laser power efficiency on the Ar mole fraction can be explained by the ion densities shown in Fig. 5.3(b).

At low Ar mole fractions, the dominant ions are He^+ and He_2^+ which do not directly contribute to exciting the upper laser levels. As the Ar mole fraction increases towards the optimum values, the densities of HeAr^+ and Ar^+ increase due to more rapid charge transfer to Ar from He^+ and He_2^+ , and more power directly dissipated by ionization of Ar. In our reaction scheme, the upper laser level is dominantly excited by dissociative recombination of HeAr^+ . Although the rate coefficient for the dissociative recombination of HeAr^+ is not large, the large electron and HeAr^+ densities sustain the high rate of recombination to the upper laser level. The increase in Ar_2^+ at higher Ar mole fractions of argon competes with the formation of HeAr^+ ,

thereby decreasing the density of HeAr^+ . Only 10% of the Ar_2^+ recombines to form the lower laser level. Therefore the decrease in laser power at high Ar mole fractions is largely a result of a decrease in the rate of pumping of the upper laser level due to the decrease in the density of HeAr^+ rather than a large increase in the rate of pumping of the lower laser level.

The density of Ar^+ scales similarly to that of HeAr^+ with Ar mole fraction and thus could be identified as a dominant precursor to the upper laser level. The rate coefficient for collisional radiative recombination of Ar^+ scales as $T_e^{-4.5}$. Therefore, at our moderate electron temperatures, its rate of recombination is small. Argon ions, Ar^+ , are dominantly lost by dimer forming reactions rather than by recombination. Lower plasma densities or other conditions which result in lower electron temperatures, as in the work of Wilson et al. will significantly increase the contribution of collisional radiative recombination of Ar^+ to pumping the upper laser level.

The electron temperature and density as a function of pressure are shown in Fig. 5.5(a). The Ar mole fraction is constant at 0.3%. As the pressure increases, the electron temperature decreases due to the larger rate of momentum transfer. The electron density decreases with increasing pressure due to the lower electron temperature which results in larger rates of dissociative recombination. The higher pressure also produces larger rates of three-body dimer ion forming collisions which are followed by dissociative recombination. The densities of various ions as a function of pressure are shown in Fig. 5.5(b). The densities of He^+ and Ar^+ decrease with increasing pressure due to the increasing rate of three-body association reactions which form He_2^+ , HeAr^+ and Ar_2^+ . As the pressure increases further, the enhanced dissociative recombination rates brought by the lower electron temperature limit the further increase of the dimer ions.

The calculated and experimental laser power efficiencies as a function of helium pressure are shown in Fig. 5.6 for the 1.79 μm transition. The experimental results show that the laser power efficiency optimizes near a pressure of 700-800 Torr. The initial rise of the efficiency is due to the increase of the formation of the precursor HeAr^+ . At high pressures, the

formation of Ar_2^+ competes with the formation of HeAr^+ and thus decreases the rate of pumping of the upper laser level. As the pressure increases, collisional broadening of the laser levels also increases, thereby decreasing gain. Additional quenching of the laser levels by dimer formation at the higher pressure also contributes to lowering gain. The predicted laser power efficiencies as a function of pressure generally reproduce the experimental trends; however, we predict higher laser efficiencies at low gas pressures.

The power efficiency of the Ar laser generally increases with increasing power deposition. For example, in the absence of significant gas heating at a power deposition of 100 W cm^{-3} , Hebner and Hays obtained a maximum laser power efficiency of 1.4%. Dudin *et al.* obtained 2.8% laser power efficiency at 10 kW cm^{-3} . Our predictions for laser power efficiencies are shown in Fig. 5.7 without gas heating. The increasing power efficiency may be attributable to increasing contributions of electro-ionization at the higher power levels. Since both the $\text{Ar}(4s)$ and electron densities scale with power P , the contributions of electro-ionization to populating the upper laser level should scale as P^2 , whereas "direct" excitation scales as P . We previously noted that for the experiments of Hebner and Hays,¹⁻² the contributions of electro-ionization are small. However, the high electron densities and high metastable densities at moderate pump rates allow an efficient electro-ionization cycle. This is also demonstrated in Fig. 5.7 where we have plotted a fraction of the formation rates of $\text{Ar}(3d)$ and Ar^+ which are attributable to recirculation as a function of pump rates. The recirculation increases with increasing power deposition thereby allowing more efficient laser operation.

Calculated gain and saturation flux of the He/Ar laser are compared to the experiments in Fig. 5.8 as a function of power deposition for the $1.79 \mu\text{m}$ transition. The gain linearly increases with increasing power deposition at low powers. Experimentally, the gain begins to slightly saturate at higher power deposition, whereas the calculations continue to predict a linear dependence on power deposition. This discrepancy may be attributed to gas heating effects which are not included in this model. (In Xe atomic lasers, it is known that gas heating leads to increased electron collision quenching of the laser levels and a decrease in gain.¹⁵) The

experimental derived saturation flux increases with increasing power deposition whereas the calculated values are relatively constant. The increase in the saturation intensity may again be attributable to gas heating effects which increase the electron collision quenching of the laser levels.

5.4 Concluding Remarks

The kinetics of the high pressure atomic Ar laser using He/Ar gas mixtures have been theoretically investigated, and the results have been compared to experiments using fission fragment excitation. A reaction mechanism in which dissociative recombination of HeAr^+ is a major precursor to the upper laser level reproduce experiment measurements of laser power efficiency as a function of Ar mole fraction and He pressure. For our conditions, collisional radiative recombination of Ar^+ is insufficient to account for the observed gain due to a greater than thermal electron temperature which decreases its rate. At high Ar mole fractions, formation of Ar_2^+ competes with formation of HeAr^+ , thereby decreasing the excitation of the upper laser level and quenching laser oscillation at high Ar mole fractions. Contribution of dissociative recombination of Ar_2^+ to the lower laser level, though small, also contribute to the quenching.

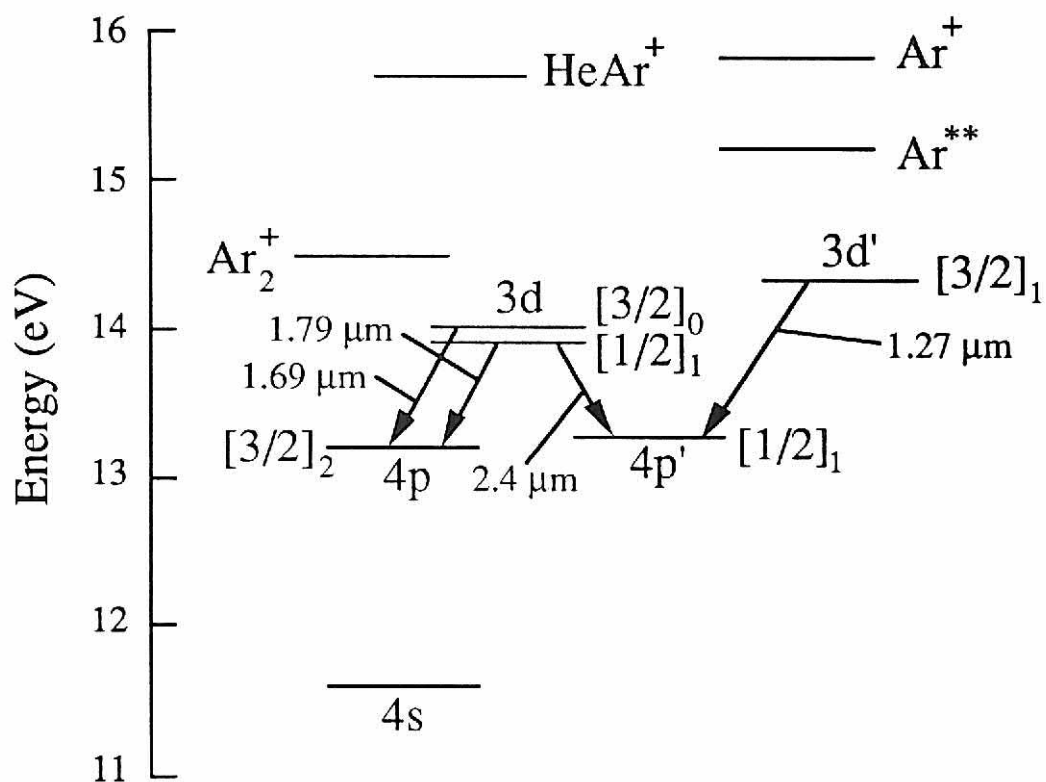
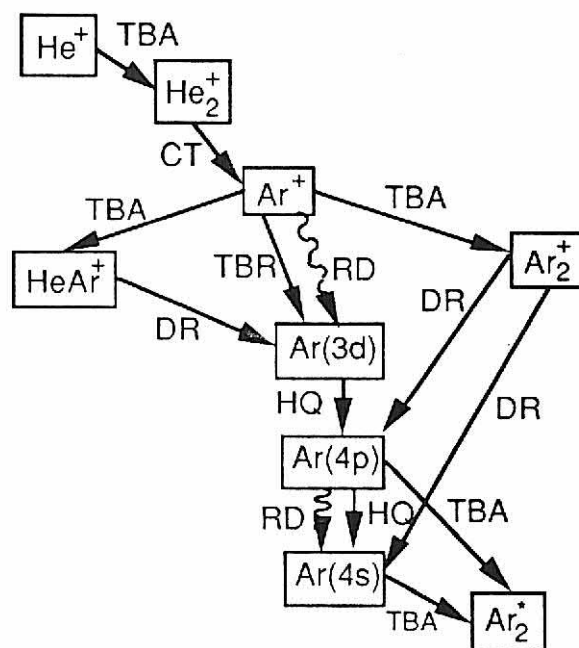
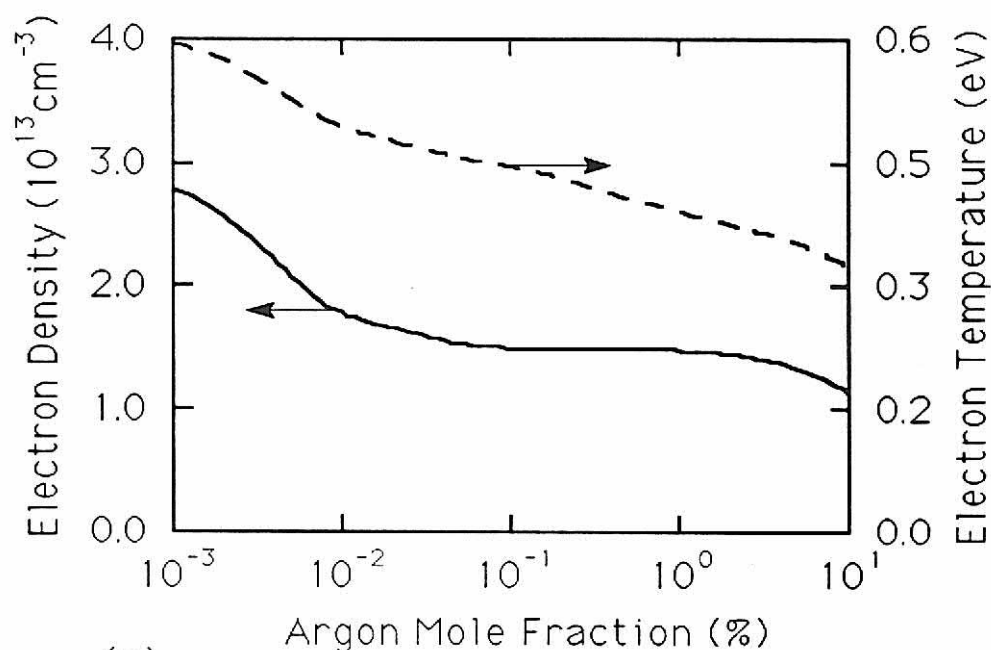


Fig. 5.1. Laser transitions and relevant atomic energy levels of Ar used in the model. The positions of HeAr⁺ and Ar₂⁺ are shown for reference. Laser oscillation at 1.79 μm occurs between Ar(3d[1/2]₁) and Ar(4p[3/2]₂).

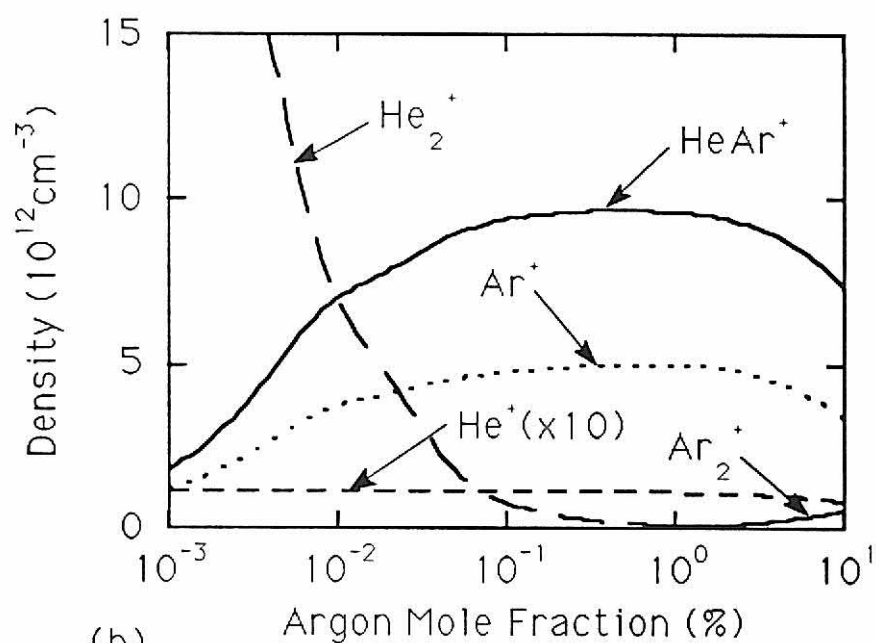


TBA - Three-Body Association
 TBR - Three-Body Recombination
 DR - Dissociative Recombination
 HQ - Heavy Particle Quenching
 RD - Radiative Decay
 CT - Charge Transfer Reaction

Fig. 5.2. Schematic of excitation and quenching pathways for the laser levels of the high pressure atomic Ar laser. In our reaction scheme, excitation of the upper laser levels is dominated by dissociative recombination of HeAr^+ . Quenching of the lower laser level is dominated by radiative relaxation and collisions with Ar.



(a)



(b)

Fig. 5.3. Plasma parameters as a function of Ar mole fraction in He/Ar mixtures (total pressure 760 Torr). (a) Electron temperature and density, and (b) ion densities. The power deposition is 100 W cm^{-3} . As the Ar mole fraction increases, electron temperature and electron density decrease. At intermediate Ar mole fractions, HeAr^+ is the dominant ion which by dissociative recombination excites the upper laser level. Competition from formation of Ar_2^+ decreases the density of HeAr^+ at high Ar mole fractions.

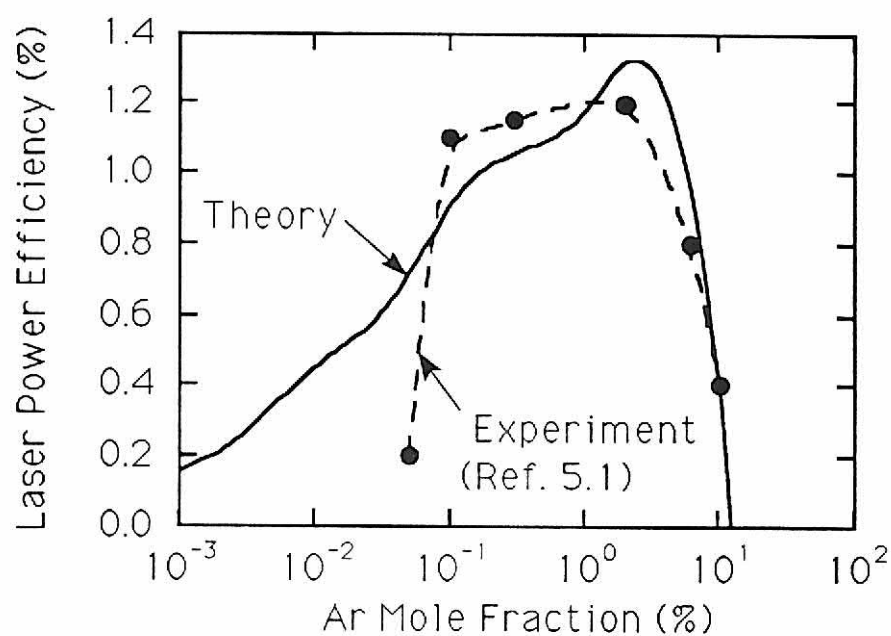


Fig. 5.4. Calculated and experimental laser power efficiency at 1.79 μm as a function of Ar mole fraction for a power deposition of 100 W cm^{-3} and a total pressure of 760 Torr. The decrease in laser power at high Ar mole fraction results from a competition between formation of Ar_2^+ and HeAr^+ .

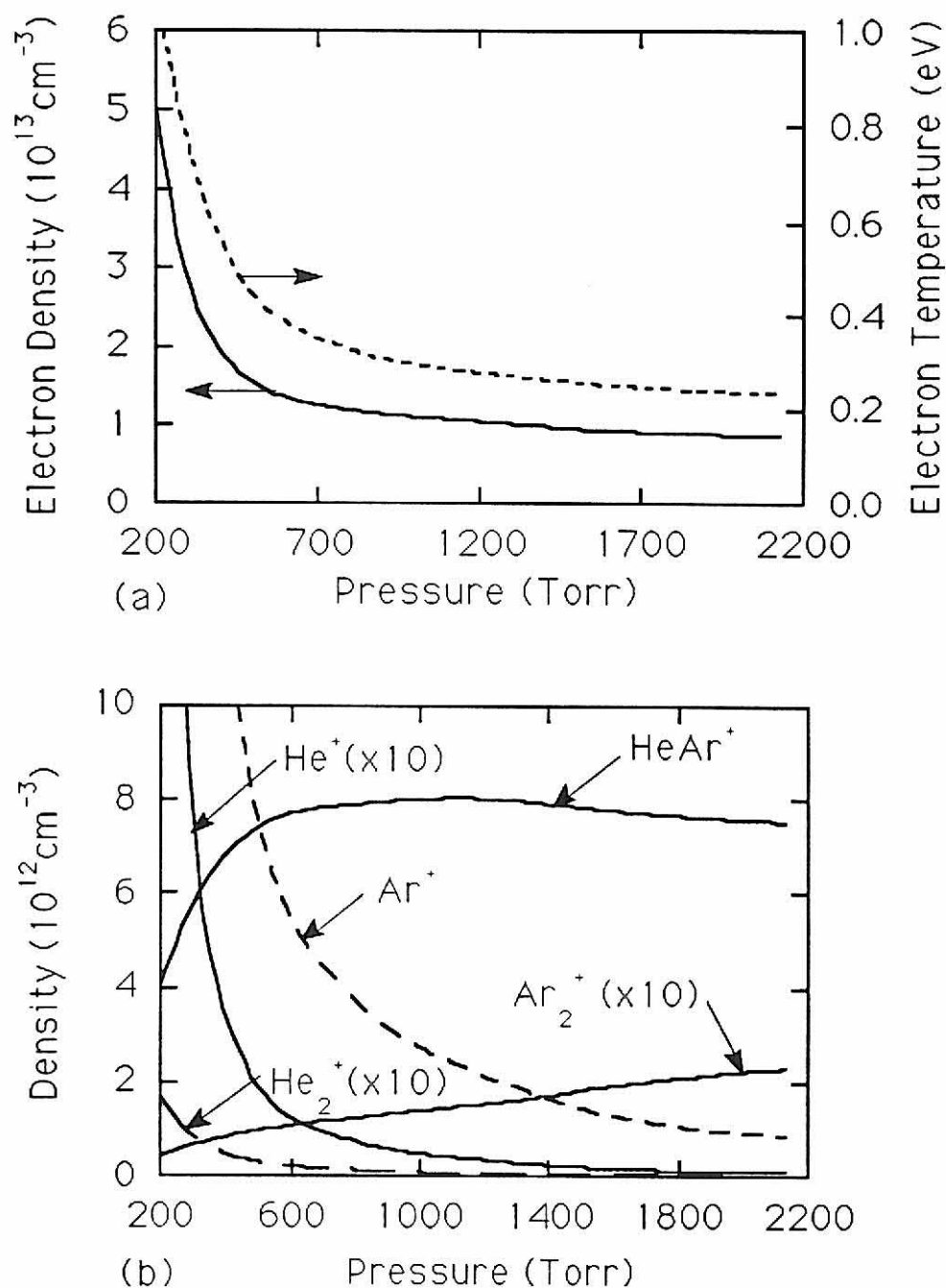


Fig. 5.5. Plasma parameters as a function of pressure in He/Ar=99.7/0.3 mixtures. (a) Electron temperature and density and (b) ion densities. The power deposition is 75 W cm^{-3} . The electron temperature decreases with increasing pressure due to more rapid rates of thermalization. Increasing pressure results in more rapid formation of dimer ions. The electron density then decreases due to high rates of dissociative recombination.

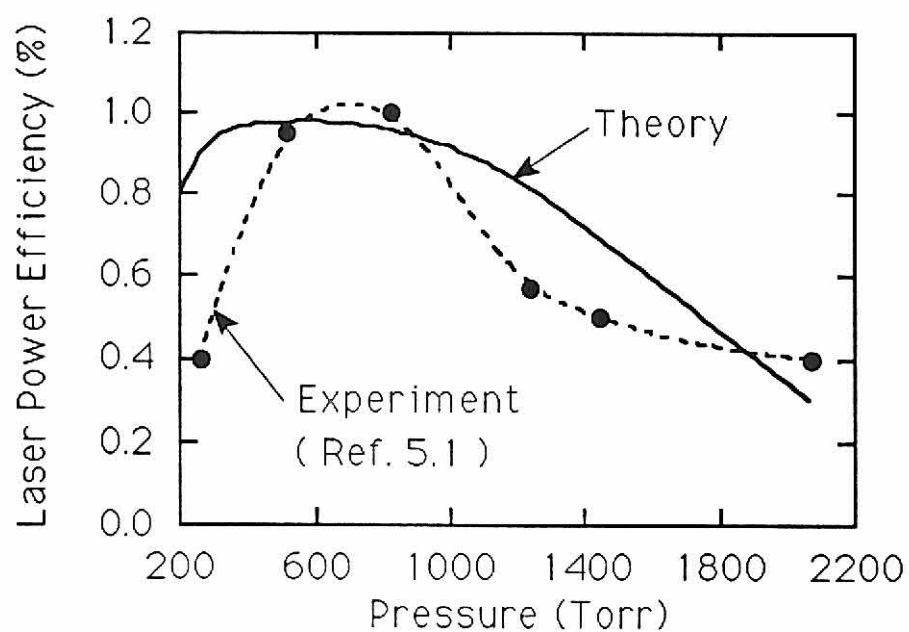


Fig. 5.6. Calculated and experimental laser power efficiency at $1.79 \mu\text{m}$ as a function of pressure. (The Ar mole fraction is 0.3%.) The power deposition is 75 W cm^{-2} . Laser power efficiency decreases at high pressure due to collisional broadening and reduction in the density of HeAr^+ .

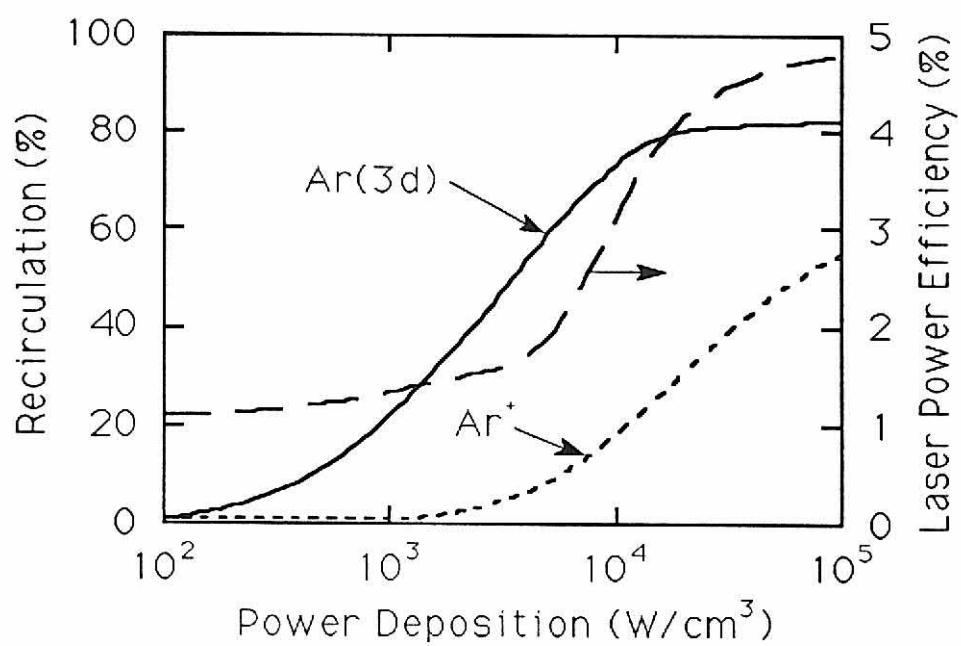


Fig. 5.7. Fraction of rates of formation Ar^+ and $\text{Ar}(3d)$ attributed to recirculation from the Ar metastables as a function of power. Electro-ionization increases sharply at pump rates above $10 \text{ kW}/\text{cm}^3$. Predicted laser power efficiency is also shown (in the absence of gas heating).

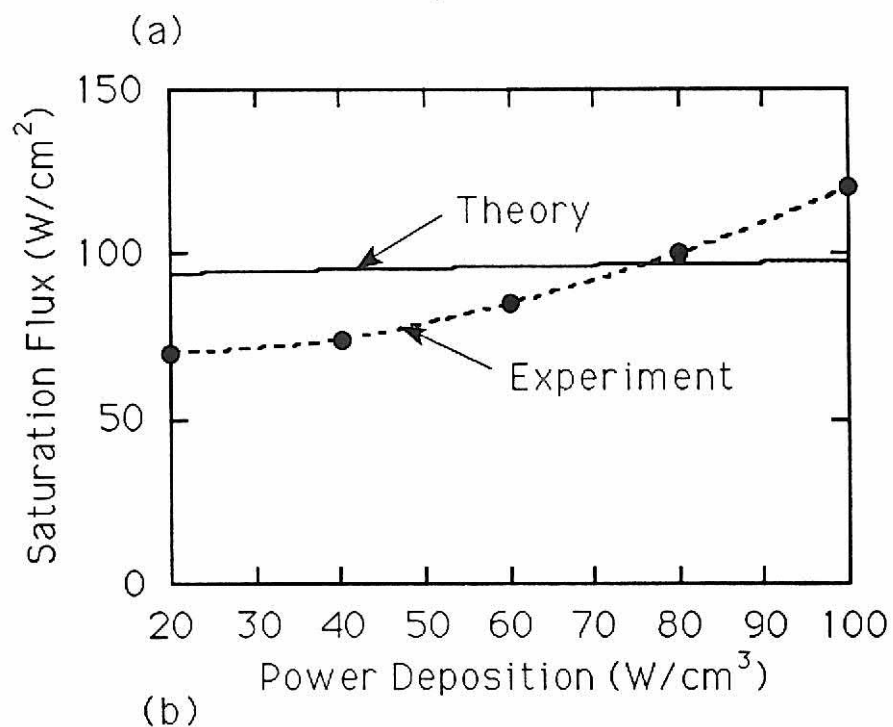
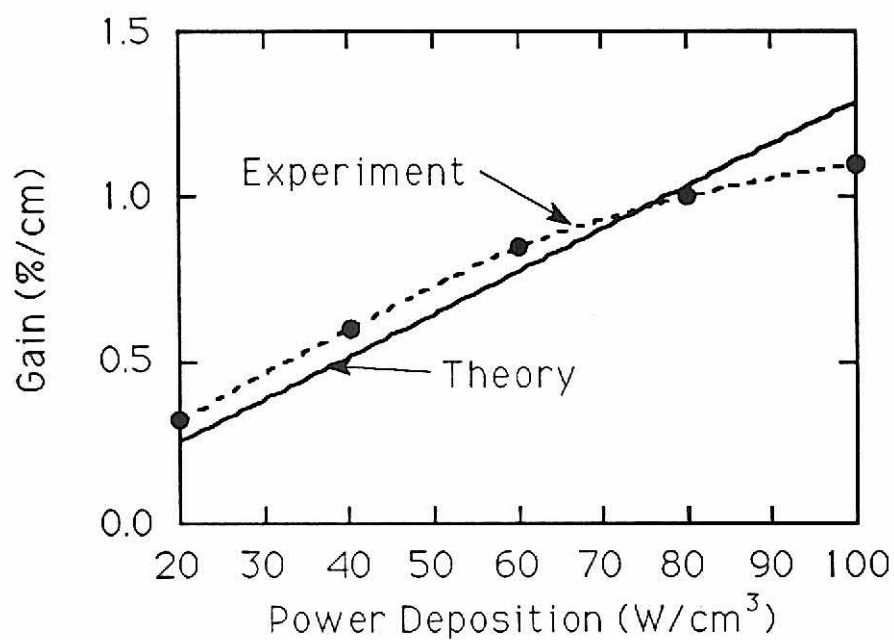


Fig. 5.8. Calculated and experimental laser parameters ($1.79 \mu\text{m}$) as a function of power deposition; (a) gain and (b) saturation flux. The gas mixture is He/Ar = 99.7/0.3 at 760 Torr. Gain increases nearly linearly with power deposition with some amount of saturation at high powers, possibly a consequence of gas heating.

5.5 References

- ¹ G. A. Hebner and G. N. Hays, *J. Appl. Phys.* **71**, 1610 (1992).
- ² G. A. Hebner and G. N. Hays, *J. Appl. Phys.* (submitted 1992).
- ³ A. M. Voinov, V. N. Krivonosov, S. P. Mel'nikov, I. N. Mochkaev, and A. A. Sinyanskii, *Sov. J. Quantum Electron.* **21**, 157 (1991).
- ⁴ S. P. Mel'nikov and A. A. Sinyanskii, *Sov. J. Quantum Electron.* **21**, 1332 (1991).
- ⁵ A. Yu. Dudin, D. A. Zayarnyi, L. V. Semenova, N. N. Ustinovskii, I. V. Kholin, and A. Yu. Chugunov, *Sov. J. Quantum Electron.* **21**, 833 (1991).
- ⁶ B. M. Berkeliev, V. A. Dolgikh, I. G. Rudoi, and A. M. Sorka, *Sov. J. Quantum Electron.* **21**, 250 (1991).
- ⁷ F. Kannari, W. D. Kimura, and J. J. Ewing, *J. Appl. Phys.* **66**, 5131 (1989).
- ⁸ J. W. Wilson, R. J. DeYoung, and W. L. Harries, *J. Appl. Phys.* **50**, 1226 (1979).
- ⁹ M. J. Kushner, *J. Appl. Phys.* **66**, 2297 (1989).
- ¹⁰ T. J. Moratz, T. D. Saunders and M. J. Kushner, *J. Appl. Phys.* **64**, 3799 (1988).
- ¹¹ J. Bretagne, J. Godart and V. Puech, *Beitr. Plasmaphys.* **23**, 295 (1983).
- ¹² C. B. Collins, and F. W. Lee, *J. Chem. Phys.* **70**, 1275 (1979).
- ¹³ C. B. Collins, and F. W. Lee, *J. Chem. Phys.* **68**, 1391 (1978).
- ¹⁴ J. R. Peterson, 44th Gaseous Electronics Conference, Albuquerque, NM. October, 1991, Paper MC-16, 156.
- ¹⁵ J. W. Shon, M. J. Kushner, G. A. Hebner and G. N. Hays, *J. Appl. Phys.* **73**, 2686 (1993).
- ¹⁶ J. W. Shon, R. L. Rhoads, J. T. Verdeyen, and M. J. Kushner, *J. Appl. Phys.* **73**, 8059 (1993).
- ¹⁷ G. A. Hebner, J. W. Shon, and M. J. Kushner, *Appl. Phys. Lett.* (submitted).
- ¹⁸ S. A. Lawton, J. B. Richards, L. A. Newman, L. Specht, and T. A. DeTemple, *J. Appl. Phys.* **50**, 3888 (1979).
- ¹⁹ G. Basov, A. Yu Chugunov, V. A. Danilychev, I. V. Kholin, and M. N. Ustinovskii, *IEEE J. Quantum Electron.* **QE-19**, 126 (1983).
- ²⁰ F. Kannari, A. Suda, M. Obara, and T. Fujioka, *IEEE J. Quantum Electron.* **QE-19**, 1587 (1983).
- ²¹ Y. J. Shiu and M. A. Biondi, *Phys. Rev. A* **17**, 868, (1978).
- ²² D. Smith and M. J. Copsey, *J. Phys. B* **1**, 650 (1968).

- ²³ D. Smith and M. J. Copsey, J. Phys. B **1**, 650 (1968).
- ²⁴ C. B. Collins and F. W. Lee, J. Chem. Phys. **68**, 1391 (1978).
- ²⁵ P. K. Leichner and R. J. Ericson, Phys. Rev. A **9**, 251 (1974).
- ²⁶ R. S. F. Chang and D. W. Setser, J. Chem. Phys. **69**, 3885 (1978).
- ²⁷ G. Bekefi, Principles of Laser Plasmas (Wiley-Interscience, New York, 1976).
- ²⁸ C. B. Collins, H. S. Hicks, W. E. Wells, and R. Burton, Phys. Rev. A **6**, 1545, (1972).
- ²⁹ R. Deloche, P. Monchicourt, M. Cheret, and F. Lambert, Phys. Rev. A **13**, 1140 (1976).

6. CONCLUSIONS

We have developed a computer model to enhance our understanding of kinetics and to optimize the performance of the rare gas lasers. The dimer ions played a significant role in the kinetics of rare gas lasers. The formation of dimer ions is achieved by three-body association reactions; the destruction of the dimer ions is achieved by dissociative recombination, which is the dominant mechanism of electron loss. The branching ratio of the dissociative recombination was the important factor in determining the efficiency of the laser. The hetero dimer ions which are less tightly bound than the homogeneous dimer ions usually branch out to the upper laser levels and higher excited states, while the homogeneous dimer ions feed the lower laser levels and metastables. The rate of dissociative recombination and three-body association depend strongly on the electron and gas temperatures.

From the modeling of the atomic Xe laser, we found that premature termination of gain before the peak of the input power in fission-fragment pumping is most likely attributable to gas heating which increases the electron density and leads to electron collision quenching (ECM). In He/Ar/Xe mixtures, the effects of gas heating are reduced due to the large momentum cross section brought by He. The 2.03 μm transition is dominant over the 1.73 μm transition due to strong quenching of the low laser level of the 2.03 μm transition by He.

From the modeling of the atomic Ne laser, we found that variations of the electron temperature in the afterglow following the e -beam pulse largely determine the time at which laser oscillation starts. Laser oscillation does not occur until the excited states are depleted and electron temperature decreases, thereby increasing the rate of dissociative recombination.

From the modeling of the atomic Ar laser, we identified the dominant excitation mechanism as dissociative recombination of HeAr^+ . Collisional-radiative recombination that used to be thought of as the dominant pump mechanism was not significant due to high electron temperature. Also, electro-ionization at high pump rates enhances the efficiency of the atomic Ar laser.

The atomic Xe laser supports six infrared laser transitions. The results from our model suggest that parametric studies of all six transitions are difficult due to many unknown rates, and branchings lead to lower laser levels. More detailed spectroscopic results are needed to provide an accurate model for multiline excitations in the Xe laser. This aspect is shown for other rare gas lasers such as the atomic Ne and Ar lasers, which also support multiple transitions.

Numerically, the integration method of the model can be improved. When photon processes are included in the laser model, the system of rate equations becomes very stiff. Gear's stiff differential equation solver could improve the run time of the model significantly. However, it is also found that the stiff method can be unfit for a large number of reactions with few other parameter computations such as electron and gas temperatures, which interrupt the system at each iteration.

**APPENDIX. A. LIST OF CHEMICAL SPECIES
PERTINENT TO RARE GAS LASERS**

| <u>Species</u> | <u>Energy (eV)</u> |
|------------------------------|--------------------|
| He [*] | 19.82 |
| He ^{**} | 20.96 |
| He ⁺ | 24.60 |
| He ₂ [*] | 17.97 |
| He ₂ ⁺ | 22.23 |
| Ne ⁺ | 21.56 |
| Ne ₂ [*] | 16.0 |
| Ne ₂ ⁺ | 20.30 |
| Ne(5s) | 20.66 |
| Ne(4s) | 19.77 |
| Ne(3p'[1/2] ₀) | 18.965 |
| Ne(3p'[1/2] ₁) | 18.725 |
| Ne(3p'[3/2] ₁) | 18.702 |
| Ne(3p[3/2] ₁) | 18.624 |
| Ne(3p[5/2] ₃) | 18.565 |
| Ne(3p[1/2] ₁) | 18.381 |
| Ne(3s'[1/2] ₁) | 16.847 |
| Ne(3s'[1/2] ₀) | 16.714 |
| Ne(3s[3/2] ₁) | 16.670 |
| Ne(3s[3/2] ₂) | 16.618 |
| Ar(4s) | 11.60 |
| Ar(4p) | 13.17 |
| Ar(4p') | 13.33 |
| Ar(3d) | 13.86 |

| | |
|------------------------------|-------|
| Ar(3d') | 14.30 |
| Ar ^T | 15.18 |
| Ar ⁺ | 15.76 |
| Ar ₂ [*] | 11.06 |
| Ar ₂ ⁺ | 14.50 |
| Xe ⁺ | 12.13 |
| Xe ₂ [*] | 7.82 |
| Xe ₂ ⁺ | 11.10 |
| Xe ^{**} | 11.50 |
| Xe [*] | 8.32 |
| Xe(7p) | 11.0 |
| Xe(5d[3/2] ₁) | 10.40 |
| Xe(5d[5/2] ₃) | 10.22 |
| Xe(5d[5/2] ₂) | 10.16 |
| Xe(5d[7/2] ₃) | 10.04 |
| Xe(5d[3/2] ₂) | 9.96 |
| Xe(5d[7/2] ₄) | 9.94 |
| Xe(5d[1/2] ₁) | 9.92 |
| Xe(5d[1/2] ₀) | 9.89 |
| Xe(6p[1/2] ₀) | 9.93 |
| Xe(6p[3/2] ₂) | 9.82 |
| Xe(6p[3/2] ₁) | 9.79 |
| Xe(6p[5/2] ₃) | 9.73 |
| Xe(6p[5/2] ₂) | 9.67 |
| Xe(6p[1/2] ₁) | 9.58 |
| Xe(6s') | 9.50 |
| ArXe ⁺ | 11.95 |

| | |
|-------------------|-------|
| XeAr ⁺ | 15.58 |
| HeNe ⁺ | 21.50 |
| HeAr ⁺ | 15.74 |
| HeXe ⁺ | 12.11 |
| NeXe ⁺ | 12.09 |
| NeAr ⁺ | 15.64 |

Note: Ar^T represents higher excited states.

APPENDIX.B. LIST OF PLASMA CHEMICAL REACTIONS PERTINENT TO RARE GAS LASERS

| <u>Electron Beam Excitation</u> | | |
|---|---|-------------|
| <u>Reaction</u> | <u>W values (1 atm; He/Ar=99.7/0.3)</u> | <u>Note</u> |
| $e + \text{He} \rightarrow \text{He}^+ + e + e$ | 47.7 eV/event | a |
| $e + \text{He} \rightarrow \text{He}^{**} + e$ | 101.2 eV/event | a |
| $e + \text{He} \rightarrow \text{He}^* + e$ | 250.4 eV/event | a |
| $e + \text{Ar} \rightarrow \text{Ar}^+ + e + e$ | 767.3 eV/event | a |
| $e + \text{Ar} \rightarrow \text{Ar}^T + e$ | 534.8 eV/event | a |
| $e + \text{Ar} \rightarrow \text{Ar}(4p') + e$ | 534.8 eV/event | a |
| $e + \text{Ar} \rightarrow \text{Ar}(4p) + e$ | 534.8 eV/event | a |
| $e + \text{Ar} \rightarrow \text{Ar}(3d') + e$ | 534.8 eV/event | a |
| $e + \text{Ar} \rightarrow \text{Ar}(3d) + e$ | 534.8 eV/event | a |
| $e + \text{Ar} \rightarrow \text{Ar}(4s) + e$ | 2097.9 eV/event | a |
| <u>Reaction</u> | <u>W values (1.91 atm; He/Ne/Ar = 69/20.7/10.3)</u> | <u>Note</u> |
| $e + \text{He} \rightarrow \text{He}^+ + e + e$ | 221.2 eV/event | a |
| $e + \text{He} \rightarrow \text{He}^{**} + e$ | 294.5 eV/event | a |
| $e + \text{He} \rightarrow \text{He}^* + e$ | 566.3 eV/event | a |
| $e + \text{Ar} \rightarrow \text{Ar}^+ + e + e$ | 118.5 eV/event | a |
| $e + \text{Ar} \rightarrow \text{Ar}^{**} + e$ | 232.8 eV/event | a |
| $e + \text{Ar} \rightarrow \text{Ar}^* + e$ | 741.5 eV/event | a |
| $e + \text{Ne} \rightarrow \text{Ne}^+ + e + e$ | 539.4 eV/event | a |
| $e + \text{Ne} \rightarrow \text{Ne}(5s) + e$ | 1235.0 eV/event | a |
| $e + \text{Ne} \rightarrow \text{Ne}(4s) + e$ | 1235.0 eV/event | a |
| $e + \text{Ne} \rightarrow \text{Ne}(3p'[1/2]_0) + e$ | 1235.0 eV/event | a |

| | | |
|---|-------------------------|-------------|
| $e + \text{Ne} \rightarrow \text{Ne}(3p'[1/2]_1) + e$ | 1235.0 eV/event | a |
| $e + \text{Ne} \rightarrow \text{Ne}(3p'[3/2]_1) + e$ | 1235.0 eV/event | a |
| $e + \text{Ne} \rightarrow \text{Ne}(3p[3/2]_1) + e$ | 1235.0 eV/event | a |
| $e + \text{Ne} \rightarrow \text{Ne}(3p[5/2]_3) + e$ | 1235.0 eV/event | a |
| $e + \text{Ne} \rightarrow \text{Ne}(3p[1/2]_1) + e$ | 1235.0 eV/event | a |
| $e + \text{Ne} \rightarrow \text{Ne}(3s'[1/2]_0) + e$ | 4523.0 eV/event | a |
| $e + \text{Ne} \rightarrow \text{Ne}(3s[3/2]_2) + e$ | 4523.0 eV/event | a |
| <u>Reaction</u> | <u>W values (1 atm:</u> | <u>Note</u> |
| | <u>Ar/Xe=99.7/0.3)</u> | |
| $e + \text{Ar} \rightarrow \text{Ar}^+ + e + e$ | 27.4 eV/event | a |
| $e + \text{Ar} \rightarrow \text{Ar}^{**} + e$ | 71.0 eV/event | a |
| $e + \text{Ar} \rightarrow \text{Ar}^* + e$ | 234.2 eV/event | a |
| $e + \text{Xe} \rightarrow \text{Xe}^+ + e + e$ | 3225.8 eV/event | a |
| $e + \text{Xe} \rightarrow \text{Xe}^* + e$ | 705.9 eV/event | a |
| $e + \text{Xe} \rightarrow \text{Xe}(6p[1/2]_0) + e$ | 1562.5 eV/event | a |
| $e + \text{Xe} \rightarrow \text{Xe}(6p[3/2]_2) + e$ | 1562.5 eV/event | a |
| $e + \text{Xe} \rightarrow \text{Xe}(6p[3/2]_1) + e$ | 1562.5 eV/event | a |
| $e + \text{Xe} \rightarrow \text{Xe}(6p[5/2]_3) + e$ | 1562.5 eV/event | a |
| $e + \text{Xe} \rightarrow \text{Xe}(6p[5/2]_2) + e$ | 1562.5 eV/event | a |
| $e + \text{Xe} \rightarrow \text{Xe}(6p[1/2]_1) + e$ | 1562.5 eV/event | a |

Electron Impact Excitation and Super elastic collisions

| | | |
|--|---|-------------|
| <u>Reaction</u> | <u>Rate Coefficient^b</u> | <u>Ref.</u> |
| $e + \text{Ar} \rightarrow \text{Ar}^+ + e + e$ | $4.0 \times 10^{-12} T_e^{0.5} \exp(-15.8/T_e)$ | 2 |
| $e + \text{Ar} \rightarrow \text{Ar}(3d, 3d') + e$ | $2.0 \times 10^{-12} T_e^{0.5} \exp(-14.2/T_e)$ | 2 |
| | b(3d)=0.5 | |
| | b(3d')=0.5 | |
| $e + \text{Ar} \rightarrow \text{Ar}(4p, 4p') + e$ | $5.0 \times 10^{-12} T_e^{0.5} \exp(-13.3/T_e)$ | 2 |

$$b(4p)=0.5$$

$$b(4p')=0.5$$

| | | |
|--|--|---|
| $e + \text{Ar} \rightarrow \text{Ar}(4s) + e$ | $1.0 \times 10^{-11} T_e^{0.75} \exp(-11.6/T_e)$ | 2 |
| $e + \text{He} \rightarrow \text{He}^+ + e + e$ | $1.5 \times 10^{-9} T_e^{0.68} \exp(-24.6/T_e)$ | 3 |
| $e + \text{He} \rightarrow \text{He}^* + e$ | $4.2 \times 10^{-9} T_e^{-0.31} \exp(-19.8/T_e)$ | 3 |
| $e + \text{He} \rightarrow \text{He}^{**} + e$ | $7.7 \times 10^{-9} T_e^{-0.31} \exp(-20.9/T_e)$ | 3 |
| $e + \text{He}^* \rightarrow \text{He}^{**} + e$ | $4.36 \times 10^{-7} T_e^{0.32} \exp(-1.14/T_e)$ | 3 |
| $e + \text{He}^* \rightarrow \text{He}^+ + e + e$ | $1.28 \times 10^{-7} T_e^{0.6} \exp(-4.78/T_e)$ | 3 |
| $e + \text{Ar}^* \rightarrow \text{Ar}^+ + e + e$ | $1.0 \times 10^{-10} T_e^3 \exp(-4.16/T_e)$ | 2 |
| $e + \text{Ar}^* \rightarrow \text{Ar}(3d, 3d') + e$ | $2.0 \times 10^{-7} T_e \exp(-2.7/T_e)$ | 2 |

$$b(3d)=0.5$$

$$b(3d)=0.5$$

| | | |
|--|--|---|
| $e + \text{Ar}^* \rightarrow \text{Ar}(4p, 4p') + e$ | $2.0 \times 10^{-7} T_e \exp(-13.3/T_e)$ | 2 |
|--|--|---|

$$b(4p)=0.5$$

$$b(4p')=0.5$$

| | | |
|---|---|---|
| $e + \text{Ne} \rightarrow \text{Ne}^+ + e + e$ | $1.65 \times 10^{-9} T_e^{0.724} \exp(-21.6/T_e)$ | 3 |
| $e + \text{Ne} \rightarrow \text{Ne}^* + e$ | $5.1 \times 10^{-10} T_e^{1.69} \exp(-16.6/T_e)$ | 3 |
| $e + \text{Ne} \rightarrow \text{Ne}^{**} + e$ | $5.9 \times 10^{-12} T_e^{-0.48} \exp(-18.5/T_e)$ | 3 |
| $e + \text{Ne}^* \rightarrow \text{Ne}^{**} + e$ | $4.36 \times 10^{-8} T_e^{0.32} \exp(-1.90/T_e)$ | 3 |
| $e + \text{Ne}^* \rightarrow \text{Ne}^+ + e + e$ | $4.41 \times 10^{-8} T_e^{0.74} \exp(-4.94/T_e)$ | 3 |
| $e + \text{Xe} \rightarrow \text{Xe}^+ + e + e$ | $3.47 \times 10^{-8} T_e^{0.72} \exp(-12.13/T_e)$ | 3 |
| $e + \text{Xe} \rightarrow \text{Xe}^* + e$ | $1.2 \times 10^{-8} T_e^{-0.72} \exp(-8.32/T_e)$ | 3 |
| $e + \text{Xe} \rightarrow \text{Xe}^{**} + e$ | $2.8 \times 10^{-8} T_e^{-0.725} \exp(-9.73/T_e)$ | 3 |
| $e + \text{Xe}^* \rightarrow \text{Xe}^{**} + e$ | $2.71 \times 10^{-6} T_e^{0.71} \exp(-0.63/T_e)$ | 3 |
| $e + \text{Xe}^* \rightarrow \text{Xe}^+ + e + e$ | $7.58 \times 10^{-8} T_e^{0.71} \exp(-3.81/T_e)$ | 3 |

Dissociative Recombination Reaction

| | | |
|---|---------------------------------|---|
| $e + \text{He}_2^+ \rightarrow \text{He}^* + \text{He}$ | $5.0 \times 10^{-9} T_e^{-0.5}$ | 4 |
|---|---------------------------------|---|

| | | |
|--|----------------------------------|---|
| $e + Ar_2^+ \rightarrow Ar(3d,3d')+Ar$ | $4.0 \times 10^{-8} T_e^{-0.67}$ | 5 |
| | $b(3d)=0.75$ | |
| | $b(3d')=0.25$ | |
| $e + Ar_2^+ \rightarrow Ar(4p,4p')+Ar$ | $6.0 \times 10^{-8} T_e^{-0.67}$ | 5 |
| | $b(4p)=0.833$ | |
| | $b(4p')=0.167$ | |
| $e + Ar_2^+ \rightarrow Ar(4s)+Ar$ | $6.0 \times 10^{-7} T_e^{-0.67}$ | 5 |
| $e+HeAr^+ \rightarrow Ar(3d,3d')+He$ | $6.3 \times 10^{-8} T_e^{-0.5}$ | c |
| | $b(3d)=0.714$ | |
| | $b(3d')=0.286$ | |
| $e+HeAr^+ \rightarrow Ar(4p,4p')+He$ | $7.0 \times 10^{-10} T_e^{-0.5}$ | c |
| | $b(4p)=0.5$ | |
| | $b(4p')=0.5$ | |
| $e + Xe_2^+ \rightarrow Xe(6s',7p)+Xe$ | $3.7 \times 10^{-7} T_e^{-0.5}$ | 5 |
| | $b(7p)=0.1$ | |
| | $b(6s')=0.9$ | |
| $e+ArXe^+ \rightarrow Xe(7p,**)+Ar$ | $1.0 \times 10^{-7} T_e^{-0.5}$ | c |
| | $b(7p)=0.7$ | |
| | $b(Xe^{**})=0.3$ | |
| $e + Ne_2^+ \rightarrow Ne(3p',3s)+Xe$ | $3.7 \times 10^{-8} T_e^{-0.5}$ | 5 |
| | $b(3p')=0.4$ | |
| | $b(3s)=0.6$ | |

Three-Body Association

| | | |
|--|-----------------------------------|---|
| $He^+ + He + He \rightarrow He_2^+ + He$ | $2 \times 10^{-31} cm^6 s^{-1}$ | 6 |
| $Ar^+ + Ar + Ar \rightarrow Ar_2^+ + Ar$ | $2.5 \times 10^{-31} cm^6 s^{-1}$ | 7 |
| $He^+ + He + Ar \rightarrow HeAr^+ + He$ | $2.5 \times 10^{-32} cm^6 s^{-1}$ | 6 |
| $He^+ + Ar + Ar \rightarrow Ar_2^+ + He$ | $1.0 \times 10^{-31} cm^6 s^{-1}$ | 6 |

| | | |
|---|---|----|
| $\text{Ne}^+ + \text{Ne} + \text{Ne} \rightarrow \text{Ne}_2^+ + \text{Ne}$ | $4.4 \times 10^{-32} \text{cm}^6 \text{s}^{-1}$ | 15 |
| $\text{Ne}^+ + \text{He} + \text{He} \rightarrow \text{HeNe}^+ + \text{He}$ | $2.1 \times 10^{-32} \text{cm}^6 \text{s}^{-1}$ | 15 |
| $\text{Xe}^+ + \text{Ar} + \text{Ar} \rightarrow \text{ArXe}^+ + \text{Ar}$ | $1.0 \times 10^{-31} \text{cm}^6 \text{s}^{-1}$ | 14 |
| $\text{Xe}^+ + \text{Xe} + \text{Xe} \rightarrow \text{Xe}_2^+ + \text{Xe}$ | $2.5 \times 10^{-31} \text{cm}^6 \text{s}^{-1}$ | 13 |

Penning Ionization: and Charge and Excitation Transfer

| | | |
|---|---|---|
| $\text{He}_2^+ + \text{Ar} \rightarrow \text{Ar}^+ + \text{He} + \text{He}$ | 2.2×10^{-10} | 8 |
| $\text{He}_2^+ + \text{Ar} + \text{M} \rightarrow$ | $2.4 \times 10^{-29} \text{cm}^6 \text{s}^{-1}$ | 8 |
| $\text{Ar}^+ + \text{He} + \text{He} + \text{M}$ | | |
| $\text{Ar}(4s) + \text{Ar}(4s) \rightarrow \text{Ar}^+ + \text{Ar} + e$ | 5.0×10^{-10} | 9 |
| $\text{Ar}(4p, 4p') + \text{Ar}(4p, 4p') \rightarrow$ | 5.0×10^{-10} | 9 |
| $\text{Ar}^+ + \text{Ar} + e$ | | |
| $\text{He}^* + \text{He}^* \rightarrow \text{He}^+ + \text{He}$ | 2.7×10^{-10} | 3 |
| $\text{He}_2^* + \text{Ar} \rightarrow \text{Ar}^+ + \text{He} + \text{He} + e$ | 3.1×10^{-10} | 4 |
| $\text{Ne}(3s) + \text{Ar} \rightarrow \text{Ar}^+ + \text{Ne} + e$ | 3.0×10^{-10} | |
| $\text{He}^* + \text{Ar} \rightarrow \text{Ar}^+ + \text{He} + e$ | 2.1×10^{-10} | 4 |
| $\text{He}^* + \text{Ar} \rightarrow \text{HeAr}^+ + e$ | 4.7×10^{-11} | 4 |

Heavy Particle Quenching^d

| | | |
|--|------------------------|----|
| $\text{Ar}(3d, 3d') + \text{Ar} \rightarrow$ | 1.0×10^{-11} | 10 |
| $\text{Ar}(4p, 4p') + \text{Ar}$ | | |
| $\text{Xe}(6p[1/2]_0) + \text{Xe} \rightarrow$ | 1.33×10^{-12} | 10 |
| $\text{Xe}(6p[3/2]_2) + \text{Xe}$ | | |
| $\text{Xe}(6p[1/2]_0) + \text{Xe} \rightarrow$ | 8.7×10^{-13} | 10 |
| $\text{Xe}(6p[3/2]_1) + \text{Xe}$ | | |
| $\text{Xe}(6p[1/2]_0) + \text{Xe} \rightarrow$ | 1.58×10^{-12} | 10 |
| $\text{Xe}(6p[5/2]_3) + \text{Xe}$ | | |
| $\text{Xe}(6p[1/2]_0) + \text{Xe} \rightarrow$ | 1.29×10^{-12} | 10 |
| $\text{Xe}(6p[5/2]_2) + \text{Xe}$ | | |

| | | |
|--------------------------------|--------------------------|----|
| Xe(6p[1/2] ₀)+Xe → | 9.0 x 10 ⁻¹³ | 10 |
| Xe(6s')+Xe | | |
| Xe(6p[3/2] ₂)+Xe → | 1.3 x 10 ⁻¹¹ | 10 |
| Xe(6p[3/2] ₁)+Xe | | |
| Xe(6p[3/2] ₂)+Xe → | 2.9 x 10 ⁻¹¹ | 10 |
| Xe(6p[5/2] ₃)+Xe | | |
| Xe(6p[3/2] ₂)+Xe → | 2.8 x 10 ⁻¹¹ | 10 |
| Xe(6p[5/2] ₂)+Xe | | |
| Xe(6p[3/2] ₂)+Xe → | 1.0 x 10 ⁻¹² | 10 |
| Xe(6p[1/2] ₁)+Xe | | |
| Xe(6p[3/2] ₂)+Xe → | 1.9 x 10 ⁻¹¹ | 10 |
| Xe(6s')+Xe | | |
| Xe(6p[3/2] ₁)+Xe → | 1.2 x 10 ⁻¹⁰ | 10 |
| Xe(6p[5/2] ₃)+Xe | | |
| Xe(6p[3/2] ₁)+Xe → | 1.24 x 10 ⁻¹⁰ | 10 |
| Xe(6s')+Xe | | |
| Xe(6p[5/2] ₃)+Xe → | 3.4 x 10 ⁻¹¹ | 10 |
| Xe(6p[5/2] ₂)+Xe | | |
| Xe(6p[5/2] ₃)+Xe → | 1.8 x 10 ⁻¹¹ | 10 |
| Xe(6p[5/2] ₂)+Xe | | |
| Xe(6p[5/2] ₃)+Xe → | 2.1 x 10 ⁻¹¹ | 10 |
| Xe(6s')+Xe | | |
| Xe(6p[5/2] ₂)+Xe → | 2.03 x 10 ⁻¹⁰ | 10 |
| Xe(6p[1/2] ₁)+Xe | | |
| Xe(6p[5/2] ₂)+Xe → | 1.8 x 10 ⁻¹⁰ | 10 |
| Xe(6s')+Xe | | |

| | | |
|--|------------------------|----|
| $\text{Xe}(6p[1/2]_1)+\text{Xe} \rightarrow$ | 1.33×10^{-10} | 10 |
| $\text{Xe}(6s')+\text{Xe}$ | | |
| $\text{Xe}(6p[1/2]_1)+\text{Xe} \rightarrow \text{Xe}^*+\text{Xe}$ | 2.0×10^{-11} | 10 |
| $\text{Xe}(6p[1/2]_0)+\text{He} \rightarrow$ | 6.0×10^{-12} | 18 |
| $\text{Xe}(6p[3/2]_2)+\text{He}$ | | |
| $\text{Xe}(6p[1/2]_0)+\text{He} \rightarrow$ | 1.4×10^{-11} | 18 |
| $\text{Xe}(5d[1/2]_1)+\text{He}$ | | |
| $\text{Xe}(6p[3/2]_2)+\text{He} \rightarrow$ | 1.1×10^{-12} | 18 |
| $\text{Xe}(6p[3/2]_1)+\text{He}$ | | |
| $\text{Xe}(6p[3/2]_2)+\text{He} \rightarrow$ | 6.0×10^{-13} | 18 |
| $\text{Xe}(6p[5/2]_3)+\text{He}$ | | |
| $\text{Xe}(6p[3/2]_1)+\text{He} \rightarrow$ | 7.49×10^{-11} | 18 |
| $\text{Xe}(6p[5/2]_3)+\text{He}$ | | |
| $\text{Xe}(6p[5/2]_3)+\text{He} \rightarrow$ | 4.0×10^{-12} | 18 |
| $\text{Xe}(6p[5/2]_2)+\text{He}$ | | |
| $\text{Xe}(6p[5/2]_2)+\text{He} \rightarrow$ | 7.7×10^{-12} | 18 |
| $\text{Xe}(6p[1/2]_1)+\text{He}$ | | |
| $\text{Xe}(6p[5/2]_2)+\text{He} \rightarrow$ | 2.0×10^{-12} | 18 |
| $\text{Xe}(6s')+\text{He}$ | | |
| $\text{Xe}(6p[1/2]_1)+\text{He} \rightarrow$ | 4.0×10^{-11} | 18 |
| $\text{Xe}(6s')+\text{He}$ | | |
| $\text{Xe}(6s')+\text{He} \rightarrow \text{Xe}^*+\text{He}$ | 6.0×10^{-13} | 18 |
| $\text{Xe}(6p[1/2]_0)+\text{Ne} \rightarrow$ | 9.7×10^{-12} | 18 |
| $\text{Xe}(6p[3/2]_2)+\text{Ne}$ | | |
| $\text{Xe}(6p[1/2]_0)+\text{Ne} \rightarrow$ | 2.43×10^{-11} | 18 |
| $\text{Xe}(5d[1/2]_1)+\text{Ne}$ | | |

| | | |
|---------------------------------------|--------------------------|----|
| Xe(6p[3/2] ₂)+Ne → | 4.0 x 10 ⁻¹⁴ | 18 |
| Xe(6p[3/2] ₁)+Ne | | |
| Xe(6p[3/2] ₂)+Ne → | 3.0 x 10 ⁻¹⁴ | 18 |
| Xe(6p[5/2] ₃)+Ne | | |
| Xe(6p[3/2] ₂)+Ne → | 3.0 x 10 ⁻¹⁴ | 18 |
| Xe(6p[5/2] ₂)+Ne | | |
| Xe(6p[3/2] ₂)+Ne → | 6.0 x 10 ⁻¹⁴ | 18 |
| Xe(s')+Ne | | |
| Xe(6p[3/2] ₁)+Ne → | 1.3 x 10 ⁻¹³ | 18 |
| Xe(6p[5/2] ₃)+Ne | | |
| Xe(6p[3/2] ₁)+Ne → | 1.99 x 10 ⁻¹⁴ | 18 |
| Xe(6p[1/2] ₁)+Ne | | |
| Xe(6p[3/2] ₁)+Ne → | 1.6 x 10 ⁻¹³ | 18 |
| Xe(6s')+Ne | | |
| Xe(6p[5/2] ₃)+Ne → | 1.0 x 10 ⁻¹² | 18 |
| Xe(6p[5/2] ₂)+Ne | | |
| Xe(6p[5/2] ₃)+Ne → | 1.2 x 10 ⁻¹² | 18 |
| Xe(6p[1/2] ₁)+Ne | | |
| Xe(6p[5/2] ₂)+Ne → | 5.3 x 10 ⁻¹² | 18 |
| Xe(6p[1/2] ₁)+Ne | | |
| Xe(6p[5/2] ₂)+Ne → | 1.0 x 10 ⁻¹⁴ | 18 |
| Xe(6s')+Ne | | |
| Xe(6p[1/2] ₁)+Ne → | 2.0 x 10 ⁻¹³ | 18 |
| Xe(6s')+Ne | | |
| Xe(6p[1/2] ₁)+Ne → Xe*+Ne | 2.3 x 10 ⁻¹⁴ | 18 |
| Xe(6s')+Ne → Xe*+Ne | 1.0 x 10 ⁻¹³ | 18 |

| | | |
|--------------------------------|-------------------------|----|
| Xe(6p[1/2] ₀)+Ar → | 1.0 x 10 ⁻¹¹ | 10 |
| Xe(6p[3/2] ₂)+Ar | | |
| Xe(6p[1/2] ₀)+Ar → | 1.3 x 10 ⁻¹⁰ | 10 |
| Xe(5d[1/2] ₁)+Ar | | |
| Xe(6p[3/2] ₂)+Ar → | 1.4 x 10 ⁻¹¹ | 10 |
| Xe(6p[3/2] ₁)+Ar | | |
| Xe(6p[3/2] ₂)+Ar → | 1.4 x 10 ⁻¹¹ | 10 |
| Xe(6p[5/2] ₃)+Ar | | |
| Xe(6p[3/2] ₂)+Ar → | 1.9 x 10 ⁻¹¹ | 10 |
| Xe(6p[5/2] ₂)+Ar | | |
| Xe(6p[3/2] ₁)+Ar → | 1.0 x 10 ⁻¹¹ | 10 |
| Xe(6p[5/2] ₃)+Ar | | |
| Xe(6p[5/2] ₃)+Ar → | 2.6 x 10 ⁻¹¹ | 10 |
| Xe(6p[5/2] ₂)+Ar | | |
| Xe(6p[5/2] ₂)+Ar → | 5.4 x 10 ⁻¹¹ | 10 |
| Xe(6p[1/2] ₁)+Ar | | |
| Xe(6p[5/2] ₂)+Ar → | 2.3 x 10 ⁻¹¹ | 10 |
| Xe(6s')+Ar | | |
| Xe(6p[1/2] ₁)+Ar → | 6.0 x 10 ⁻¹² | 10 |
| Xe(6s')+Ar | | |
| Xe(6s')+Ar → Xe*+Ar | 1.0 x 10 ⁻¹³ | 10 |

Collisional Radiative Recombination

| | | |
|--|---|----|
| Ne ⁺ +e+e → Ne ^{**} +e | 1.0 x 10 ⁻¹⁹ cm ⁶ s ⁻¹ | 11 |
| Ne ⁺ +e+M → Ne ^{**} +M | 1.0 x 10 ⁻²⁶ cm ⁶ s ⁻¹ | 11 |
| Xe ⁺ +e+e → Xe ^{**} +e | 1.0 x 10 ⁻¹⁹ cm ⁶ s ⁻¹ | 11 |
| Xe ⁺ +e+M → Xe ^{**} +M | 1.0 x 10 ⁻²⁶ cm ⁶ s ⁻¹ | 11 |
| Ar ⁺ +e+e → Ar ^{**} +e | 1.0 x 10 ⁻¹⁹ cm ⁶ s ⁻¹ | 11 |

| | | |
|--|---|----|
| $\text{Ar}^+ + e + M \rightarrow \text{Ar}^{**} + M$ | $1.0 \times 10^{-26} \text{cm}^6 \text{s}^{-1}$ | 11 |
| $\text{He}^+ + e + e \rightarrow \text{He}^{**} + e$ | $7.1 \times 10^{-20} \text{cm}^6 \text{s}^{-1}$ | 11 |
| $\text{He}^+ + e + M \rightarrow \text{He}^{**} + M$ | $1.0 \times 10^{-26} \text{cm}^6 \text{s}^{-1}$ | 11 |

Radiative Relaxation

| | | |
|---|----------------------------------|----|
| $\text{Ne}(5s) \rightarrow \text{Ne}(3p', 3p)$ | $5.0 \times 10^6 \text{s}^{-1}$ | 10 |
| $\text{Ne}(4s) \rightarrow \text{Ne}(3p', 3p)$ | $5.0 \times 10^6 \text{s}^{-1}$ | 10 |
| $\text{Ne}(3p') \rightarrow \text{Ne}$ | $6.0 \times 10^7 \text{s}^{-1}$ | 10 |
| $\text{Ne}(3p', 3p) \rightarrow \text{Ne}(3s', 3s)$ | $5.0 \times 10^6 \text{s}^{-1}$ | 10 |
| $\text{Xe}(7p, 7s') \rightarrow \text{Xe}(6s')$ | $2.89 \times 10^6 \text{s}^{-1}$ | 19 |
| $\text{Xe}(7p, 7s) \rightarrow \text{Xe}^*$ | $4.64 \times 10^6 \text{s}^{-1}$ | 20 |
| $\text{Xe}(5d) \rightarrow \text{Xe}^*$ | $4.00 \times 10^5 \text{s}^{-1}$ | 20 |
| $\text{Xe}(6p) \rightarrow \text{Xe}^*$ | $2.72 \times 10^7 \text{s}^{-1}$ | 21 |
| $\text{Xe}(5d) \rightarrow \text{Xe}(6p)$ | $1.90 \times 10^5 \text{s}^{-1}$ | 22 |
| $\text{Xe}(5d) \rightarrow \text{Xe}$ | $1.67 \times 10^9 \text{s}^{-1}$ | 22 |
| $\text{Xe}(5d) \rightarrow \text{Xe}(6p)$ | $2.46 \times 10^6 \text{s}^{-1}$ | 20 |
| $\text{Ar}^{**} \rightarrow \text{Ar}(3d, 3d')$ | $6.2 \times 10^7 \text{s}^{-1}$ | 10 |
| $\text{Ar}(3d, 3d') \rightarrow \text{Ar}(4p, 4p')$ | $9.5 \times 10^6 \text{s}^{-1}$ | 10 |
| $\text{Ar}(4p, 4p') \rightarrow \text{Ar}(4s)$ | $7.0 \times 10^7 \text{s}^{-1}$ | 10 |

Line Broadening Collisions

| | | |
|---|-----------------------|-------|
| $\text{Xe}(5d) + \text{He} \rightarrow \text{Xe}(5d) + \text{He}$ | 4.0×10^{-10} | e, 16 |
| $\text{Xe}(5d) + \text{Ne} \rightarrow \text{Xe}(5d) + \text{Ne}$ | 5.0×10^{-10} | e, 16 |
| $\text{Xe}(5d) + \text{Ar} \rightarrow \text{Xe}(5d) + \text{Ar}$ | 8.0×10^{-10} | e, 16 |
| $\text{Ne}(3p', 3p) + \text{He} \rightarrow$ | 7.0×10^{-10} | e, 17 |
| $\text{Ne}(3p', 3p) + \text{He}$ | | |
| $\text{Ne}(3p', 3p) + \text{Ar} \rightarrow$ | 7.0×10^{-8} | e, 17 |
| $\text{Ne}(3p', 3p) + \text{Ar}$ | | |

| | | |
|-------------------------|-------------------------|-------|
| Ne(3p',3p)+Ne → | 9.0 x 10 ⁻⁸ | e, 17 |
| Ne(3p',3p)+Ne | | |
| Ar(3d)+He → Ar(3d)+He | 7.0 x 10 ⁻¹⁰ | 12 |
| Ar(3d')+He → Ar(3d')+He | 7.0 x 10 ⁻¹⁰ | 12 |
| Ar(3d)+Ar → Ar(3d)+Ar | 9.0 x 10 ⁻⁸ | 12 |
| Ar(3d')+Ar → Ar(3d')+Ar | 9.0 x 10 ⁻⁸ | 12 |

^a Computed by Monte Carlo model described in Ref. 1.

^b Rate coefficients have units of cm³s⁻¹ unless notes otherwise.

b(Ar(3d)) denotes branching ratio to Ar(3d).

^c Estimated. See text.

^d Only exothermic quenching reactions are listed. The rates of endothermic reactions are computed from detailed balancing.

^e Value derived from model.

B.1 References

- ¹ M. J. Kushner, J. Appl. Phys. **66**, 2297 (1989).
- ² F. Kannari, A. Suda, M. Obara, and T. Fujioka, IEEE J. Quantum Electron. **QE-19**, 1587 (1983).
- ³ R. Deloche, P. Monchicourt, M. Cheret. and F. Lambert, Phys. Rev. **A13**, 1140 (1976).
- ⁴ C. B. Collins. and F. W. Lee, J. Chem. Phys. **68**, 1391 (1978).
- ⁵ Y. J. Shiu and M. A. Biondi, Phys. Rev. A **17**, 868, (1978).
- ⁶ D. Smith and M. J. Copsey, J. Phys. B **1**, 650 (1968).
- ⁷ D. Smith and M. J. Copsey, J. Phys. B **1**, 638 (1968).
- ⁸ C. B. Collins and F. W. Lee, J. Chem. Phys. **68**, 1391 (1978).
- ⁹ P. K. Leichner and R. J. Ericson, Phys. Rev. A **9**, 251 (1974).
- ¹⁰ R. S. F. Chang and D. W. Setser, J. Chem. Phys. **69**, 3885 (1978).
- ¹¹ G. Bekefi, Principles of Laser Plasmas, Wiley-Interscience. New York, (1976).
- ¹² J. W. Shon, M J. Kushner, G. A. Hebner and G. N. Hays, J. Appl. Phys. **73**, 2686 (1993).
- ¹³ D. C. Lorents, D. J. Eckstrom, and D. Huestis, "Excimer formation and decay processes in rare gases," SRI Report No. MP 73-2, SRI International, Menlo Park, CA (September, 1973).
- ¹⁴ T. G. Finn, L. J. Palumbo, and L. F. Champagne, Appl. Phys. Lett. **33**, 148 (1978).
- ¹⁵ A. P. Vitols and H. J. Oskam, Phys. Rev. A **5**, 2618 (1972).
- ¹⁶ G. A. Hebner and G. N. Hays, Appl. Phys. Lett. **59**, 537 (1991).
- ¹⁷ A. Y. Aleksandrov, V. A. Dolgikh, I. G. Rudoi, and A. M. Soroka, Sov. J. Quantum Electron. **21**, 611 (1991).
- ¹⁸ W. J. Alford, IEEE J. Quantum Electron. **QE-26**, 1633 (1990).
- ¹⁹ J. H. Kolts and D. W. Setser, in Proceedings of the 7th Winter Colloquium on High Power Visible Lasers, Park City, Utah, 1977.
- ²⁰ M. Aymar and M. Coulombe, At Data Nucl. Data Tables **21**, 537 (1978).
- ²¹ J. K. Ku and D. W. Setser, J. Chem. Phys. **84**, 4304 (1986).
- ²² L. Allen, D. G. C. Jones, and D. G. Schofield, J. Opt. Soc. Am. **59**, 842 (1969).

VITA

Jong Won Shon was born in 1961 in Seoul, Korea. He moved to Portland, Oregon in 1979. He attended Oregon State University at Corvallis, Oregon, where he received his Bachelor of Science degrees in Electrical Engineering, Computer Science and Mathematics in 1985. After graduation, he began his graduate studies at the University of Illinois, Urbana-Champaign, where he obtained his M.S. and Ph.D. degrees in Electrical and Computer Engineering, and will receive his Ph.D. in January 1994.